ANALYSIS OF A NOVEL TURBOMACHINERY SHAFT SEAL DESIGN

by

CANER AKCAN

Submitted to the Graduate School of Engineering and Natural Sciences
in partial fulfillment of
the requirements for the degree of
Master of Science

Sabancı University

August 2008

ANALYSIS OF A NOVEL TURBOMACHINERY SHAFT SEAL DESIGN

APPROVED BY:

Assoc. Prof. Dr. Mahmut F. AKŞİT (Thesis Advisor)	…….
Assist. Prof. Dr. Ali Koşar	…….
Assist. Prof. Dr. Güllü Kızıltaş ŞENDUR	…….
Assist. Prof. Dr. İlyas Kandemir	…….
Assist. Prof. Dr. Kürşat ŞENDUR	…….

DATE OF APPROVAL: …….

ANALYSIS OF A NOVEL TURBOMACHINERY SHAFT SEAL DESIGN

Caner AKCAN

Mechatronics Engineering, MS Thesis, 2008

Thesis Advisor: Assoc. Prof. Dr. Mahmut F. AKŞİT

Keywords: Turbomachinery Shaft Seal, Metal Cloth, Aerodynamic Lifting Force, Natural Frequency Analysis, Leakage Flow Analysis, Compressible Reynolds Equation

ABSTRACT

Advanced sealing systems are needed to control parasitic leakage flows to achieve high turbine engine efficiency and low emissions. Typical extreme turbomachinery engine operating conditions when combined with rotor excursions do not lend simple sealing solutions. This work presents an in-depth analysis of a novel robust yet simple sealing system that is capable of maintaining long life under high speed and high temperature operating conditions. The proposed seal design is actually a gas bearing that is carefully tailored, analyzed, and designed to function as a differential pressure seal. The design involves a simple rigid/semi-flexible seal ring that is attached to a stationary support plate via flexible metal cloth structure. The seal body is capable of moving under the effect of aerodynamic lift force. Therefore, above a certain clearance limit, which ensures that asperity contact is avoided, the seal follows shaft excursions to avoid damaging hard rubs.

Applying established working principles for gas lubricated journal bearing, governing Reynolds equation for compressible gas flow is solved using both finite difference and finite element methods. The results of these analyses are validated with other published work in literature. The calculated seal aerodynamic pressure profile is integrated to obtain the lift force. This force is compared to the frictional drag and other resistive forces that need to be overcome to move the seal with rotor during transients. Four different seal designs with varying geometries are studied, and resulting lifting forces are evaluated. It is verified that necessary lifting force for these designs can be obtained without exceeding lower limits of seal clearance. Furthermore, to ensure dynamic stability of the sealing system, natural frequency analyses are conducted. Results from the analysis under typical operating conditions of a gas turbine indicated that seal natural frequencies are well above rotor operating speeds. Finally, leakage analysis of new seal system is performed. Comparison with brush seal leakage performance rates under typical operating conditions reveals that the analyzed seal designs show satisfactory leakage performances that are similar to those of brush seals.

YENİ BİR TURBOMAKİNE ŞAFT KEÇESİNİN ANALİZİ

Caner AKCAN

Mekatronik Mühendisliği, Yüksek Lisans Tezi, 2008

Tez Danışmanı: Doç. Dr. Mahmut F. AKŞİT

Anahtar kelimeler: Turbomakine Şaft Keçesi, Metal Örgü, Aerodinamik Kaldırma Kuvveti, Doğal Frekans Analizi, Gaz Kaçağı Analizi, Sıkıştırılabilir Reynolds Denklemi

ÖZET

Gelişmiş sızdırmazlık sistemleri, yüksek türbin verimliliğine ulaşmak ve dışarı olan sızıntıları en aza indirmek için istenmeyen kaçak akışları kontrol etmek zorundadırlar. En uç çalışma koşullarında, rotorun kararsız hareketleri karşısında, turbomakinelerde sızdırmazlık sistemlerinin uygulanması basit olmayan çözümler gerektirir. Bu çalışma, yüksek hız ve sıcaklık koşullarında, uzun süreli çalışabilme özelliğine sahip, dayanıklı olduğu kadar basit, yeni bir keçe sisteminin detaylı analizini içermektedir. Öngörülen keçe dizaynı esasında, bilinen gazlı yatakların, farklı basınç ortamları arasında kullanılan keçeye uyarlanmış halidir ve keçe bu şekilde analiz edilmiştir. Keçe dizaynı basit bir katı/yarı-esnek halkanın sabit bir destek levhasına esnek metal örgü vasıtasıyla tutturulmasıyla oluşmuştur. Keçe gövdesi aerodinamik kaldırma kuvvetinin etkisiyle hareket edebilme özelliğine sahiptir. Bu sayede, yüzeyler üzerindeki pürüzlerin birbirine değmediğini garantileyen belli bir şaft-keçe yüzeyi aralığı üzerinde, keçe, kararsız şaft hareketlerini takip edebilecek ve hasar yaratabilecek sert aşınmaları önleyebilecektir.

Bilinen gaz yağlı şaft yatağının çalışma prensipleri uygulanarak, sıkıştırılabilir gaz akışını düzenleyen Reynolds denklemi sonlu farklar ve sonlu elemanlar metodlarıyla çözülmüştür. Bu metodlarla gerçekleştirilen analiz sonuçları, literatürdeki diğer çalışmalarde elde dilen sonuçlarla karşılaştırılmış ve sonuçların birbiriyle uyumlu olduğu görülmüştür. Elde edilen keçe aerodinamik basınç profilinin, kaldırma kuvvetini hesaplamak için integrali alınmıştır. Elde edilen kaldırma kuvveti, sürtünmeyle oluşan ve şaftın kararsız hareketleri karşısında keçenin de hareket etmesine karşı koyabilecek diğer tüm kuvvetlerin toplamıyla karşılaştırılmıştır. Değişen geometrik şekilleriyle dört farklı keçe üzerinde çalışılmış ve bu keçeler üzerinde oluşan kaldırma kuvvetleri hesaplanmıştır. Bu çalışmalarda, yeterli kaldırma kuvvetinin, izin verilebilir en küçük keçe açıklığını ihlal etmeden elde edilebileceği görülmüştür. Bununla birlikte, keçenin dinamik olarak kararlı yapıda olduğunu göstermek için doğal frekans analizi yapılmıştır. Analiz sonuçları, tipik bir gaz turbini çalışma koşullarında, tasarlanan keçelerin doğal frekanslarının türbin rotorunun çalışma hızının oldukça üstünde olduğunu göstermiştir. Son olarak, keçeler üzerinde sızdırmazlık analizi yapılmıştır. Elde edilen sızdırmazlık performanslarının, tipik çalışma koşullarında, fırça keçelerin sızdırmazlık performansına oldukça yakın ve başarılı oldukları gözlenmiştir.

“To my family…”

ACKNOWLEDGEMENTS

I wish to express my deepest gratitude to my thesis advisor Mahmut F. Akşit for his valuable advice and guidance of this work. I am grateful to him not only for the completion of this thesis, but also for his everlasting enthusiasm to answer my questions on all technical matters.

I would like to thank my committee members Güllü Kızıltaş Şendur for her support and enthusiasm during the thesis study, Kürşat Şendur for assisting me to develop the finite difference code, Ali Koşar and İlyas Kandemir for their interest in this work and recommendations.

I would also like to thank all my friends at Mechatronics Graduate Laboratory. Many thanks to Serdar, Fatih, Işıl, Hakan, Muhammet, Ramazan, Özer, İslam, Samir, Tuğrul, Ertuğrul, Orkun, Elif, and Altuğ for their great friendship and valuable support.

My special thanks go to all "esinti" members, "hemşo" and Altan Kayacan for their endless encouragement and trust. I also want to convey my sincere thanks to my room-mates Hakan Günaydın and Ömer Ceylan without whom completing even my undergraduate period would not be possible.

I would like to acknowledge the support provided by The Scientific & Technological Research Council of Türkiye (TÜBİTAK) during my MSc. Studies.

Finally, I would like to thank to my parents and my brother for their great confidence in me and wishing and providing the best for me through my entire life.

TABLE OF CONTENTS

LIST OF FIGURES

LIST OF TABLES

LIST OF SYMBOLS

a	Step size in the y-direction for numerical analysis, $a = \frac{B}{r(m+1)}$
A_s	Side area of seal
b	Step size in the x-direction for numerical analysis, $b = 2\pi / n$
B	Width of seal / axial length of seal
β	Mean free path of air
c	Clearence
D	Diameter of journal/bearing/seal
d	diameter of air molecule
e	Eccentricity
ε	Eccentricity ratio
f	Natural frequency
F_c	Friction force at concentric state
F_n	Aerodynamic lift force
F_s	Friction force between seal and wall
F_t	Friction force at eccentric state
H	h / c
h	Film thickness
h_m	Film thickness at maximum pressure location
$h_{\min}$	Minimum film thickness
h_{nom}	Nominal film thickness
i	Node index in the x-direction
j	Node index in the y-direction
k	Constant for mean free path calculation
k_c	Cloth metal stiffness
k_f	Fluid film stiffness
Kn	Knudsen number

l	$l = (j-1)n + i$
L	Circumferential length of journal/bearing/seal, $L = 2\pi r$
λ	Compressibility number, $\lambda = \left(\frac{r}{c}\right)^2 \frac{\mu\omega}{P_a}$ (dimensionless)
m	Number of nodes in the y-direction
mf	Mass flow rate
M	Mass
M_a	Molar mass
M_s	Mass of the seal
μ	Dynamic viscosity
μ_b	Bulk viscosity
μ_f	Coefficient of friction
n	Number of nodes in the x-direction
N	Mole number of gas
N_A	Avogadro's number
o	Center of journal
o'	Center of bearing/seal
ω	Angular velocity, rad/sec
P	Pressure
P^*	Normalized pressure
P_a	Ambient pressure
P_h	Upstream pressure
P_{hn}	Dimensionless upstream pressure
P_l	Downstream pressure
P_{ln}	Dimensionless downstream pressure
$P_{\max}$	Maximum pressure
$P_{\min}$	Minimum pressure
P_n	P / P_a
P_r	Load per unit projected area, $P_r = W / 2rB$
$\Delta P = \mathrm{DP}$	Differential pressure

φ	Dimensionless variable in the axial direction
ϕ	Attitude angle
r	Radius of journal/bearing/seal
R	Universal gas constant
Re	Reynolds number
ρ	Density
s	Thickness of the designed seal
S	Sommerfeld number
t	Time
t^*	Normalized time
T	Temperature
θ	Angle in the circumferential direction
θ_m	Angle at maximum pressure location
u	Velocity of fluid in x-direction
u^*	Normalized velocity of fluid in x-direction
U	Linear velocity of shaft
v	Velocity of fluid in y-direction
v^*	Normalized velocity of fluid in y-direction
V	Volume of gas
$\mathbf{V}$	Velocity in vector form
w	Velocity of fluid in z-direction
w^*	Normalized velocity of fluid in z-direction
W	Load
W_x	x-component of load
W_z	z-component of load
W_s	Weight of seal
(x, y, z)	Global coordinates
(x^*, y^*, z^*)	Normalized global coordinates

LIST OF ABBREVIATIONS

FD	:	Finite Difference
FEA	:	Finite Element Analysis
HS	:	Hard Sphere
MM	:	Maxwell Molecules
VHS	:	Variable Hard Sphere
VSS	:	Variable Soft Sphere

1 INTRODUCTION

1.1 Motivation

Gas turbines and other turbomachinery are comprised of different pressure zones around high speed rotating components. Parasitic leakage flows have pronounced impact on turbine engine efficiency and emissions. Advanced sealing systems are developed to control and manage secondary flow circuit in turbine engines. Typical sealing locations on a gas turbine include compressor discharge, bearing seals, turbine inter-stage packings and the bucket tips [1]. An aircraft gas turbine engine may have more than 50 sealing locations [2]. Cumulative effect of leakage on power consumption and thrust can be significant. Owing to the scarcity in fossil fuel resources, engine efficiency requirements become more demanding and seal designs are pushed to their limits.

Main challenge in innovative design features is achieving tighter clearances between stationary components and rotating shaft. Thermal transients in industrial turbines, and rotor excursions during landing or maneuver loads in the aircraft engines put limits on allowable seal-rotor radial clearance. Brush seals avoid clearance related problems to some extent as they allow contact between bristle tips and rotor surface due to flexible nature of bristles. However, bristle tip contact creates wear problems and reduces seal life cycle. Besides wear problems, leakage through and under bristles reduce leakage performance.

In order to achieve robustness against transient excursions and to keep the clearances at minimum level, this work presents analysis of a novel seal design which is held with flexible supports. The seal body, which is attached to the stationary shroud support with a flexible metal cloth, has the capability of moving with the rotor in

response to the acting aerodynamic lift force. After a certain point, eccentricity between shaft and seal body remains constant and leakage through the seal is stabilized. The proposed novel seal design is actually a gas bearing that is carefully tailored, analyzed, and designed to function as a differential pressure seal. Aerodynamic journal bearings are commonly used in many daily life equipments such as car engine shaft bearings. However, here are the main differences with the proposed seal design and a typical journal bearing:

- Working fluid in a typical journal bearing is oil whereas proposed seal works with air or combustion gases. Therefore, compressible flow will govern, as opposed to simpler incompressible lubrication theory.
- The proposed gas bearing will work against a considerable pressure difference while common bearings work in a balanced pressure environment at both ends.
- A typical bearing is fed/pressurized through supply holes embedded within the journal itself. However, the proposed seal is fed through the gas entering from high pressure side.

In this work, first a solution procedure has been established for the relations governing the fluid film in gas lubricated journal bearings. The analysis is validated with the previous gas bearing work in literature. Then analysis is applied to the proposed seal design case. The calculated pressure profile is integrated to obtain the lift force. This force is compared to the frictional drag and other resistive forces that need to be overcome to move the seal with rotor during transients. A seal stability analysis is also provided.

As stated earlier, dynamics of the designed seal is governed by lubrication theory as that of well-known gas lubricated journal bearings. Therefore, it is essential to understand governing parameters, properties and limiting conditions of gas lubricated journal bearings in order to gain an insight into the working principle of the designed seal.

1.2 Gas Lubricated Journal Bearings

1.2.1 Structure of Gas Lubricated Journal Bearings

Gas lubricated journal bearings are used as self-acting machine components to carry radial loads in many industrial applications. Necessary lifting force in these components is created by aerodynamic action of the journal (sleeve). Given that the load carrying capacity of gas lubricated bearings are substantially low, the same journal, which is utilized as a bearing in light load carrying applications, can be used as a sealing component to prevent the parasitic leakages resulting from pressure differences. Gas bearings and the proposed gas seal have the similar structure except that the seal will be held in flexible supports and maintain pressure difference across. Without loss of generality, gas film lubrication theory for journal bearings can be adopted to the proposed novel gas seal design.

In a gas lubricated journal bearing, as the shaft starts to rotate from rest, a thin layer of gas is pulled through because of viscous drag [3] and is compressed to a great extent between the bearing surfaces (Figure 1.1). As a result, an adequate pressure force is created to support the load without any external pumping agency. Figure 1.2 illustrates the typical design parameters for a journal bearing assembly.

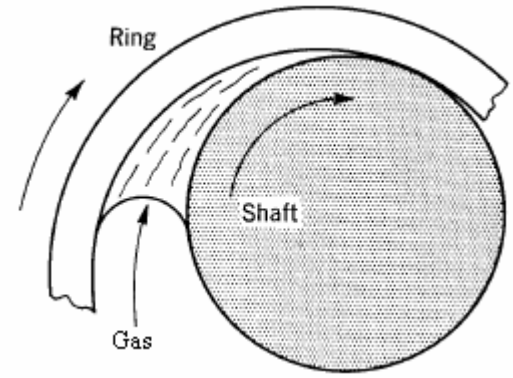

Figure 1.1 Gas film formation [4]

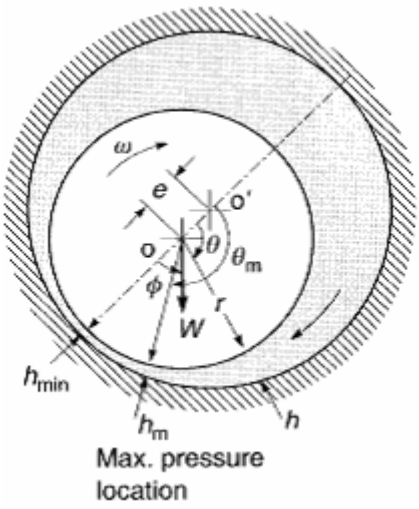

Figure 1.2 Plain journal bearing geometry [5]

Center of the journal is represented by o while o' is the center of the bearing. Difference in radii of the journal and the bearing is called clearance and represented by c. Note that journal and bearing are not concentric and the journal is moved around bearing. Particular position of journal inside the bearing is determined by the equilibrium of forces created by aerodynamic action. The direction of journal movement is in the same way as the rotation. The distance between the centers of the journal and the bearing is called eccentricity and represented by e. When journal touches bearing, e is equal to c. On the other hand, if the rotor is very light and spinning very fast, journal rotates almost in concentric position. At this point, e is very close to zero. In addition, the ratio of eccentricity to clearance defines the eccentricity ratio such that;

$$\varepsilon = e / c \tag{1.1}$$

For most bearings c/r is between 10^{-4} and 10^{-3} [5]. Based on this, variation of film thickness can be approximated as

$$h = c(1 + \varepsilon \cos(\theta)). \tag{1.2}$$

Details of this derivation are presented in [6].

Note that minimum film thickness occurs at $\theta = 180^{\circ}$ and is given as

$$h_{\min} = c(1 - \varepsilon) \tag{1.3}$$

Another important design parameter for the journal bearing is the attitude angle. Attitude angle represents the angle between the load axis and the line $o\,o'$, and is displayed by ϕ.

1.2.2 Common Characteristics of Gas Lubricated Journal Bearings

Gases have unique properties which make them superior over liquids as lubricants. One of the most interesting aspects of gases is their viscosity-temperature relationship. Viscosity of gases increases with increasing temperature but is moderately affected by local temperature changes. Therefore, at high temperatures, with the increasing viscosity, load carrying capacity of gas lubricated bearings is increased. On the other hand, viscosity of liquids is inversely proportional to the temperature and very sensitive to local changes. Figure 1.3 demonstrates the viscosity of common gases as a function of temperature. Air is located at the midrange of gases when the viscosity values are considered. Viscosities of various gases for a broader range of temperature values are tabulated in Table 1.1. These air viscosity data are used later for lift force analysis.

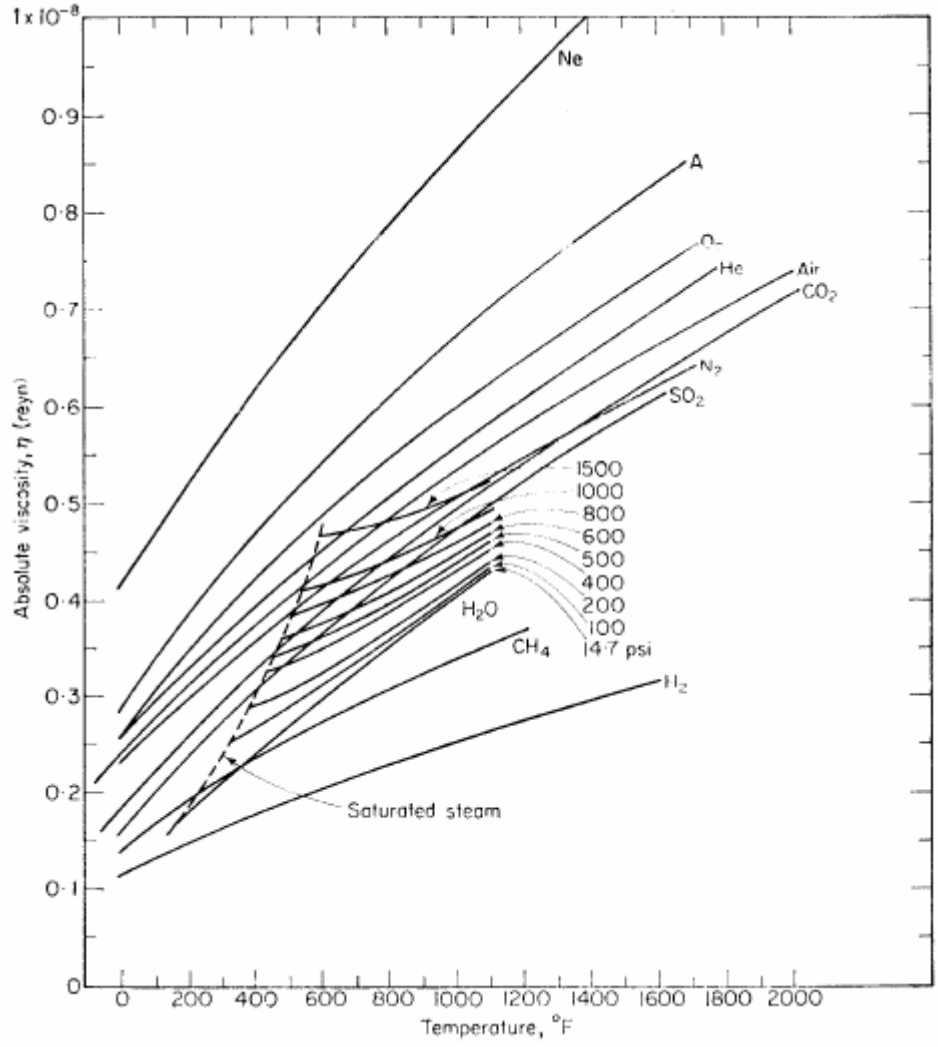

Figure 1.3 Viscosity - Temperature Relationship of Common Gases [7]

Temperature		Air	Ar	CO_2	H_2O	He	Kr	N_2	Ne	Xe
°F	°R	Absolute viscosity, η, lbf s/in.² (reyn)								
−280	180	1.07×10^{-9}	1.27×10^{-9}	0.74×10^{-9}	---	1.45×10^{-9}	---	1.05×10^{-9}	2.12×10^{-9}	---
−100	360	1.97	2.41	1.49	---	2.27	2.50×10^{-9}	1.91	3.48	2.24×10^{-9}
80	540	2.68	3.32	2.20	---	2.96	3.67	2.57	4.56	3.35
260	720	3.29	4.10	2.84	2.08×10^{-9}	3.56	4.69	3.15	5.50	4.38
440	900	3.84	4.80	3.41	2.59	4.11	5.61	3.66	6.35	5.29
620	1080	4.34	5.44	3.93	3.12	4.62	6.46	4.14	7.16	6.15
800	1260	4.80	6.04	4.41	3.64	5.11	7.23	4.57	7.91	6.93
980	1440	5.24	6.59	4.86	4.17	5.56	7.95	4.99	8.64	7.67
1160	1620	5.64	7.11	5.29	4.69	6.00	8.65	5.39	9.31	8.36
1340	1800	6.05	7.60	5.70	5.20	6.43	9.30	5.75	9.96	9.03
1520	1980	6.44	8.09	6.09	5.70	6.84	9.92	6.13	10.60	9.66
1700	2160	6.80	8.55	6.45	6.19	7.23	10.52	6.49	11.19	10.26
2600	3060	8.55	11.82	8.14	8.41	9.05	13.26	8.14	14.00	13.00
Boiling temperature, °R		---	147.2	---	67.2	7.9	219.2	139	48.7	298.4
Gas constant, $in.^2/(s^2\ °R)$		2.47×10^5	1.79×10^5	1.63×10^5	39.8×10^5	17.9×10^5	0.85×10^5	2.55×10^5	3.54×10^5	0.55×10^5

Table 1.1 Viscosity of Various Gases at 14.7 psia [6]

Another interesting aspect of gases is their viscosity-pressure relationship. Unlike viscosity-temperature relationship, gas viscosity is insensitive to the pressure change. This can be observed in Figure 1.4. Due to this low dependency on local temperature and pressure change, viscosity of gases can be considered constant within the lubricating film for the same ambient conditions.

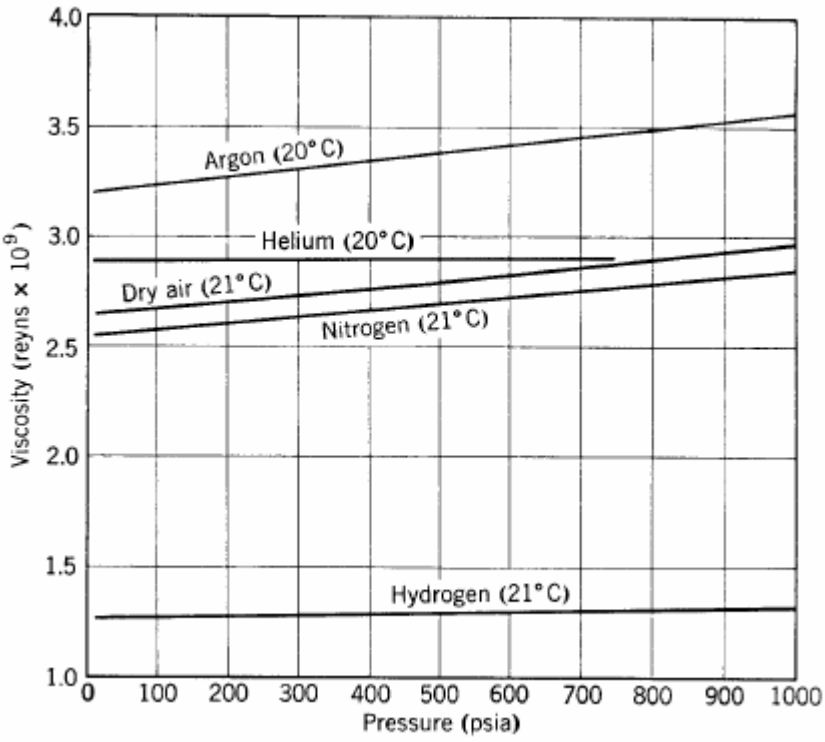

Figure 1.4 Viscosity – Pressure Relationship of Various Gases [8]

The main difference between gas lubricated journal bearings and an oil lubricated journal bearing is that the lubricating fluid for gas lubricated journal bearing is compressible. Since the lubricating film is gaseous, density of gas throughout the lubricating film is related to the pressure variation on the bearing surface. Reynolds equation for compressible fluids poses a difficult problem, and a closed-form solution is obtainable for only few special simplified cases. On the other hand, governing equation for liquid lubricating bearings is simpler to deal with as the density of liquid film is not affected by pressure changes. The lubrication theory for gas films is explained in great detail in the 3rd chapter.

A useful assumption on compressible Reynolds equation can be made consistent with the surface speeds of rotating shaft. At low relative speeds, the gas-film density remains nearly constant, so that the fluid film between the bearing surfaces behaves as if incompressible. Thus, at low relative speeds, incompressible lubrication theory can be adopted. However, at high speeds, the density of gas-film can change considerably, so that gas-film properties differ substantially from those of similar liquid films [8]. For such cases, nonlinear Reynolds equation governing the compressible gas flow must be solved either by iterative methods or analytically based on a considerable linearization work.

The main drawback for gas-lubricated journal bearings is their low load carrying capacity resulting from substantially low viscosity of gases. Viscosity of air is on the order of 1/1000 of that of liquid lubricants at ambient temperature. Therefore, film thickness, pressures, and load capacities of gas bearings are reduced in great extent when compared with a liquid lubricated bearing. Bhushan [5] reports that the pressures in self acting gas bearings are typically 0.1 MPa, whereas these are on the order of 100 MPa in liquid film bearings. Although this is a significant disadvantage for bearing applications, for seal designers, load carrying capacity is not the primary concern. However, for the proposed flexible and compliant seal structure, a lift force is necessary to avoid the contact between the seal surface and rotating shaft. Required lifting force is very low in most cases when compared to bearing applications. If seal is properly designed, necessary lift forces can be produced by the aerodynamic action of gas film.

To sum up, significant advantages of gas-lubricated bearings can be grouped as follows [4-6], [8], [9]:

1. Viscous resistance of gas film is relatively low.
2. The lubricant is clean and does not contaminate surfaces as in the case of oil.
3. The gaseous lubricant is chemically stable for extremely low and extremely high temperatures and does not break down from cavitations.
4. Viscosity of gaseous lubricant is increasing with temperature so that the heating effect tends to increase the restoring force to overcome the overload.
5. The danger of fire is almost none.
6. Because of no fire hazard, gas lubricated journal bearings are more suitable for high speed applications and more noise-free when compared with rolling-contact bearing.
7. Gas lubricated journal bearings do not require cooling operations.

On the other hand, some former studies indicate the following weaknesses of gas-lubricated journal bearings:

1. Load carrying capacity of a gas-lubricated journal bearing is many times less than that of oil-lubricated journal bearing which has the same size.
2. Coefficient of friction of dry contact is higher than that in oil-lubricated journal bearing. Therefore, the gas lubricated journal bearing must have an extremely fine surface finish and must be properly aligned.
3. The viscosity of gaseous lubricant is nearly 1000 times less than that of oil lubricant. Therefore, the separation of contacting surfaces requires speeds which are 1000 times higher than that of oil-lubricated bearings.

1.2.3 Limiting Conditions for Gas Lubricated Journal Bearings

Although gas-lubricated journal bearings operate according to aerodynamic lubrication theory, all self-acting gas bearings have physical contact at start-stop conditions. In that interval, a self-acting gas journal bearing is in the boundary lubrication regime. Even if the surfaces are coated with a boundary lubricant, the coefficient of friction is expected to be at least three times larger than that between oil-lubricated metal surfaces. Consequently, a gas bearing is more vulnerable to wear damage than an oil-lubricated bearing [9]. For this reason, shaft-bearing assembly and machining of bearing surfaces are vital processes for a gas-lubricated bearing to function properly.

The lowest permissible limit of film thickness is a very controversial issue.

> "Smallest acceptable film thickness depends on the degree of finish of the sliding surfaces, on the elastic rigidity of the journal and bearing surfaces, on the maximum expected thermal distortion of the clearance space due to thermal gradients, and finally on the expected size of any contaminating particles that may find their way into the lubricant stream and attempt to pass through the clearance space and through the minimum film thickness" [4].

Karelitz [10] suggests that the lowest practical limit for fluid film lubrication should be approximately (0.00005 in.) 1 μm. In his test apparatus, the bearing block and the shaft are placed in contact initially. Then, the shaft is started to rotate and a rapid wearing away of bearing block is observed. When the wear stops, the clearance between the bearing surface and the journal is measured. Measured values of minimum films thickness are identified as 0.000058 in. and 0.000059 in. for two different load conditions respectively. Karelitz also observes the actual height of the asperities near the rubbed surface. The distance from peak to valley of the surface roughness is on the same order of magnitude as the estimated value of minimum film thickness. Not only Karelitz but also McKee [11] and Stanton [12] observe the minimum film thickness, and the results are around the same order of magnitude. On the other hand, specifically for the gas lubricated bearings, Gross [8] states that bearing surfaces may have to be flat to 5 μin. and have less than 1 μin. rms surface roughness. He proposes that the bearings should be manufactured from hardened tool steel with surfaces finished optically smooth so that the surface roughness is no greater than 5 μin. rms. Although they are finely finished, Fuller [4] emphasizes that the practical minimum fluid film thickness should not be less than 1 μm. For gas film bearings, the clearances are less than that of liquid lubricated bearings since the friction force is much lower and the contamination of the dirt particles is rare. Considering the very low film thickness in gas-lubricated journal bearings, it is crucial to remove all natural frequencies of the bearing from operating frequencies.

As stated before, in gas-lubricated bearings, the density change as a function of pressure can not be neglected in the solution of governing equation. On the other hand, viscosity of gases varies very little with pressure and can be assumed constant. Similarly, the temperature in between the gas film can be regarded as constant although the viscous heating can cause local temperature rise. However, for oil-lubricated bearings, temperature rise is a significant factor that affects the viscosity of the oil film. Thus, when compared with oil-lubricated bearings, we can state that the complexity of

nonlinear governing equation of compressible gas flow is a bit reduced by constant viscosity assumption. Analytical solution of the governing equation is obtainable only for very special cases such as one dimensional steady state flow. Therefore, numerical solution techniques are commonly used to obtain results for the finite bearing cases.

1.3 Problem Statement

Evolution of innovative design features for gas path sealing applications is parallel to the reduction of effective leakage clearance. Value of this clearance is strictly related to the operating conditions of the environment. In a typical gas turbine, increasing temperature and centrifugal forces can change the diameter and position of the shaft considerably. Therefore, most shaft seals are mounted with relatively high clearances to avoid a possible contact between seal and shaft. Labyrinth seals are of the typical examples and have higher leakage rates compared to their competitors, brush seals. Brush seals are breakthrough in sealing applications as their structure allows contact with the bristle tip and rotor surface due to flexible nature of the bristles. In return, leakage rates are reduced considerably. However, complex pressure-stiffness coupling and bristle rotor contact introduces problems associated with the brush seal technology that limit their use at some specific locations and environments. Among the reported problems, accelerated wear between rotor and bristles during transients, bristles remaining hang-open by inter-bristle friction after rotor excursions, high heat generation at rubbing interface during wear-in period, and wires being susceptible to high cycle fatigue are major concerns [13].

Up to now, for most compliant seal structures in literature, a physical contact and wear of materials are inevitable and the seal is deteriorated. Thus, in an attempt to provide an alternate solution, this work proposes a novel gas seal concept coupled with a flexible metal cloth structure. Metal cloth structure enables relatively rigid seal body to move freely during excursions with aerodynamic lift force. To understand the dynamics of designed seal, gas-lubrication laminar flow theory is revisited and compressible Reynolds equation is solved for general finite bearing cases using finite difference (FD) and finite element approach (FEA). Developed algorithms for both

approaches are validated with published results for finite bearings. Then, with the proper boundary conditions, compressible Reynolds equation is adopted to the proposed seal, and lifting force is evaluated. Leakage performances of the seal are analyzed theoretically under steady conditions, and flow rates are compared with other seal designs. A natural frequency analysis is also conducted to make sure that the seal is functioning properly in the mechanically stable region.

1.4 Literature Survey

Literature on this work can be studied under two main groups, background on sealing applications and solution methods for compressible Reynolds equation. Although there are various seal types available, labyrinth and brush seals are the most commonly used designs for turbomachinery sealing applications. Labyrinth with sharp edge teeth design is the traditional and most commonly used configuration to prevent leakage flows resulting from pressure differences around rotating shafts. Its mechanical simplicity makes it attractive for various sealing locations. The effectiveness of labyrinth seals depends on the magnitude of radial clearance, the number of fingers, and their configuration. Fabrication technology, excursion of the rotor in transient conditions, bearing dampers and heating effect on the seal determines the value of radial clearance [14]. Labyrinth seals are effective when radial clearances are small. However, it loses performance with wear of rubbing surfaces and at large clearances that are dictated by transient thermal conditions [2]. Because of high labyrinth leakage, there is a tendency in gas path sealing applications to use brush seals for which the radial clearance is not a limiting condition due to the flexible structure of bristles.

The invention of brush seal has become a breakthrough in sealing industry. The compliance of individual bristles gives brush seals the superiority over a labyrinth seal [15]. Ferguson [16] reports that leakage improvements an order of magnitude over labyrinth seals are possible in the brush seal applications. Similarly, Carlile [17], and Chupp [18] present experimental leakage data for brush seals illustrating the increase in leakage performance compared to annular and labyrinth seals. Parallel to the leakage improvements, there is also increase in thrust of gas turbine engine equipped with brush

seals. On the other hand, tests at Allison Gas Turbine Division show that the tolerance of brush seals to dynamic excursions is also superior [19]. Heat generated in rubbing contact of dynamic excursions is considerably less than that in labyrinth seal. For industrial gas turbines, performance improvements in power and heat rate are reported [1].

Contrary to the advantages, there are also reported problems for brush seal applications. When coupled with frictional effects, loads created by the leakage flow and pressure difference become the main sources for the challenges encountered in application of brush seals [15]. Bristle stiffening, hysteresis and pressure closure are the three main phenomena which affect the clearance and wear rates of the brush seal materials [15], [20]. Basu [21], Hendricks [22], and Short [23] developed new brush seal designs that are capable of reducing these effects. However, test results showed that these innovative brush seal designs still exhibit substantial hysteresis and pressure closure [24]. In addition, Aksit [15] states that frequent excursions may still limit the brush seal life and performance even though superior design features are developed. Therefore, large industrial turbines, which experience bristle-rotor interference only during start up or shut down, are more suitable for brush seal applications than aircraft engines that face much more frequent excursions. Thus, the reliability issues of brush seals for aircraft engines still remain important.

On the gas bearings side, a recent advancement in bearing technology took place when foil bearings came into the picture. Excessive radial movement of shaft can be overcome by the flexible structure of foil bearings. Owing to the flexible structure and damping capability of top foil and bump foil, a foil bearing can operate in reliable conditions even if both the rotational speeds and the operating temperatures are very high. A review of foil bearing technology, [25] reveals that foil bearings can even operate at clearances which are less than 0.0005 inch for a 2 inch diameter shaft running at 36000 rpm. Whirl instability and misalignment problems are also resolved by foil bearings. By the aerodynamic action of the rotating shaft, a gas film is formed and the top foil is expanded. The clearance for the foil bearing applications is defined by the magnitude of preload between the top foil and the journal at the mounting period. Radil et al. [26] investigate the effect of clearance on the performance and load capacity of foil bearings. Likewise, Dellacorte and Valco [27] have investigated the load carrying capacity of foil bearings in a wide temperature range, including very high temperatures. One of the main advantages of foil bearings over brush seals occurs in the area of

coating. The foil structure contacting with the journal at the startup is more suitable for coating even if the operating temperatures are substantially high. Dellacorte et al. [28] evaluate the performance and durability of foil bearings under a wide range of loads at temperatures from 25^{o}C to 650^{o}C. Owing to the above mentioned advantages, foil bearings are finding increasing use in high speed engine applications. However, high manufacturing and maintenance costs of foil bearings limit the application areas. The assembly of foil and housing structures require a precise machining and a well defined production process. It is an apparent necessity for the turbo machinery industry to develop a foil like structure that shows the similar damping and stiffness characteristics but simpler in design and easier to manufacture.

Flexibility in sealing components has been extended with the introduction of metal cloth structure into sealing applications. It is a challenging issue for turbomachinery seal designers to maintain flexibility with extended service life in high-temperature, high-pressure sealing applications. Integration of flexible metal cloth to the sealing applications provides a means to tolerate thermal misalignments and shows the promise to extend the service life at high temperatures [29]. Metal cloth seals are utilized in various applications in industrial gas and steam turbines [30], [31]. Application areas are generally the junctions between stationary components where the vibratory motion, thermal growth and misalignment are possible to occur. Up to now, the application of metal cloth seals remains limited between stationary components. In this study, a design of seal ring coupled with flexible metal cloth is developed to provide dynamic sealing around rotating shafts. Unlike the traditional dynamic seal designs, new seal has the capability of moving freely under the action of aerodynamic lift force.

As stated earlier, dynamics of gas film around the proposed seal is governed by the compressible Reynolds equation. A complete analytical solution to the governing equation set is unobtainable. However, some semi-analytical solution procedures are available for gas bearings in literature [32], [33]. These analytical procedures are limited to some specific ranges of eccentricity ratios. Fully numerical solutions to the compressible Reynolds equation are widespread in literature [34], [8], [35]. Application areas of these solutions are limited by either very high or very low compressibility numbers. Raimondi [36] presents the most comprehensive numerical solution for gas journal bearings as the results are applicable for a large set of compressibility numbers and eccentricity ratios. However, the precision of his results are limited by mesh/grid size since digital computers had low performance during mid 20th century. Largest

mesh/grid size presented in Raimondi's study is 40x32. In this study, solution to the governing Reynolds equation has been obtained for mesh/grid sizes extending to 500x600. However, there is no major change in the results as the mesh/grid size increases. It is a common procedure in literature to demonstrate the obtained results in non-dimensional design charts with respect to the value of compressibility number [4], [6]. The results are published for comparison purposes at certain length-to-diameter ratios which are varying between ½, and 2. There is no published numerical code in the literature. Solution of the pressure distributions for bearing designs having length-to-diameter ratios different than the published plots requires interpolation to the nearest available result or developing a numerical code applicable to all design combinations. In this study, a special numerical code is developed, therefore, the compressible Reynolds equation can be solved for any bearing design. However, there are still limitations to the application of numerical solution procedure. Effective implementation of numerical procedure is parallel to finding the appropriate mesh/grid size. When length-to-diameter ratio B/D, eccentricity ratio ε, and compressibility number λ are increased above a certain point, required mesh/grid size to converge a solution increases exponentially. For excessively high values of stated parameters, setting the appropriate mesh/grid size in finite difference approach requires a considerable effort. However, for a typical gas turbine seal, these parameters are not excessively high and solution to the governing Reynolds equation is obtained without so much computational effort. These parameters are presented in chapter 5. On the other hand, finite element code generated by commercial software COMSOL Multiphysics is capable of converging a solution even if values of mentioned parameters are fairly high. Therefore, for special design cases having extremely high B/D, ε, and λ, finite element code generated by COMSOL Multiphysics can be used effectively.

There are also other solution procedures for the gas-lubricated plain journal bearing such as the interior collocation method presented by Arakere and Nelson [37]. Recently, Belforte et al. [38], [39] have put extensive effort to analyze the static and dynamic characteristics of self-acting gas bearings with rotating shafts by developing mathematical models to derive analytical relations and transfer functions for gas-film coefficients. Since metal cloth structure is highly flexible compared to rotor shaft, in this work, dynamic stability of designed seal is investigated by assuming that rotating shaft is totally rigid.

Literature survey demonstrates that the major problem in sealing applications is wear of materials on contacting surfaces. Traditional seal designs, such as brush seal, reduce wear related problems to some extend but an increase in leakage rate is observed as operating time increases. The aim of this study is to avoid shaft-seal contact in a typical gas turbine except start-stop conditions, and to stabilize the leakage flow around acceptable ranges. The idea to pursue this goal is to develop a gas seal coupled with metal cloth which can move freely during shaft excursions under the effect of aerodynamic lift force. Proposed design is similar to typical aerodynamic gas journal bearing except that it is held with flexible supports. Designed seal is explained in detail in chapter 2. Governing theory of compressible gas flow and its application on the designed seal are investigated in the succeeding chapters.

2 FLEXIBLE GAS SEAL DESIGN

Most annular seals, including labyrinth and brush seals, are mounted rigidly. Turbine parts expand and distort under thermal and pressure loads during operation at high temperatures and pressures. These deformations are predominantly in the form of relative thermal growth in industrial gas turbines, although shaft deflection due to heavy rotor weight is also present. In aircraft engines, limiting shaft deflections occur due to g-forces caused by maneuver loads or bad landing instances in addition to thermal distortions. Common engineering practice is to calculate/estimate possible rotor excursions in operation, and provide a preset rotor-seal clearance to accommodate worst case conditions. Eccentric rotor-seal operation has to be endured. In such situations, radial distance between the rotor and the annular seals can be very close. If the mounting clearance between the seal and the shaft is not sufficient to prevent physical contact, severe damage may occur leading to eventual engine failure. Therefore, mounting clearance between rigid labyrinth seals and rotor is left relatively high to avoid or limit so-called “hard rubs” during worst case conditions. When the eccentric rotation of the shaft coupled with this predefined annular gap is taken into account, the amount of leakage flow for labyrinth seals can be an order of magnitude higher compared to that of brush seals.

On the other hand, brush seals have flexible bristles that can be allowed contact with rotor during excursions. When dynamic rotor excursions occur, bristles can take relative position with respect to the rotor and reduce the actual gap. Therefore, for brush seal, leakage rates show stable characteristics for a range of clearances. However, accelerated wear between rotor and bristles during transient excursions poses a challenging problem for brush seal applications which limits the life-cycle. Pressure closure may accelerate seal wear while other issues such as bristle stiffening and hysteresis may limit seal leakage performance. It is also reported that brush seal performance may degrade at high differential pressures due to the fact that bristles bend

under back plate and actual clearance increases. In addition, cost of brush seals increase drastically as seal size increases while careful handling is required due to delicate nature of bristles.

The presented seal design provides a low cost, simple, easy to manufacture and robust alternative that will provide similar leakage performance as brush seals with higher pressure and temperature capability. As illustrated in Figure 2.8 the seal design involves a seal ring that is coupled with a flexible metal cloth to provide the ring the capability of following the rotor in all radial directions. The ring will be semi-flexible in radial direction while being infinitely rigid in axial direction for high pressure load capability. Flexible shroud attachment will allow aerodynamic lift force to push seal ring around avoiding rotor contact except for start-stop conditions. This will allow extended seal life without performance degradation.

2.1 Structure and Properties of Metal Cloth

The proposed seal design is based on coupling a semi-flexible seal ring with a flexible metal cloth attachment. Therefore, the whole seal structure has many degrees of freedom. A cropped view of the metal cloth clamped on the seal ring and on the shroud wall is illustrated in Figure 2.1. Metal cloth is originally a woven wire mesh. Wire mesh can be manufactured from any metal/alloy that can be drawn into wire form. Most commonly used materials for the weaving of wire cloth are steel, stainless steel, copper alloys, aluminum alloys and nickel alloys. Each of these materials is classified into sub-groups according to the percentage of the additives included. Chromium and nickel additives in the stainless steel make it resistant to corrosion and strong at high temperatures. Stainless steel is also resistant to the oxidation at high temperatures. Since the operating temperatures are extremely high, around 550^{o}C (1000^{o}F), in turbo machinery, stainless steel or Nickel/Cobalt super alloy wires are more favorable due to their superior performance against oxidation and corrosion.

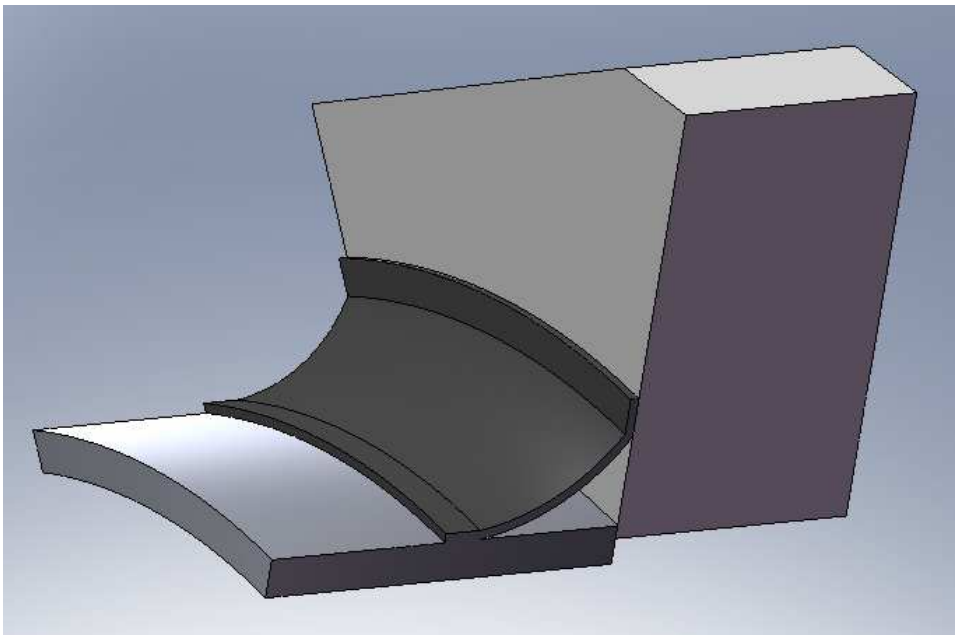

Figure 2.1 Cropped View of the Seal Ring – Metal Cloth Assembly

Wire cloth is also classified based on weave type, wire diameter and mesh number per linear inch. Plain weave, plain Dutch weave, twilled weave and twilled Dutch weave are some common weave types. Figure 2.2 illustrates the structure of plain Dutch weave for two different mesh sizes. In a plain weave structure, each shute wire passes over one warp wire and under the adjacent warp wire, that is one over and one under. Wires are crimped in the weaving operation. Plain Dutch weave is similar to regular plain weave except that warp wires are larger than shute wires. This construction allows shute wires to be spaced more closely to provide a higher density weave with wedge shape openings. Figure 2.3 explains plain Dutch weave terminology and demonstrates this weaving style in detail.

Figure 2.2 Plain Dutch Weave

Besides the weaving style, mesh number per linear inch is also an important parameter to define the wire cloth characteristics. Since the diameters of warp and shute wires are different, it is a common procedure for Dutch weaves to express mesh number

along the width and the length separately. Mesh number can increase up to 80x700 in a plain Dutch weave. It should be also noted that increase in the number of wire mesh generally results in the reduction of wire diameter.

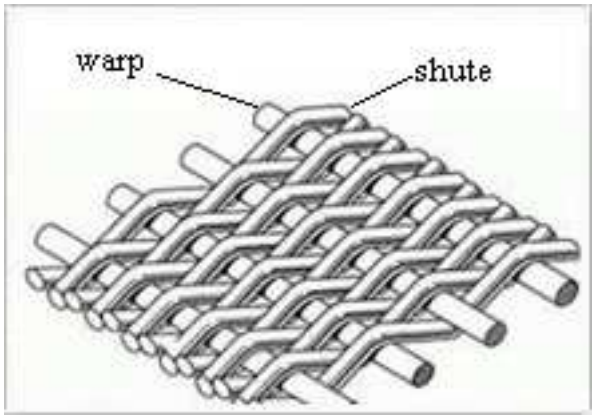

Figure 2.3 Plain Dutch Weave Terminology

2.2 Test Results of Plain Dutch Weave

In search of a proper metal cloth for the new seal design, a market research has been conducted to identify domestically available stainless cloth weaves. Three plain Dutch weaves which have different in mesh numbers per linear inch were selected as candidates for the cloth structure to connect the seal ring to the stationary shroud wall as in Figure 2.1. Wire mesh numbers for these cloths are 24x110, 30x150 and 50x250. Samples of these three wire meshes were prepared and subjected to tensile test to determine stiffness values for each weave. The purpose of this tensile test is to get an insight about the flexibility of the metal cloth in the seal assembly illustrated in Figure 2.8. The collected metal cloth pieces were cut into samples in such a way that wrap and shute wires are diagonally oriented, i.e. 45^{o} with respect to the pulling direction. When a force applied on a cloth weave in diagonal orientation, it causes mesh to distort before pulling on wrap or shute wires, thereby reducing the stiffness. Therefore, diagonal use of metal cloth weave is preferred in applications. Deformation of the samples after the tensile test is demonstrated in Figure 2.4.

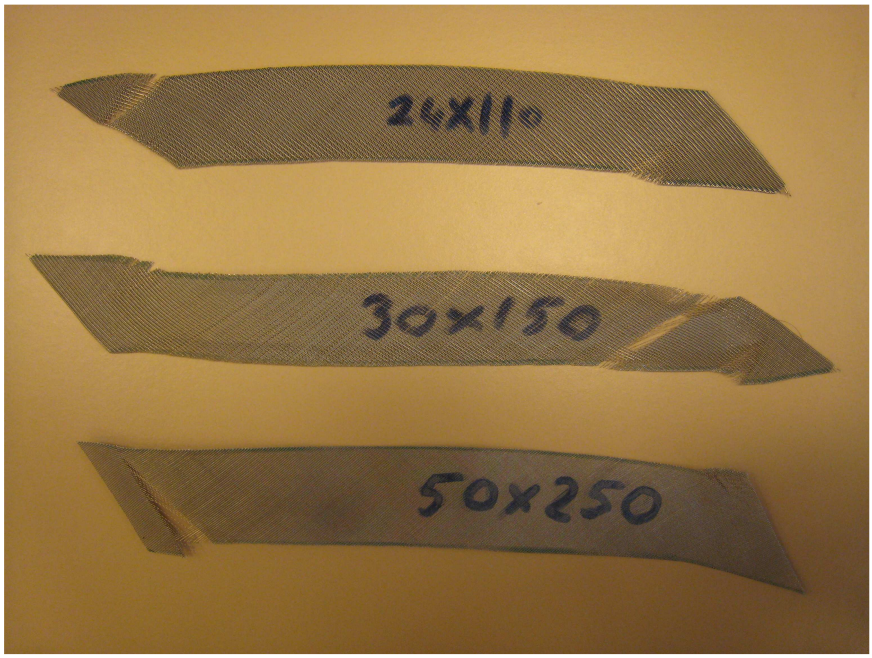

Figure 2.4 Deformed metal cloth samples after tensile tests

Force-deformation results obtained from the tensile test are illustrated in Figures 2.5, 2.6 and 2.7. Red and green curves on each graph stand for the two different samples of the same cloth mesh. Two samples of each cloth type were subjected to tensile test, and an average of the elastic modulus results is taken. Elastic modulus values are illustrated in Table 2.1. It is observed that the elastic modulus at the beginning of the tensile test is lower than the elastic modulus obtained when the elongation is about 8-10% of the original length. It is also observed that the elastic modulus of the metal cloth is on the order of 100 MPa while the elastic moduli of common steel alloys are around 200 GPa. The results draw attention to the fact that metal cloth is very flexible and would produce very small resisting force against the aerodynamic lift action of the fluid film. Due to frictional wire mesh interactions, metal cloth weave is expected to keep the overall system mechanically stable as it has a good damping property. Natural frequency analysis of the seal design is carried out in Chapter 5.

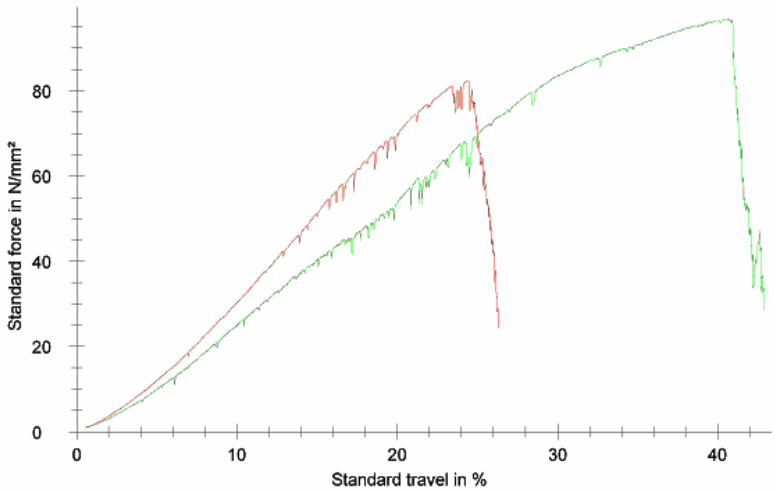

Figure 2.5 Stress-strain curve for 50x250 wire mesh

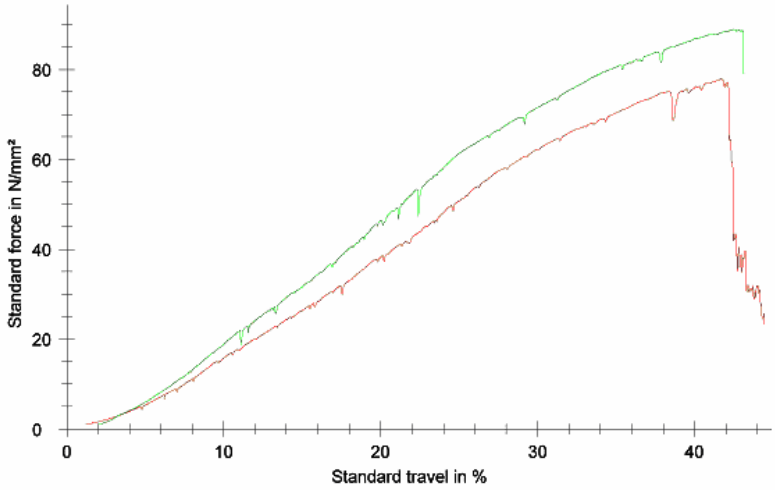

Figure 2.6 Stress-strain curve for 30x150 wire mesh

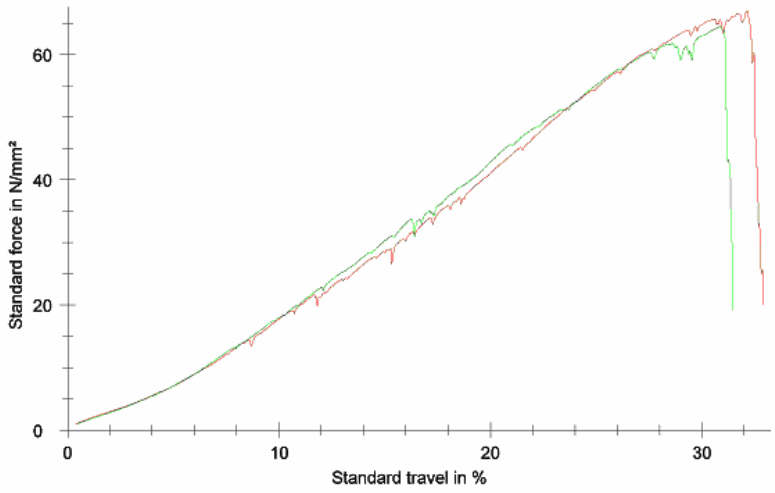

Figure 2.7 Stress-strain curve for 24x110 wire mesh

		F (2.1%) MPa	F (3%) MPa	F (8%) MPa	F (10%) MPa	Elastic Modulus (2.1% - 3%) MPa	Elastic Modulus (8% - 10%) MPa
SAMPLE	50x250	3,39	5,61	21,03	27,22	222,29	309,5
	30x150	1,35	2,46	12,17	16,75	123,37	229
	24x110	2,96	4,04	13,03	17,76	120,37	236,5

Table 2.1 Tensile test results of metal cloth samples

Table 2.1 illustrates that the cloth sample with 50x250 wire meshes has the highest elastic modulus. However, cloth thickness of the same sample is around 0.3 mm. Cloth seals manufactured from thin wires are more vulnerable to oxidation at high temperatures. The other two cloth samples have similar values of elastic modulus. Their thickness values are 0.5 mm. and 0.71 mm. respectively for 30x150 and 24x110 wire mesh sizes. Taking into account that the oxidation rates are increased at high temperatures, 24x110 wire mesh will be more durable against oxidative wear due to its larger wire size. Thus, 24x110 wire mesh is selected as the metal cloth for our gas seal assembly.

2.3 Structure of Shaft-Seal Assembly Coupled with Cloth Metal

The proposed seal is meant for applications where pressure zones are present around rotating bodies. Figure 2.8 demonstrates the shaft-seal assembly mounted on a stationary wall representing a shroud feature that acts as a barrier between high and low pressure cavities. The seal ring is located at the high pressure side of the stationary support. Cross section of the seal assembly without a shaft can be seen in Figure 2.9.

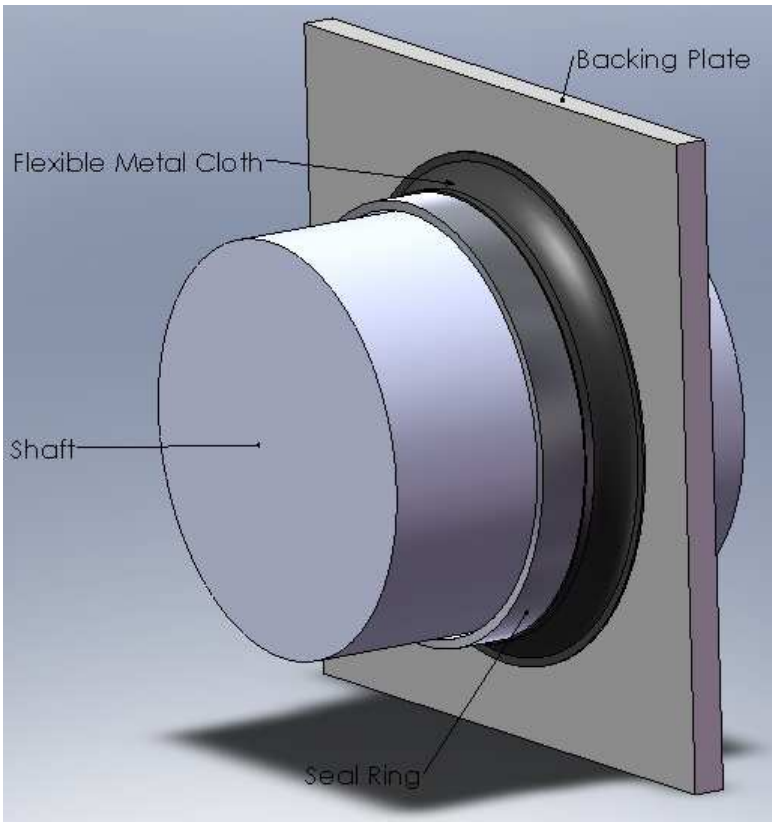

Figure 2.8 Trimetric view of shaft-seal assembly

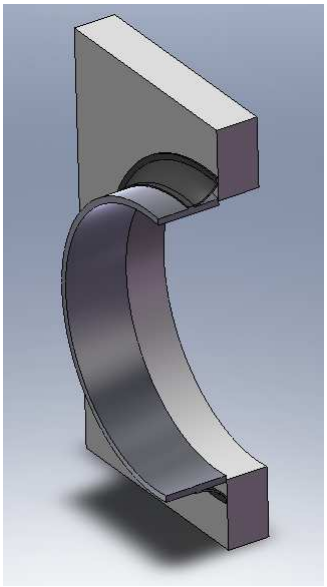

Figure 2.9 Trimetric view of the seal cross section

Mounting clearance between the shaft and the seal ring is around 50 μm. Since the ratio of the clearance to the shaft diameter is on the order of 0.001, this clearance can not be noticed from the figures. In fact, a clearance does exist and an aerodynamic force is developed by the relative motion of the rotating surfaces. A detailed cross sectional

view of the shaft-seal assembly can be seen in Figure 2.10. Metal cloth layer connects the seal ring to the backing plate as illustrated in this figure. There is no direct coupling between the seal ring and the backing plate. When both sides of the seal are exposed to the same ambient pressure, there is no axial force acting on the seal ring assembly which can move freely in response to the dynamic movement of the rotor. When a differential pressure load is applied, seal ring is axially loaded against the backing plate as illustrated in Figure 2.10. In this case, the movement of the seal ring is resisted by the friction force between the seal ring and the backing plate. If the aerodynamic force acting on the seal ring is equal or higher than this frictional resistance, seal ring can move with rotor in the radial direction and possible rotor damage can be avoided. This force balance is analyzed in detail later in Chapter 5. Eccentricity ratio of the shaft to create the required lift force to push the seal in the direction of motion is evaluated. Calculations for seal ring axial width to satisfy minimum film thickness requirements are presented.

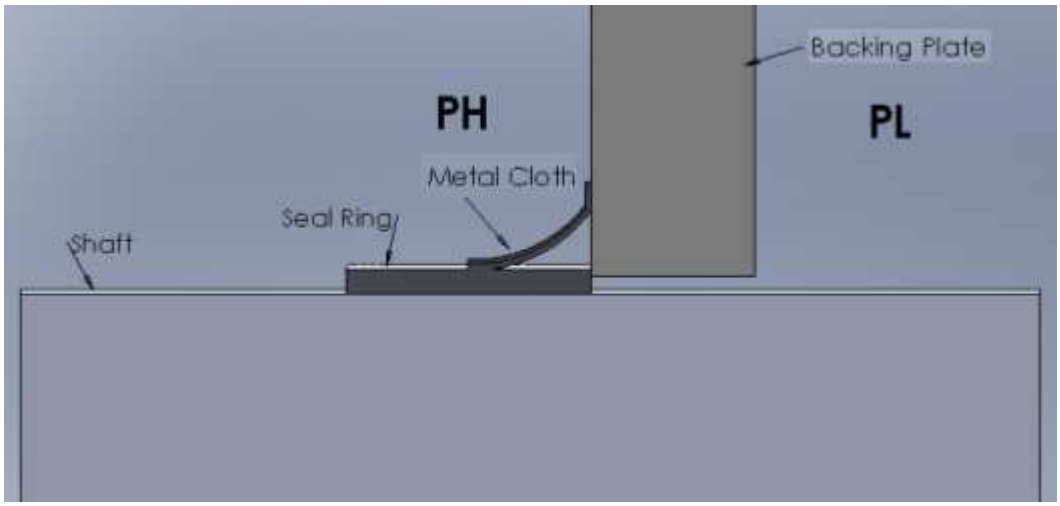

Figure 2.10 Side view of the shaft-seal assembly

For a typical shaft diameter of 5.1 in., i.e. 13 cm, a technical sketch of the seal assembly is presented in Figure 2.11. Although the width of the seal ring is represented as 3 cm, it can vary depending on the shaft size and operating conditions. Thickness of the seal ring is 3 mm. Metal cloth is modeled as a solid structure, and the cloth thickness is equal to 0.71 mm. Mounting clearance between the shaft and the backing plate is 2 mm. However, these values are for a sample case, and can change according to application limitations. Application limitations are dependent on temperature, pressure and free place around the shaft.

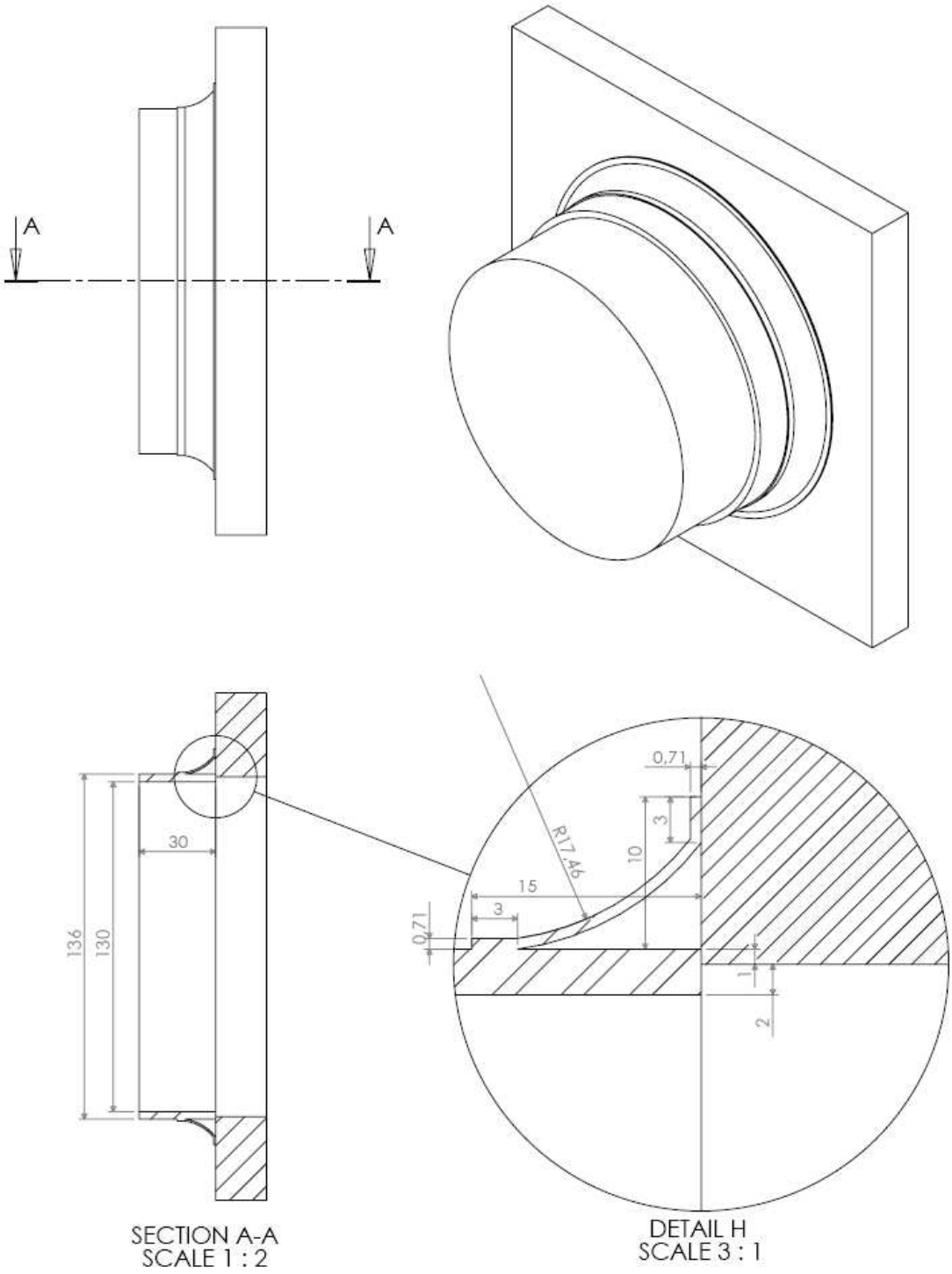

Figure 2.11 Technical sketch for a sample seal

3 ANALYSIS OF AERODYNAMIC LIFT PRESSURE DISTRIBUTION

There are common solution procedures for the pressure distribution of oil lubricated journal bearings in the literature. Closed form analytic solutions are obtainable for short-bearing and long-bearing assumptions when the sealing medium is oil. If length-to-diameter ratio of oil bearings is less than ½, short bearing assumption is applicable to solve the governing equation. Similarly, if length-to-diameter ratio is higher than 2, long bearing assumption is valid. By applying one of these assumptions, the governing equation is put into a reduced form that gives way to a closed form analytical solution for the oil lubrication problem. For the oil lubricated finite journal bearings, where length-to-diameter ratio is between ½ and 2, analytical solutions to the governing Reynolds equation are not normally available, and numerical methods are required [40]. Governing equation for finite journal bearings is often solved by using a relaxation method. The key point in relaxation methods is to replace the derivatives in Reynolds equation by finite difference approximations. Raimondi and Boyd [41] present solution procedures for oil lubricated finite journal bearings. They illustrate various performance charts for different length-to-diameter ratios. For the finite journal bearing, the results of performance parameters such as load capacity, attitude angle and friction force are presented as a function of operating parameters.

Governing equation for oil lubricated bearings assumes the use of incompressible fluids. However, in gas lubricated bearings, the lubricant is compressible. This leads to a modified nonlinear Reynolds equation for the gas lubricated journal bearings. Analytical solutions to the modified Reynolds equation for gas lubricated journal bearings exist only for extremely low and high surface speeds assuming no side flow [6]. Approximate analytical solutions to the full Reynolds equation of gas lubricated journal bearings are also available in the literature. Linearization of nonlinear terms is common procedure in these works. Ausman [32] uses a perturbation approach to solve the nonlinear Reynolds equation. Another approach to solve the nonlinear Reynolds

equation analytically is the linearized ph approach [33]. However, both of these approaches are limited in the sense that the results are in good agreement only for specific ranges of eccentricity ratios. Numerical approaches are required to get a complete solution of the nonlinear Reynolds equation for gas lubricated journal bearings.

3.1 Derivation of Reynolds Equation for Gas Lubricated Journal Bearings

3.1.1 Solution to Continuity and Navier-Stokes Equations

Nonlinear partial differential elliptic equations for gas lubricated journal bearings are originated from continuity and Navier-Stokes equations of compressible Newtonian fluids. The velocity gradient in Newtonian fluids is linearly related to the shearing stress. Almost all lubricating fluids are Newtonian.

Continuity and Navier-Stokes equations for compressible Newtonian fluids are expressed in vector form as:

$$\frac{\partial \rho}{\partial t} + \nabla \cdot (\rho \mathbf{V}) = 0 \tag{3.1}$$

$$\rho\left(\frac{\partial \mathbf{V}}{\partial t} + \mathbf{V} \cdot \nabla \mathbf{V}\right) = -\nabla P + \mu \nabla^2 \mathbf{V} + \mathbf{F} + \left(\mu + \mu_b\right) \nabla \left(\nabla \cdot \mathbf{V}\right) \tag{3.2}$$

where μ and μ_b stand for dynamic viscosity and bulk viscosity respectively and $\mathbf{F}$ represents body forces. Mass density is ρ, absolute pressure is P, time is t, and velocity is $\mathbf{V} = \mathbf{i}u + \mathbf{j}v + \mathbf{k}w$. Last term on the right hand side of equation (3.2) is an addition for compressible fluids to the Navier Stokes equation of incompressible flow (3.3):

$$\rho\left(\frac{\partial \mathbf{V}}{\partial t} + \mathbf{V} \cdot \nabla \mathbf{V}\right) = -\nabla P + \mu \nabla^2 \mathbf{V} + \mathbf{F} \tag{3.3}$$

Stokes makes an idealization for compressible fluids and assumes that pressure is independent of dilation. As a consequence, a relation between dynamic viscosity and bulk viscosity can be stated as follows:

$$2\mu + 3\mu_b = 0 \tag{3.4}$$

Based on this relation and neglecting the body forces, which are negligible in a lubricating film, the equations (3.1) and (3.2) can be written explicitly for 3 spatial dimensions as follows:

$$\frac{\partial \rho}{\partial t}+\frac{\partial}{\partial x}(\rho u)+\frac{\partial}{\partial y}(\rho v)+\frac{\partial}{\partial z}(\rho w)=0 \tag{3.5}$$

$$\begin{aligned}\rho\left(\frac{\partial u}{\partial t}+u\frac{\partial u}{\partial x}+v\frac{\partial u}{\partial y}+w\frac{\partial u}{\partial z}\right)=&-\frac{\partial P}{\partial x}+\frac{2}{3}\frac{\partial}{\partial x}\left\{\mu\left[3\frac{\partial u}{\partial x}-\left(\frac{\partial u}{\partial x}+\frac{\partial v}{\partial y}+\frac{\partial w}{\partial z}\right)\right]\right\}\\&+\frac{\partial}{\partial y}\left[\mu\left(\frac{\partial u}{\partial y}+\frac{\partial v}{\partial x}\right)\right]+\frac{\partial}{\partial z}\left[\mu\left(\frac{\partial w}{\partial x}+\frac{\partial u}{\partial z}\right)\right]\end{aligned} \tag{3.6}$$

$$\begin{aligned}\rho\left(\frac{\partial v}{\partial t}+u\frac{\partial v}{\partial x}+v\frac{\partial v}{\partial y}+w\frac{\partial v}{\partial z}\right)=&-\frac{\partial P}{\partial y}+\frac{2}{3}\frac{\partial}{\partial y}\left\{\mu\left[3\frac{\partial v}{\partial y}-\left(\frac{\partial u}{\partial x}+\frac{\partial v}{\partial y}+\frac{\partial w}{\partial z}\right)\right]\right\}\\&+\frac{\partial}{\partial z}\left[\mu\left(\frac{\partial v}{\partial z}+\frac{\partial w}{\partial y}\right)\right]+\frac{\partial}{\partial x}\left[\mu\left(\frac{\partial u}{\partial y}+\frac{\partial v}{\partial x}\right)\right]\end{aligned} \tag{3.7}$$

$$\begin{aligned}\rho\left(\frac{\partial w}{\partial t}+u\frac{\partial w}{\partial x}+v\frac{\partial w}{\partial y}+w\frac{\partial w}{\partial z}\right)=&-\frac{\partial P}{\partial z}+\frac{2}{3}\frac{\partial}{\partial z}\left\{\mu\left[3\frac{\partial w}{\partial z}-\left(\frac{\partial u}{\partial x}+\frac{\partial v}{\partial y}+\frac{\partial w}{\partial z}\right)\right]\right\}\\&+\frac{\partial}{\partial x}\left[\mu\left(\frac{\partial w}{\partial x}+\frac{\partial u}{\partial z}\right)\right]+\frac{\partial}{\partial y}\left[\mu\left(\frac{\partial v}{\partial z}+\frac{\partial w}{\partial y}\right)\right]\end{aligned} \tag{3.8}$$

Considering that ideal gas law holds for the lubricating gas film, density of gas can be expressed in terms of film pressure as follows:

$$PV=NRT\rightarrow PV=(M/M_a)RT\rightarrow \rho=\frac{M}{V}=P\left(\frac{M_a}{RT}\right) \tag{3.9}$$

M, *V* and *N* are related to the quantity of the gas. However, for a specific gas in a steady environment, M_a, *R*, and *T* are independent of gas quantity and can be taken as constant. Therefore, for a specific gas, such as air, a direct relationship between the density and the pressure can be defined. This relation reduces the number of unknowns in momentum equations to four, which are *P, u, v* and *w*. As a result, we have four equations, including the continuity equation, and four unknowns, and therefore the problem is well posed in mathematical terms. Although the problem is well posed, nonlinear, second order, partial differential structure of Navier-Stokes equations makes it very difficult to get exact solutions except in a few special instances. A series of simplifications to these Navier-Stokes equations must be performed to solve the gas

film lubrication problem. Simplification of the equations requires order of magnitude analysis on the variables.

In order to start the order of magnitude analysis, we must first note that the vertical component of the velocity, *w*, is very small when compared with the horizontal components, *u*, *and v*. The ratio *w/u* has the same magnitude as the inclination between the bearing surfaces. Due to the fact that there is a slight inclination between the bearing surfaces, vertical component of the velocity is expected to be very low and can be ignored from the equations. After removing the terms related to *w* from the equations (3.6), (3.7) and (3.8), these equations can be written in a more compact and simple form as

$$\rho\left(\frac{\partial u}{\partial t}+u\frac{\partial u}{\partial x}+v\frac{\partial u}{\partial y}\right)=-\frac{\partial P}{\partial x}+\mu\left(\frac{1}{3}\frac{\partial^2 v}{\partial x\partial y}+\frac{4}{3}\frac{\partial^2 u}{\partial x^2}+\frac{\partial^2 u}{\partial y^2}+\frac{\partial^2 u}{\partial z^2}\right) \tag{3.10}$$

$$\rho\left(\frac{\partial v}{\partial t}+u\frac{\partial v}{\partial x}+v\frac{\partial v}{\partial y}\right)=-\frac{\partial P}{\partial y}+\mu\left(\frac{1}{3}\frac{\partial^2 u}{\partial x\partial y}+\frac{4}{3}\frac{\partial^2 v}{\partial y^2}+\frac{\partial^2 v}{\partial x^2}+\frac{\partial^2 v}{\partial z^2}\right) \tag{3.11}$$

$$0=-\frac{\partial P}{\partial z}+\mu\frac{1}{3}\left(\frac{\partial^2 u}{\partial x\partial z}+\frac{\partial^2 v}{\partial y\partial z}\right) \tag{3.12}$$

For a typical finite journal bearing, the dimensions of bearing geometry can be scaled as follows

$$L,\ B >> h \tag{3.13}$$

where *L* is the circumferential length and *B* is the width/axial length of bearing.

A scaling between *L* and *B* for a journal bearing is not obvious because of the fact that infinitely many design combinations can be created varying *L* and *B* values. However, for a finite journal bearing, these two variables are almost in the same order of magnitude. An order of magnitude difference between *L* and *B* does not create a dilemma for the simplification of the momentum equations because of the fact the determining factor for the order of magnitude test is the ratio of fluid film gap distance, h, to the other variables. Magnitude of fluid film gap, *h*, is extremely small with respect to other dimension variables. Typical scale factors of *h* with respect to other variables are

$$\frac{h}{L}\sim 10^{-4},\frac{h}{B}\sim 10^{-3} \tag{3.14}$$

If we apply order of magnitude analysis on the second order partial differential operators, following scaling relations are obtained.

$$\frac{\partial^2}{\partial x^2} \sim \frac{1}{L^2} \tag{3.15}$$

$$\frac{\partial^2}{\partial y^2} \sim \frac{1}{B^2} \tag{3.16}$$

$$\frac{\partial^2}{\partial z^2} \sim \frac{1}{h^2} \tag{3.17}$$

$$\frac{\partial^2}{\partial x \partial y} \sim \frac{1}{LB} \tag{3.18}$$

Order of magnitude test indicates that

$$\frac{\partial^2}{\partial x^2}, \frac{\partial^2}{\partial y^2}, \frac{\partial^2}{\partial x \partial y} << \frac{\partial^2}{\partial z^2} \tag{3.19}$$

So the terms, $\frac{\partial^2 u}{\partial x^2}, \frac{\partial^2 u}{\partial y^2}, \frac{\partial^2 u}{\partial x \partial y}, \frac{\partial^2 v}{\partial x^2}, \frac{\partial^2 v}{\partial y^2}, \frac{\partial^2 v}{\partial x \partial y}$ in the equations (3.10) and (3.11) are very small with respect to $\frac{\partial^2 u}{\partial z^2}$ and $\frac{\partial^2 v}{\partial z^2}$, and can be neglected.

$$\rho\left(\frac{\partial u}{\partial t} + u\frac{\partial u}{\partial x} + v\frac{\partial u}{\partial y}\right) = -\frac{\partial P}{\partial x} + \mu\left(\frac{1}{3}\frac{\partial^2 v}{\partial x \partial y} + \frac{4}{3}\frac{\partial^2 u}{\partial x^2} + \frac{\partial^2 u}{\partial y^2} + \frac{\partial^2 u}{\partial z^2}\right) \tag{3.20}$$

$$\rho\left(\frac{\partial v}{\partial t} + u\frac{\partial v}{\partial x} + v\frac{\partial v}{\partial y}\right) = -\frac{\partial P}{\partial y} + \mu\left(\frac{1}{3}\frac{\partial^2 u}{\partial x \partial y} + \frac{4}{3}\frac{\partial^2 v}{\partial y^2} + \frac{\partial^2 v}{\partial x^2} + \frac{\partial^2 v}{\partial z^2}\right) \tag{3.21}$$

However, orders of magnitudes of the differential terms, $\frac{\partial^2 u}{\partial x \partial z}$ and $\frac{\partial^2 v}{\partial y \partial z}$, in equation (3.12) are comparable so that none of the terms are removed from the equation. Thus, the momentum equations reduce to

$$\rho\left(\frac{\partial u}{\partial t} + u\frac{\partial u}{\partial x} + v\frac{\partial u}{\partial y}\right) = -\frac{\partial P}{\partial x} + \mu\frac{\partial^2 u}{\partial z^2} \tag{3.22}$$

$$\rho\left(\frac{\partial v}{\partial t} + u\frac{\partial v}{\partial x} + v\frac{\partial v}{\partial y}\right) = -\frac{\partial P}{\partial y} + \mu\frac{\partial^2 v}{\partial z^2} \tag{3.23}$$

$$0 = -\frac{\partial P}{\partial z} + \mu\frac{1}{3}\left(\frac{\partial^2 u}{\partial x \partial z} + \frac{\partial^2 v}{\partial y \partial z}\right) \tag{3.24}$$

The equations above can be expressed in non-dimensional form by normalizing film velocities with respect to surface velocities along the corresponding directions, distances with respect to corresponding bearing dimensions, pressure with respect to $\mu\frac{UL}{h^2}$ and time with respect to L/U such that;

$$u \sim U \;\rightarrow\; u^* = \frac{u}{U} \text{ and } u = Uu^*$$

$$v \sim U\frac{B}{L} \;\rightarrow\; v^* = \frac{v}{U}\cdot\frac{L}{B} \text{ and } v = \frac{UB}{L}v^*$$

$$x^* = \frac{x}{L} \;\rightarrow\; x = Lx^*$$

$$y^* = \frac{y}{B} \;\rightarrow\; y = By^*$$

$$P^* = \frac{P}{\mu\frac{UL}{h^2}} \;\rightarrow\; P = \mu\frac{UL}{h^2}P^*$$

$$t^* = \frac{t}{L/U} \;\rightarrow\; t = \frac{L}{U}t^*$$

Applying the normalization factors to Equations 3.22 to 3.24 the following equations in non-dimensional form are obtained:

$$\rho\frac{U^2}{L}\left(\frac{\partial u^*}{\partial t^*} + u^*\frac{\partial u^*}{\partial x^*} + v^*\frac{\partial u^*}{\partial y^*}\right) = \mu\frac{U}{h^2}\left(-\frac{\partial P^*}{\partial x^*} + \frac{\partial^2 u^*}{\partial z^{*2}}\right) \tag{3.25}$$

$$\rho\frac{U^2B}{L^2}\left(\frac{\partial v^*}{\partial t^*} + u^*\frac{\partial v^*}{\partial x^*} + v^*\frac{\partial v^*}{\partial y^*}\right) = -\mu\frac{UL}{h^2B}\frac{\partial P^*}{\partial y^*} + \mu\frac{UB}{h^2L}\frac{\partial^2 v^*}{\partial z^{*2}} \tag{3.26}$$

$$0 = -\mu\frac{UL}{h^3}\frac{\partial P^*}{\partial z^*} + \frac{1}{3}\mu\frac{U}{Lh}\left(\frac{\partial^2 u^*}{\partial x^*\partial z^*} + \frac{\partial^2 v^*}{\partial y^*\partial z^*}\right) \tag{3.27}$$

In the final form above, the coefficients are still dimensional. To get rid of these dimensional terms, equations (3.25), (3.26) and (3.27) are divided respectively by $\mu\frac{U}{h^2}$, $\mu\frac{UB}{h^2L}$ and $\mu\frac{UL}{h^3}$. The resultant equations are fully non-dimensional:

$$\frac{\rho Uh}{\mu}\frac{h}{L}\left(\frac{\partial u^*}{\partial t^*} + u^*\frac{\partial u^*}{\partial x^*} + v^*\frac{\partial u^*}{\partial y^*}\right) = -\frac{\partial P^*}{\partial x^*} + \frac{\partial^2 u^*}{\partial z^{*2}} \tag{3.28}$$

$$\frac{\rho Uh}{\mu}\frac{h}{L}\left(\frac{\partial v^*}{\partial t^*} + u^*\frac{\partial v^*}{\partial x^*} + v^*\frac{\partial v^*}{\partial y^*}\right) = -\frac{L^2}{B^2}\frac{\partial P^*}{\partial y^*} + \frac{\partial^2 v^*}{\partial z^{*2}} \tag{3.29}$$

$$0 = -\frac{\partial P^*}{\partial z^*} + \frac{1}{3}\frac{h^2}{L^2}\left(\frac{\partial^2 u^*}{\partial x^*\partial z^*} + \frac{\partial^2 v^*}{\partial y^*\partial z^*}\right) \tag{3.30}$$

The term, $\frac{\rho U h}{\mu}$, located at the leftmost of the equations (3.28) and (3.29) corresponds to the Reynolds number for which the characteristic length is the aerodynamic lift clearance of the journal bearing. For a gas turbine journal bearing operating at high temperatures and high ambient pressures, the following typical parameters can be defined:

$T = 1000\ F°$

$P_a = 700\ KPa$

$\rho = 0.4363\ kg/m^3$

$\mu = 3.751e-5\ N-s/m^2$

$h = 50\ \mu m$

$D = 5.1\ in. \ \rightarrow \ L = 2\pi r = 0.407\ m.$

$w = 10000\ rpm = 1047\ rad/s \ \rightarrow \ U = 68.067\ m/s$

Then, we obtain

$$\mathrm{Re} \approx 39 < 2300$$

ensuring that the flow is laminar. Also, the scaled Reynolds number becomes

$$\mathrm{Re} \cdot \frac{h}{L} = \frac{\rho U h}{\mu}\frac{h}{L} = 39 \cdot \frac{50e-6}{0.407} \approx 0.0048 << 1$$

Since the scaled Reynolds number is very small with respect to unity, inertial terms on the left side of the equations (3.28) and (3.29) can be neglected. Also, $\frac{h^2}{L^2}$,which is located at the right hand side of (3.30) is very small, and the term multiplied with it can also be neglected. Therefore, the remaining simplified non-dimensional equations are

$$0 = -\frac{\partial P^*}{\partial x^*} + \frac{\partial^2 u^*}{\partial z^{*2}} \tag{3.31}$$

$$0 = -\frac{L^2}{B^2}\frac{\partial P^*}{\partial y^*} + \frac{\partial^2 v^*}{\partial z^{*2}} \tag{3.32}$$

$$0 = \frac{\partial P^*}{\partial z^*} \tag{3.33}$$

Finally, reduced Navier-Stokes equations (3.31), (3.32) and (3.33) can be expressed in dimensional form as

$$0 = -\frac{\partial P}{\partial x} + \mu\frac{\partial^2 u}{\partial z^2} \tag{3.34}$$

$$0 = -\frac{\partial P}{\partial y} + \mu \frac{\partial^2 v}{\partial z^2} \tag{3.35}$$

$$0 = \frac{\partial P}{\partial z} \tag{3.36}$$

One last step is needed to derive the governing equations for gas film lubrication. Velocities on the bearing boundaries are determined according to the results of flow regime analysis.

3.1.2 Analysis of Flow Regime

The next step is to obtain the velocity profiles in x and y directions from the equations (3.34) and (3.35). In order to solve the equations 3.34 and 3.35 for the velocity profiles, boundary conditions should be properly defined. Characteristics of film velocities at the boundaries of a bearing/seal/shaft are related to the flow regime of the fluid film. The application of continuum flow theory requires no-slip conditions at the boundaries. If no-slip conditions are valid, fluid velocity at the boundaries of bearing is equal to the driving surface velocity. In other words, there is no relative difference between the fluid velocity and surface velocity. If the gas film flow takes place in the slip region, velocity of gas molecules on the boundary surfaces are not equal to the driving surface velocities, and there exists a slip velocity. In such a case, additional velocity relations are required to define the slip velocities on the boundaries. Film velocity across the boundary surfaces is not distributed linearly, and continuum flow theory fails.

To determine whether the flow is in slip region or not, we should evaluate the Knudsen number, Kn. Knudsen number is a measure of average number of collisions of gas molecules in a given length, and defined as

$$Kn = \beta / h \tag{3.37}$$

where

β = molecular mean free path of gas molecules

h = film thickness

When the mean free path of molecules becomes comparable to the film thickness, the fluid does not behave as a continuous fluid but rather exhibits some characteristics

of its molecular chaos. The criteria for the boundaries of flow regimes with respect to Knudsen number can be defined as follows [42]:

No-slip (continuum) flow: $Kn < 0.01$

Slip flow: $0.01 < Kn < 3$

Transition flow: $3 < Kn, \quad Kn/(Re)^{1/2} < 10$

Free-molecular flow: $10 < Kn/(Re)^{1/2}$

Gas lubrication with-ultra thin films may exhibit slip flow [42], [43]. Moreover, Bhushan [5] states that, in the slip-flow regime, the flow may still be treated by conventional continuum theories but with modified boundary conditions. In other words, in the slip-flow regime, the flow can still be governed by continuum flow theories but instead of vanishing velocities at the boundaries, slip velocities should be introduced. Burgdorfer [44] investigates the effect of molecular mean free path on the performance of gas lubricated bearings. He suggests that the continuum theory can be applied for slip-flow regime unless the minimum film thickness is lower than the mean free path of the gas. Moreover, Burgdorfer emphasizes that the load carrying capacity of bearing and friction coefficient of gas film decrease with increasing value of Knudsen number in slip-flow regime.

In order to identify the flow regime of gas film for the journal bearing for which the operating conditions are illustrated above, we should first evaluate the molecular mean free path of air. The molecular mean free path can be defined by various models as follows [45]:

Model	k	$\beta = k\dfrac{\mu}{\rho\sqrt{RT}}$
HS	$\dfrac{16}{5\sqrt{2\pi}} \approx 1.277$	0.032×10^{-6}
MM	$\sqrt{\dfrac{2}{\pi}} \approx 0.798$	0.02×10^{-6}

Table 3.1 Mean free path calculation with HS and MM Models

HS and MM stand for hard sphere and Maxwell molecules models respectively. Mean free paths of various gases can be evaluated using these two models. For an air film at $1000\ ^{\circ}F$ and $700\ KPa$, values of mean free paths are demonstrated in Table 3.1. There are other models such as VHS (variable hard sphere) and VSS (variable soft

sphere) to evaluate the mean free path. Kandlikar et. al. state that the HS and the MM models may be considered as the limits of VHS model. Therefore, in our application, mean free path of air using VHS model would be varying between the values illustrated in Table 3.1 On the other hand, Kanlikar et. al. [45] indicate that VSS model leads to a correction of the mean free path calculated by VHS model. He points that the correction introduced by the VSS model in the mean free path and in the collision rate remains limited, less than %3. Therefore, values of mean free path of air calculated by HS and MM methods are sufficient to determine the characteristic of flow regime.

To evaluate the Knudsen number, gas film thickness is needed as the second parameter. For our journal bearing configuration, film thickness, h, is variable along the circumferential direction due to the eccentricity of journal. A constant nominal value of film thickness should be determined for use in the formulation of Knudsen number. Hence, mounting clearance of bearing, c, which is equal to 50 μm, is taken as the nominal value of film thickness, h. Knudsen numbers with the mean free path values obtained from two different models are calculated as follows:

$$Kn_{HS} = \frac{\beta_{HS}}{h_{nom}} \rightarrow Kn_{HS} = \frac{0.032\times10^{-6}}{50\times10^{-6}} = 6.4\times10^{-4} < 0.01 \tag{3.38}$$

$$Kn_{MM} = \frac{\beta_{MM}}{h_{nom}} \rightarrow Kn_{MM} = \frac{0.02\times10^{-6}}{50\times10^{-6}} = 4\times10^{-4} < 0.01 \tag{3.39}$$

Resultant Knudsen numbers reveal that no-slip condition occurs at the boundaries and continuum flow theory can be adopted without any complications. To make a local analysis of flow regimes, instead of calculating Knudsen number for nominal film thickness, we can calculate the Knudsen number at the minimum film thickness. For the same journal bearing which has a 50 μm mounting clearance, an eccentricity ratio of 0.9 (eccentricity ratio of 1 means physical contact between journal and bearing) results in a minimum film thickness of 5 μm. In this case, Knudsen numbers are still below the limiting number, 0.01, but the difference is considerably reduced. As a result, it is realized that no-slip boundary conditions can be applied for our problem, and velocity profiles along x and y directions can be obtained accordingly.

3.1.3 Application of Boundary Conditions and Resulting Reynolds Equation

Assuming no-slip conditions and laminar flow, boundary conditions for equations (3.34) and (3.35) can be defined as

$$\begin{aligned} 0 &= -\frac{\partial P}{\partial x} + \mu \frac{\partial^2 u}{\partial z^2} \\ z &= 0,\ u = U \\ z &= h(x),\ u = 0 \end{aligned} \tag{3.40}$$

$$\begin{aligned} 0 &= -\frac{\partial P}{\partial y} + \mu \frac{\partial^2 v}{\partial z^2} \\ z &= 0,\ v = 0 \\ z &= h(x),\ v = 0 \end{aligned} \tag{3.41}$$

By solving the equations in the sets (3.40) and (3.41) with the defined boundary conditions, velocity profiles in x and y directions are obtained as

$$u = \frac{1}{2\mu}\frac{\partial P}{\partial x}\left(z^2 - zh\right) + U\left(1 - \frac{z}{h}\right) \tag{3.42}$$

$$v = \frac{1}{2\mu}\frac{\partial P}{\partial y}\left(z^2 - zh\right) \tag{3.43}$$

Now, we can plug the resulting equations into the continuity equation (3.3). Integration of continuity equation with respect to z yields,

$$\int_0^{h(x)} \left[\frac{\partial \rho}{\partial t} + \frac{\partial}{\partial x}(\rho u) + \frac{\partial}{\partial y}(\rho v) + \frac{\partial}{\partial z}(\rho w) \right] = 0 \tag{3.44}$$

In steady state conditions, plugging equations (3.42) and (3.43) into (3.44) and taking the integration yields the Reynolds equation for our compressible flow,

$$\frac{\partial}{\partial x}\left(\frac{\rho h^3}{\mu}\frac{\partial P}{\partial x}\right) + \frac{\partial}{\partial y}\left(\frac{\rho h^3}{\mu}\frac{\partial P}{\partial y}\right) = 6U\frac{\partial(\rho h)}{\partial x} \tag{3.45}$$

The above equation governs the characteristics of compressible, laminar, steady state continuum flow with no-slip assumption on the boundaries. As stated before, the equation is highly nonlinear. While the film thickness is dependent on x variable only, pressure and gas density (which can also be defined as a function of pressure) are a function of both x and y dimensions. Multiplication of these terms makes the equation

(3.45) nonlinear. On the other hand, (3.45) is a general equation that governs the characteristics of fluid film in a finite steady journal bearing. No further simplification is made on the equation associated with short-bearing or long bearing theory. Closed form analytical solution to this equation is not available. In the next section, equation (3.45) is solved by using numerical methods, and corresponding pressure profiles are presented.

3.2 Solution to the Governing Reynolds Equation

As stated before, there are 3 dependent variables in Equation (3.45). Variance of viscosity, μ, is very small for gases so it is taken equal to the ambient viscosity. Density, ρ, which is dependent on position, can be defined as a function of pressure. Figure 3.1 illustrates the unwrapped view of journal bearing geometry and the variation of film thickness (Equation 1.2) in the circumferential direction.

As stated before, density can be related to the pressure by multiplying it with a constant term. Therefore, all density terms in (3.45) are replaced by pressure and the constant multiplication terms are dropped. As a result, following equation is obtained.

$$\frac{\partial}{\partial x}\left(\frac{Ph^3}{\mu}\frac{\partial P}{\partial x}\right)+\frac{\partial}{\partial y}\left(\frac{Ph^3}{\mu}\frac{\partial P}{\partial y}\right)=6U\frac{\partial(Ph)}{\partial x} \tag{3.46}$$

Equation (3.46) can be written in non-dimensional form by normalizing x and y variables with respect to journal radius *r*, similarly *P* with respect to ambient pressure P_a, and *h* with respect to clearance *c*.

$$\frac{\partial}{\partial \theta}\left(P_n H^3\frac{\partial P}{\partial \theta}\right)+\frac{\partial}{\partial \varphi}\left(P_n H^3\frac{\partial P_n}{\partial \varphi}\right)=6\lambda\frac{\partial(P_n H)}{\partial \theta} \tag{3.47}$$

where

$$\theta=\frac{x}{r},\varphi=\frac{y}{r},P_n=\frac{P}{P_a},H=\frac{h}{c}\text{ and }\lambda=\left(\frac{r}{c}\right)^2\frac{\mu\omega}{P_a}$$

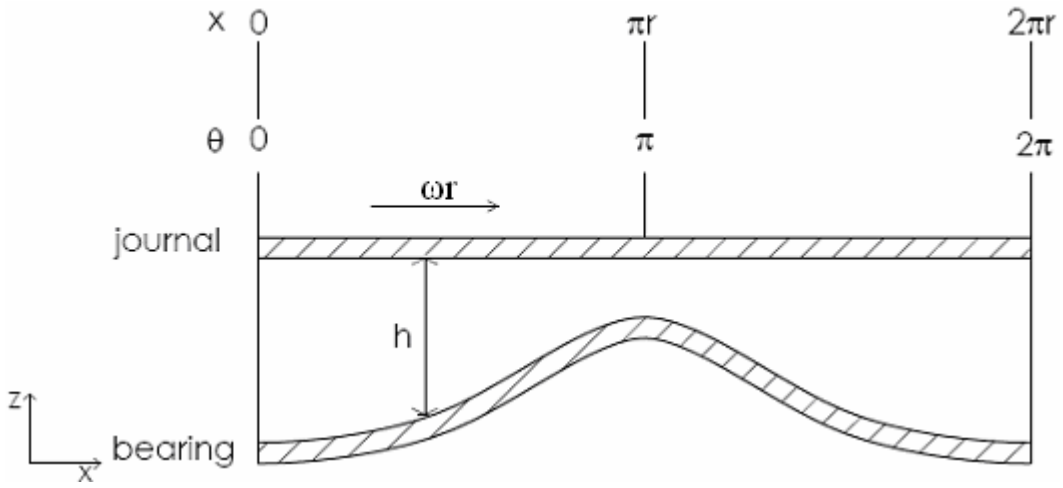

Figure 3.1 Unwrapped film shape of journal bearing

3.2.1 Finite Difference (FD) Approximation for Governing Reynolds Equation

In this section, a finite difference approximation to the Reynolds equation (3.47) is derived. To make it more appropriate for finite difference approximation, equation (3.47) is reformulated as,

$$\frac{1}{2}\frac{\partial}{\partial\theta}\left(H^3\frac{\partial P_n^2}{\partial\theta}\right)+\frac{1}{2}H^3\frac{\partial}{\partial\varphi}\left(\frac{\partial P_n^2}{\partial\varphi}\right)=6\lambda\frac{\partial\left(P_nH\right)}{\partial\theta} \tag{3.48}$$

where

$$\frac{\partial P_n^2}{\partial\theta}=2P_n\frac{\partial P_n}{\partial\theta} \tag{3.49}$$

$$\frac{\partial P_n^2}{\partial\varphi}=2P_n\frac{\partial P_n}{\partial\varphi} \tag{3.50}$$

H is not dependent on φ, and can be taken out from the partial derivative term. However, the first term is dependent on θ, and must be kept in the partial derivative form.

In order to continue with the finite difference approximation, standard basic difference relations could be utilized. Forward, backward and central difference approximations of first order derivatives are represented as,

$$f'(x)\approx\frac{f(x+h)-f(x)}{h}\quad\text{(forward difference)} \tag{3.51}$$

$$f'(x) \approx \frac{f(x)-f(x-h)}{h} \quad \text{(backward difference)} \tag{3.52}$$

$$f'(x) \approx \frac{f(x+h)-f(x-h)}{2h} \quad \text{(central difference)} \tag{3.53}$$

Second order derivatives can be approximated by central difference as,

$$f''(x) \approx \frac{f(x+h)-2f(x)+f(x-h)}{h^2} \tag{3.54}$$

The domain and boundary conditions of Reynolds equation for which the finite difference approximation applied are displayed in Figure 3.2. Similarly, Figure 3.3 illustrates the same domain and boundary conditions in non-dimensional form. Since the domain is a representation of unwrapped bearing surface, we can use a rectangular grid to adopt finite difference approximation. Non-dimensional location of each point in the grid can be presented in θ and φ directions as follows:

$$\theta_i = ib, \quad \text{for } i = 0,1,2,...,n+1 \tag{3.55}$$

$$\varphi_j = ja, \quad \text{for } j = 0,1,2,...,m+1 \tag{3.56}$$

The step sizes are $b = 2\pi / n$ and $a = \dfrac{B}{r(m+1)}$.

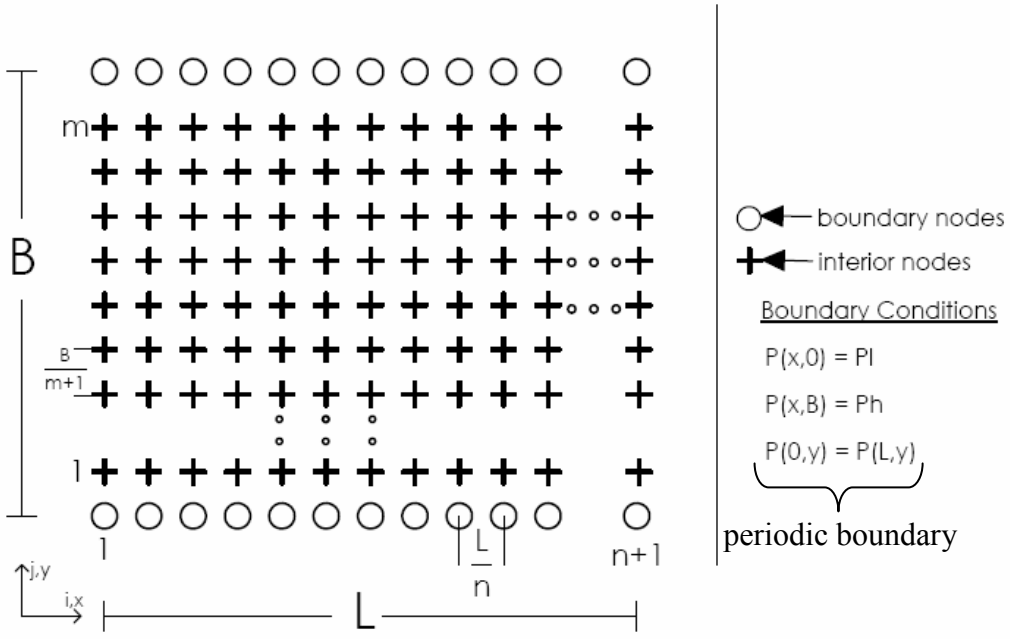

Figure 3.2 Mesh grid for finite difference approximation (dimensional)

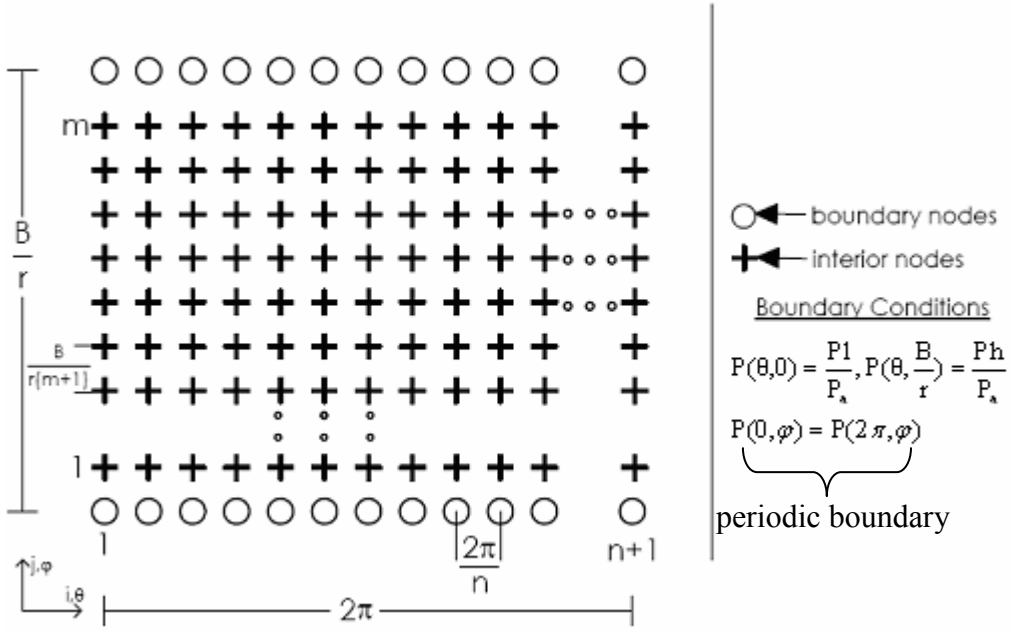

Figure 3.3 Mesh grid for finite difference approximation (non-dimensional)

In preparation for introducing finite difference approximations, we evaluate the Reynolds equation (3.48) at $\left(\theta_i,\varphi_j\right)$ to obtain

$$\underbrace{\frac{1}{2}\frac{\partial}{\partial\theta}\left(H\left(\theta_i\right)^3\frac{\partial P_n\left(\theta_i,\varphi_j\right)^2}{\partial\theta}\right)}_{1^{st}\text{ term}}+\underbrace{\frac{1}{2}H\left(\theta_i\right)^3\frac{\partial}{\partial\varphi}\left(\frac{\partial P_n\left(\theta_i,\varphi_j\right)^2}{\partial\varphi}\right)}_{2^{nd}\text{ term}}=\underbrace{6\lambda\frac{\partial\left(P_n\left(\theta_i,\varphi_j\right)H\left(\theta_i\right)\right)}{\partial\theta}}_{3^{rd}\text{ term}} \tag{3.57}$$

When we use central difference scheme to approximate the derivatives, this gives us

1st term:

$$\frac{3}{2}H^2\left(\theta_i\right)\left(\frac{H\left(\theta_{i+1}\right)-H\left(\theta_{i-1}\right)}{2b}\cdot\frac{P_n^2\left(\theta_{i+1},\varphi_j\right)-P_n^2\left(\theta_{i-1},\varphi_j\right)}{2b}\right)$$
$$+\frac{1}{2}H^3\left(\theta_i\right)\left(\frac{P_n^2\left(\theta_{i+1},\varphi_j\right)-2P_n^2\left(\theta_i,\varphi_j\right)+P_n^2\left(\theta_{i-1},\varphi_j\right)}{b^2}\right) \tag{3.58}$$

2nd term:

$$\frac{1}{2}H^3\left(\theta_i\right)\left(\frac{P_n^2\left(\theta_i,\varphi_{j+1}\right)-2P_n^2\left(\theta_i,\varphi_j\right)+P_n^2\left(\theta_i,\varphi_{j-1}\right)}{a^2}\right) \tag{3.59}$$

3rd term:

$$6\lambda\left[P_n\left(\theta_i,\varphi_j\right)\left(\frac{H\left(\theta_{i+1}\right)-H\left(\theta_{i-1}\right)}{2b}\right)+H\left(\theta_i\right)\left(\frac{P_n\left(\theta_{i+1},\varphi_j\right)-P_n\left(\theta_{i-1},\varphi_j\right)}{2b}\right)\right] \quad (3.60)$$

Writing these three terms in compact form gives us the following finite difference approximation to the governing Reynolds equation

$$\begin{aligned}
&\frac{3}{8b^2}H_i^2\left(H_{i+1}-H_{i-1}\right)\cdot\left(\left(P_n\right)_{i+1,j}^2-\left(P_n\right)_{i-1,j}^2\right)\\
&+\frac{1}{2b^2}H_i^3\left(\left(P_n\right)_{i+1,j}^2-2\left(P_n\right)_{i,j}^2+\left(P_n\right)_{i-1,j}^2\right)\\
&+\frac{1}{2a^2}H_i^3\left(\left(P_n\right)_{i,j+1}^2-2\left(P_n\right)_{i,j}^2+\left(P_n\right)_{i,j-1}^2\right)\\
&-\frac{6\lambda}{2b}\left[\left(P_n\right)_{i,j}\left(H_{i+1}-H_{i-1}\right)+H_i\left(\left(P_n\right)_{i+1,j}-\left(P_n\right)_{i-1,j}\right)\right]=0
\end{aligned} \quad (3.61)$$

Note that there are as many equations as there are points $\left(\theta_i,\varphi_j\right)$ in the region. Due to the periodicity boundary condition (rectangular shape is an unwrapped representation of circular bearing surface), $P_n\left(0,\varphi\right)=P_n\left(2\pi,\varphi\right)$, two sets of vertical points located at $i=1$ and $i=n+1$ have the same pressure values. Similarly, pressures at the boundary nodes on the bottom line (downstream pressure) and on the top line (upstream pressure) are known. Therefore, there is no need to solve for the pressures at these nodes. As a result, $m\times n$ equations (excluding one set of vertical points due to the periodicity) need to be iteratively solved. Then, each point, which is defined by both i and j components, in the grid is renumbered. Fig 3.4 shows the renumbering of points in the grid for a representative case where $m=5$, $n=9$. Note that, periodic nodes are given the same number. Bottom and top boundary nodes are not numbered since their pressure values are known. This numbering scheme is known as a lexicographic ordering [46], and can be formulated as

$$l=(j-1)n+i$$

where

$i=1,2,3,...n$

$j=1,2,3,...m$

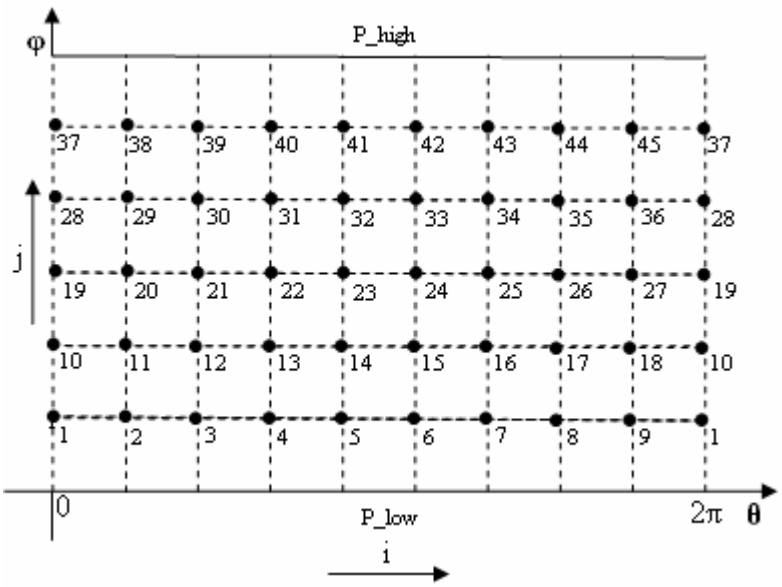

Figure 3.4 Numbering scheme of the mesh grid

With the given ordering of the grid points, the finite difference equation (3.61) now becomes

$$\begin{aligned}
&\frac{3}{8b^2}H_i^2\left(H_{i+1}-H_{i-1}\right)\cdot\left(\left(P_n\right)_{l+1}^2-\left(P_n\right)_{l-1}^2\right)\\
&+\frac{1}{2b^2}H_i^3\left(\left(P_n\right)_{l+1}^2-2\left(P_n\right)_l^2+\left(P_n\right)_{l-1}^2\right)\\
&+\frac{1}{2a^2}H_i^3\left(\left(P_n\right)_{l+n}^2-2\left(P_n\right)_l^2+\left(P_n\right)_{l-n}^2\right)\\
&-\frac{6\lambda}{2b}\left[\left(P_n\right)_l\left(H_{i+1}-H_{i-1}\right)+H_i\left(\left(P_n\right)_{l+1}-\left(P_n\right)_{l-1}\right)\right]=0
\end{aligned} \tag{3.62}$$

There are exceptional cases for the numbering of periodic nodes which make coding a challenging problem. Solutions to the finite difference equation (3.62) are obtained by applying Gauss-Seidel iteration. Details of the coding scheme are available in appendix.

3.2.2 Finite Element Analysis (FEA)

Results from finite difference solution are validated by a separate finite element analysis. Finite element method was applied to the problem using a commercial code, COMSOL Multiphysics. A sub-module called “film damping” is utilized to solve

compressible gas flow within a very narrow gap. Considering the large aspect ratio of channel geometry, a modified Reynolds equation which is very similar to the equation (3.46) is solved for the defined bearing geometry. Since the pressure variation across the film thickness, h, is neglected, 2D solution for the pressure variation on the bearing/journal surface is sufficient to obtain the pressure variation for the entire channel.

The channel flow can be modeled either on the boundary of the journal, or on the bearing surface itself. If journal is selected, then the region of the journal spanned by the bearing should be identified, and boundary conditions on the edges of this journal should be defined. Figure 3.5 shows boundary conditions, and a typical journal geometry on which the bearing is settled. Since the effect of gas film thickness on the radius of bearing is ignored, we expect the pressure variable on the bearing and journal surfaces to have the same magnitude applied in opposite directions.

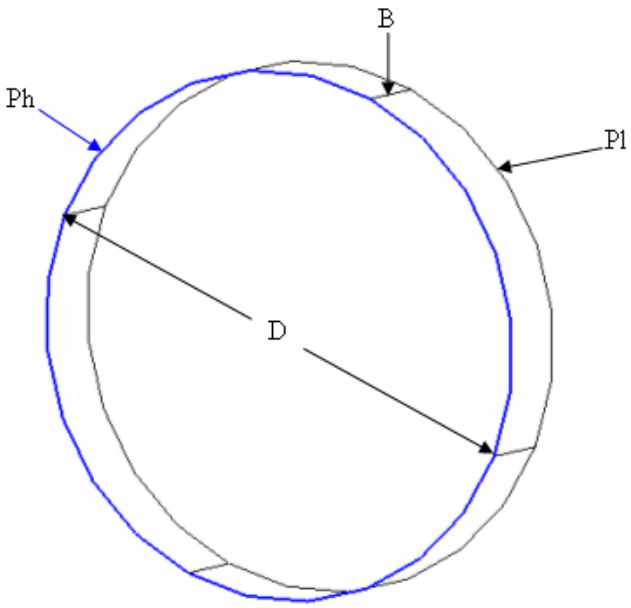

Figure 3.5 Representation of bearing ring in COMSOL Multiphysics

Entire procedure to solve the modified Reynolds equation using COMSOL can be summarized by the following flowchart,

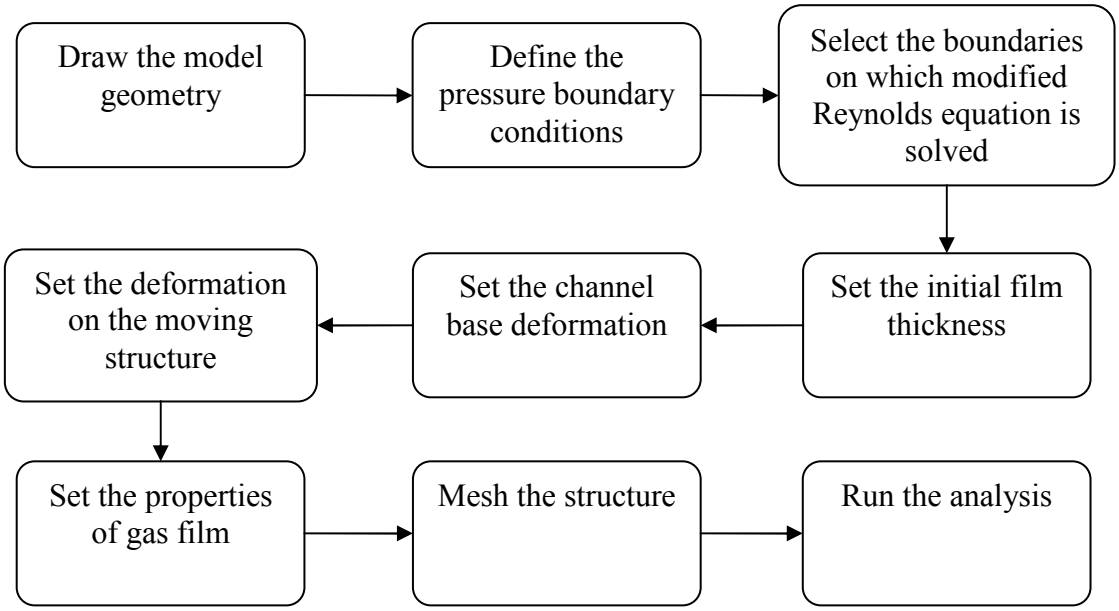

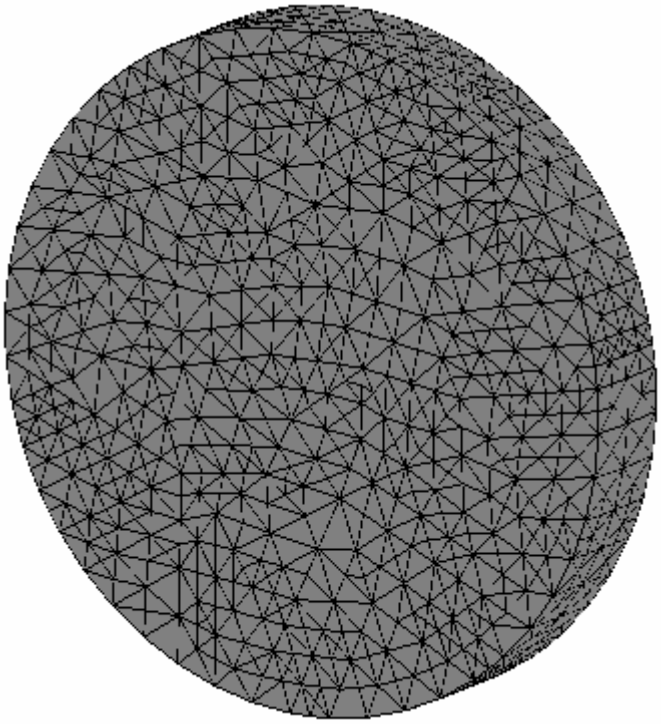

Figure 3.6 Meshed view of journal (shaft)

4 PRESSURE DISTRIBUTION RESULTS FOR BEARING CASE AND COMPARISON WITH OTHER WORK IN LITERATURE

In the previous section, finite difference approximation and finite element methods are introduced to solve the governing Reynolds equation for the gas film flow. The aim of these two methods is to get the pressure distribution on the bearing surface. Integrating the distributed pressure values, lifting force, F_n, acting on the bearing can be calculated. Under steady conditions, lifting force, F_n, is equal to the load, W, that is carried by the bearing. Ratio of z component of the load, W_z, to the x component, W_x, is employed to estimate the attitude angle. Similarly, using the pressure data, friction force acting on the bearing surface and frictional torque can be estimated. All of these concepts can be illustrated in non-dimensional form in design charts corresponding to certain B/D ratios, eccentricity ratio, ε, and compressibility ratio, λ.

In this section, starting from pressure distributions, calculated values of these parameters are illustrated for two bearing ratios, B/D = ½ and 1. For comparison purposes, two specific cases of pressure distribution obtained from finite difference and finite element methods are presented. Then, the results of both methods are compared; and it is confirmed that both methods converge to the same result.

After comparison and matching of finite difference and finite element analysis results, obtained data is compared with previous literature work for validation. Literature work consists of pressure solutions to the bearing cases which are subjected to the same ambient pressures at the inlet and exit of the bearing. In order to make a comparison with the published work, load capacity, attitude angle and friction force are evaluated for bearing cases which are subjected to same ambient pressures at inlet and exit. In this section, important design parameters for a bearing design such as load capacity, attitude angle and friction force are evaluated for bearing cases which have the same ambient pressures at both sides.

4.1 Effect of Compressibility

The solution of governing equation for compressible case differs from the solution of incompressible case such that the results are function of an additional dimensionless design parameter called the compressibility number λ,

$$\theta = \frac{x}{r}, \varphi = \frac{y}{r}, P_n = \frac{P}{P_a}, H = \frac{h}{c} \text{ and } \lambda = \left(\frac{r}{c}\right)^2 \frac{\mu\omega}{P_a} \tag{4.1}$$

and P_a being the ambient pressure. It is a common procedure in literature to express the compressibility number as 6 times λ. However, in this thesis, for comparison with Raimondi's work [36], λ is used as the compressibility number. Raimondi states that compressibility number can be regarded as the index which reflects the elasticity of the lubricant, $\lambda = 0$ corresponding to an incompressible fluid, and $\lambda = \infty$ corresponding to an extremely elastic (compressible) fluid. Thus, for very low velocities ω, gas flow can be governed by the incompressible flow theory. On the other hand, when the compressibility number becomes very large with increasing speed or reducing ambient pressure, compressibility effects become very significant. In Figure 4.1, Raimondi demonstrates the difference between the load carrying capacity of liquids and gases in relation to bearing number. Similarly, Figure 4.2 illustrates an experimental demonstration which shows the relationship between load carrying capacity W and λ for an aerodynamic gas-lubricated journal bearing. In this experiment, speed, viscosity and eccentricity ratio are held constant while the ambient pressure is reduced gradually. Reducing ambient pressure increases compressibility number. It is noticed that when the ambient pressure is reduced to 9%, the load carrying capacity is lowered by 40%. However, as noticed from the Figure 4.1, load carrying capacity of incompressible fluid is independent of ambient pressure.

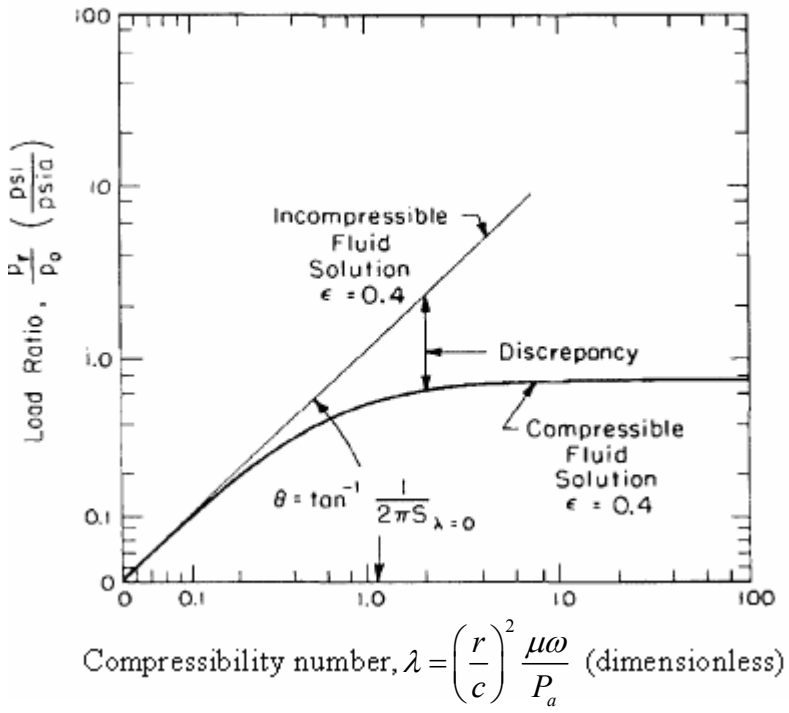

Figure 4.1 Discrepancy in load capacity between incompressible and compressible fluid theories [36]

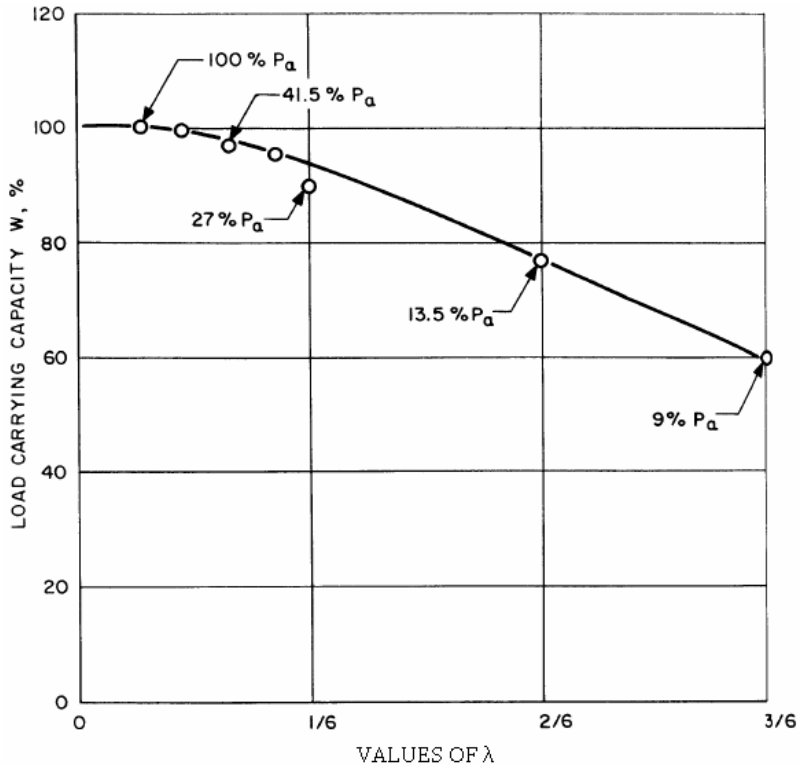

Figure 4.2 Relationship between load-carrying capacity and compressibility ratio. Speed, viscosity and eccentricity ratio held constant. Ambient pressure varied [47].

4.2 Pressure Distributions Obtained from Finite Difference Method

For $B/D=1$ and $\varepsilon=0.4$, Figure 4.3 and 4.4 presents the effect of compressibility number on the pressure distribution obtained from finite difference method, in dimensionless θ and φ directions respectively. Figure 4.3 shows the pressure distribution along θ direction at cross section $\varphi=B/(2r)$. Similarly, Figure 4.4 illustrates the effect of compressibility on pressure distribution along φ direction at cross section $\theta=\pi$. Note that all data in these figures are dimensionless. In other words, any journal bearing which has the bearing ratio $B/D=1$ and eccentricity $\varepsilon=0.4$ would give the same result for pressure distributions regardless of the actual length and diameter. It is noticed from the figures that increasing λ affects pressure distribution radically. Figure 4.3 shows that as the compressibility number gets larger, pressure distribution becomes symmetrical with respect to $\theta=\pi$. On the other hand, Figure 4.4 illustrates that pressure distributions are symmetrical with respect to $\varphi=B/(2r)$ irrespective of compressibility number. Moreover, it is noted from Figure 4.4 that a saddle point forms along the φ direction when the compressibility number gets very large. This is a valuable indication for the fact that the load carrying capacity of journal gas bearings, which operate with the same ambient conditions at both ends, converges to a steady state value as the compressibility number goes to infinity.

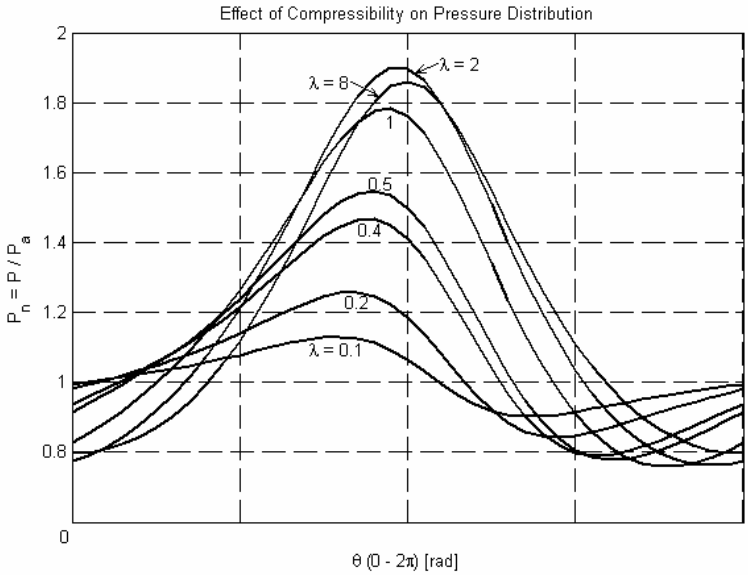

Figure 4.3 Compressibility effect on pressure distribution along θ direction; B/D=1, ε=0.4

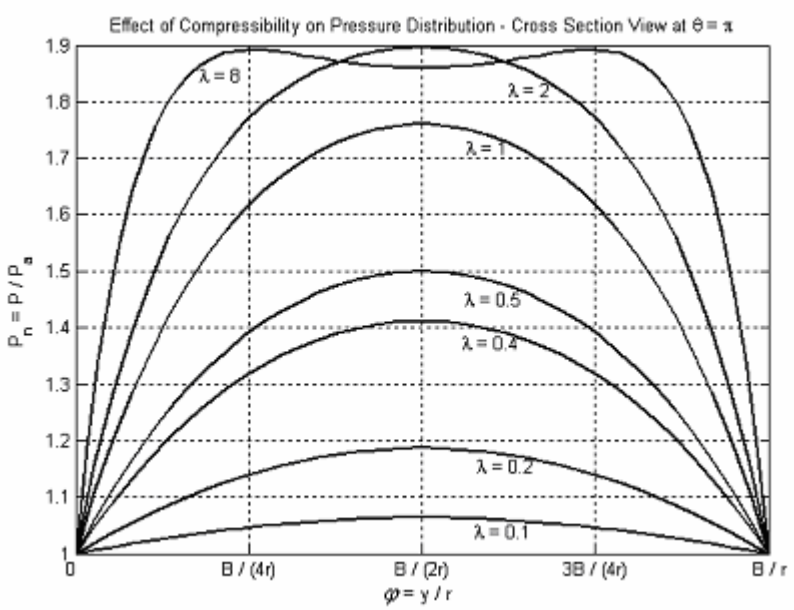

Figure 4.4 Compressibility effect on pressure distribution along φ direction; B/D=1, ε=0.4

Figure 4.5 below shows the solution to the 3D pressure distributions of a gas-lubricated journal bearing obtained from finite difference scheme. The figure presents a specific case where $B/D=1$, $\varepsilon=0.2$, and $\lambda=2$. For the same design parameters, pressure distributions along θ and φ directions are presented consecutively in Figures 4.6 and 4.7.

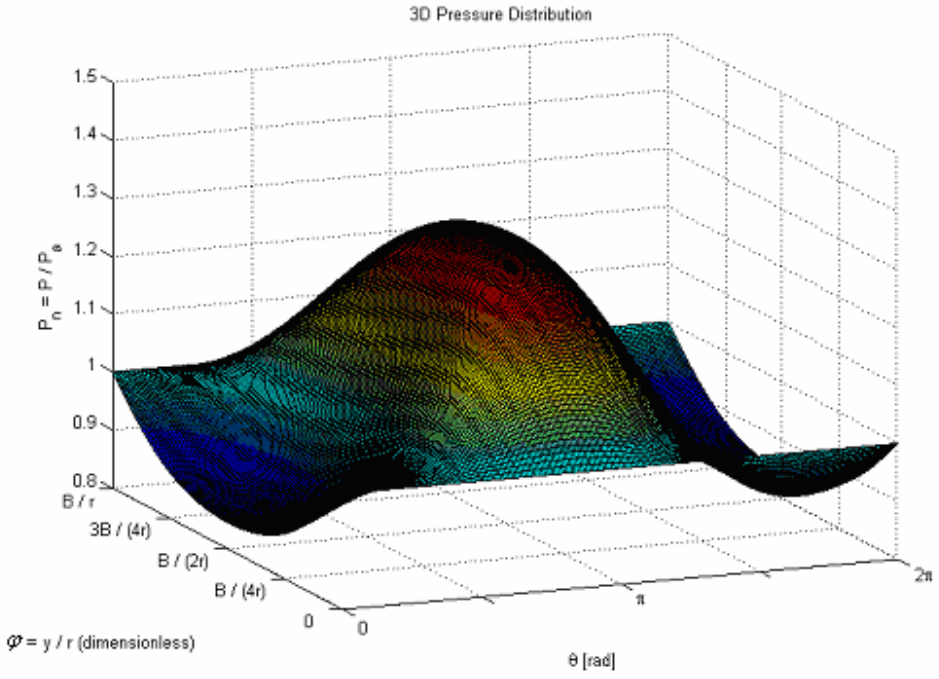

Figure 4.5 3D pressure distribution on bearing surface; B/D=1, ε=0.2, λ=2 - (FD)

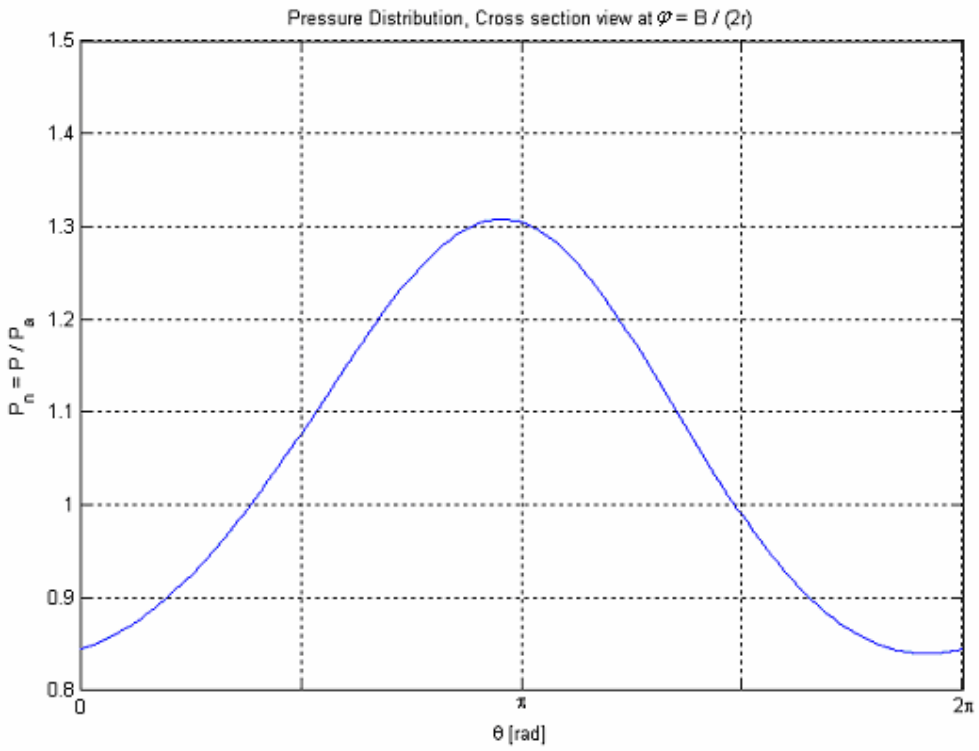

Figure 4.6 Pressure distribution along θ direction; B/D=1, ε=0.2, λ=2 - (FD)

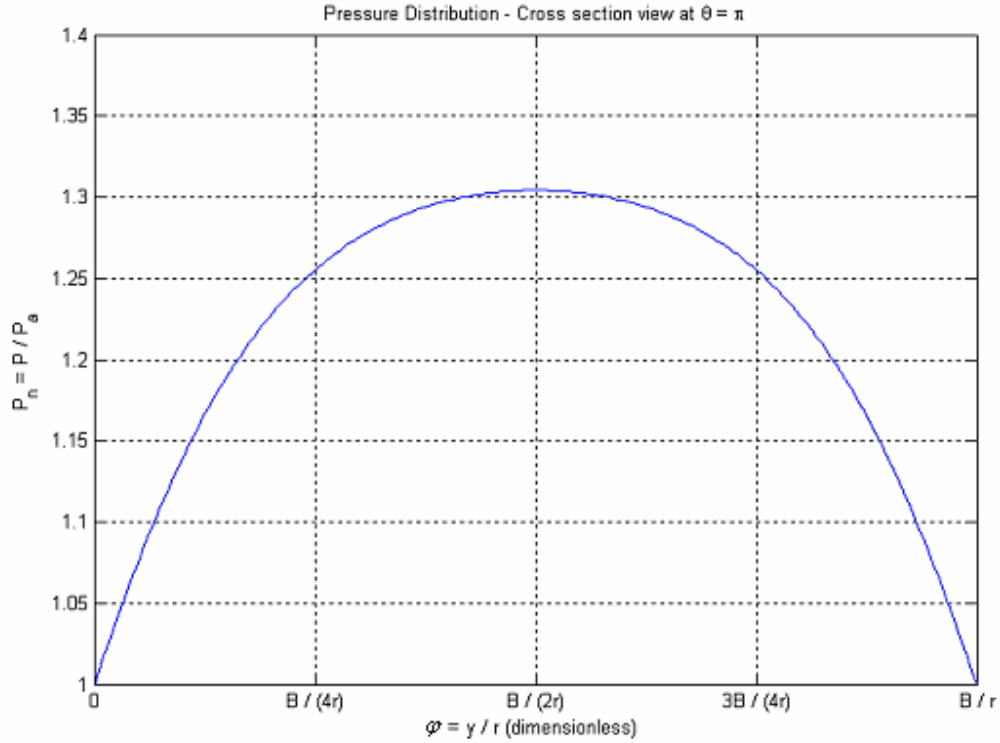

Figure 4.7 Pressure distribution along φ direction; B/D=1, ε=0.2, λ=2 - (FD)

Similarly, Figure 4.8 is a representation of 3D pressure distribution for the bearing design parameters B/D = ½, ε = 0.2 and $\lambda = 2$. Figure 4.9 and Figure 4.10 demonstrate 2D views of the same pressure distribution in θ and φ directions respectively. Note that pressure distribution curve in Figure 4.10 is more concave with respect to that in Figure 4.7. The reason behind is that the B/D ratio in figure 4.7 is 2 times the B/D ratio in Figure 4.10 so that the bearing is more close to infinitely long bearing assumption. If B/D ratio goes to infinity (long bearing assumption), pressure distribution along φ attains a flat structure which means that the pressure distribution on the bearing surface is characterized totally by the pressure distribution along the θ direction.

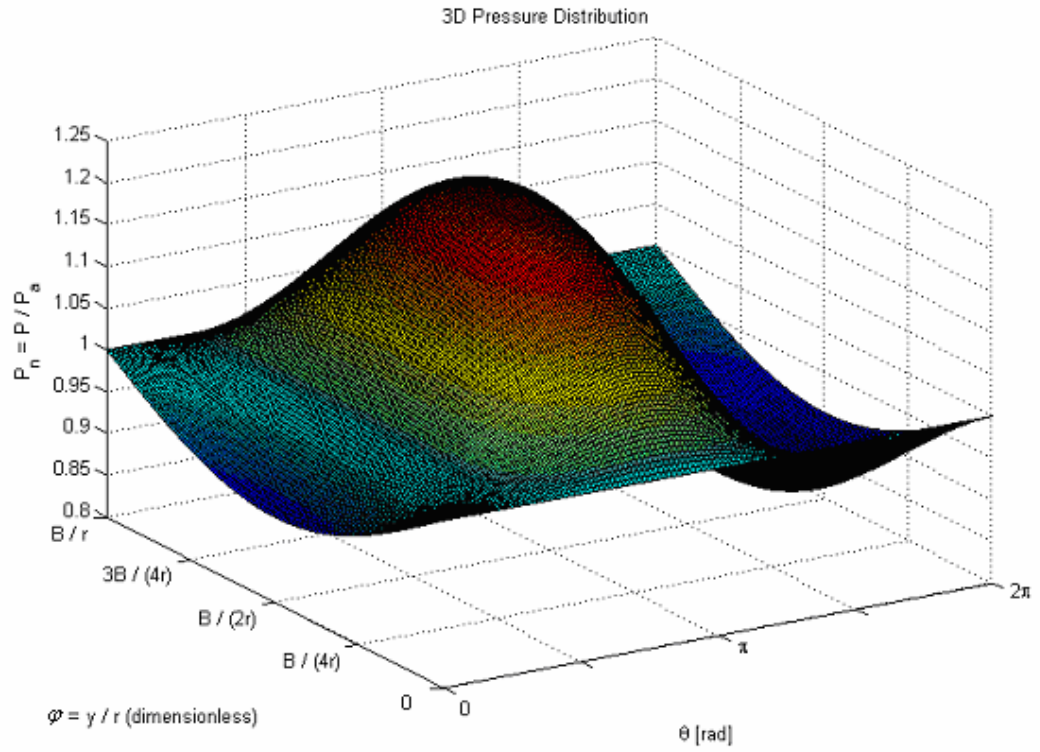

Figure 4.8 3D pressure distribution on bearing surface; B/D=1/2, ε=0.2, λ=2 - (FD)

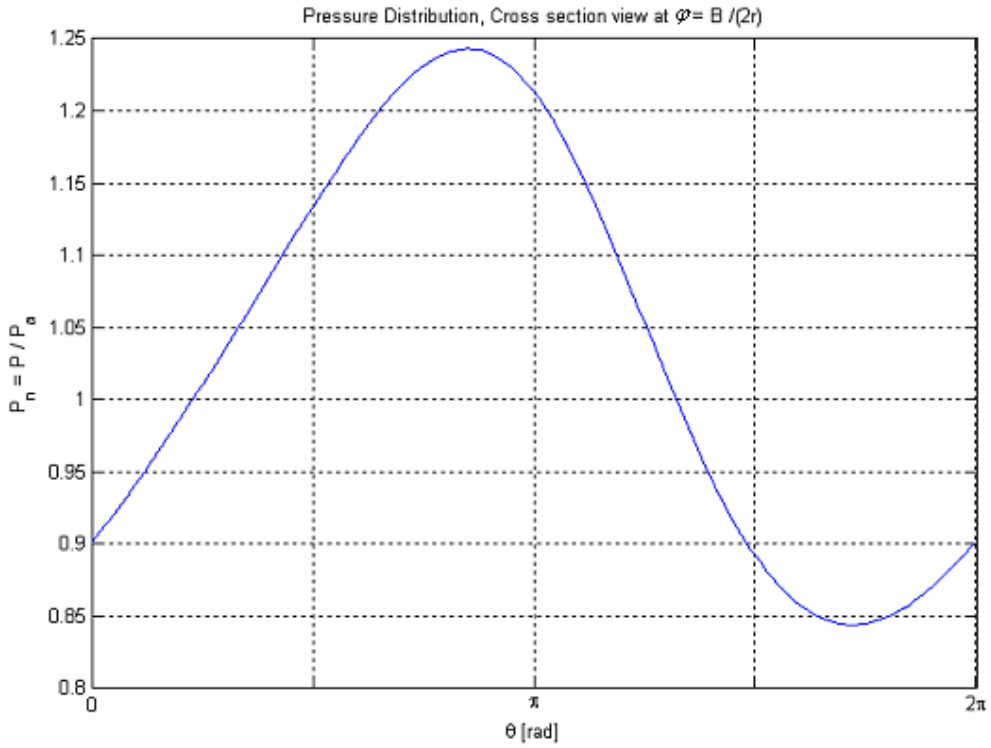

Figure 4.9 Pressure distribution along θ direction; B/D=1/2, ε=0.2, λ=2 - (FD)

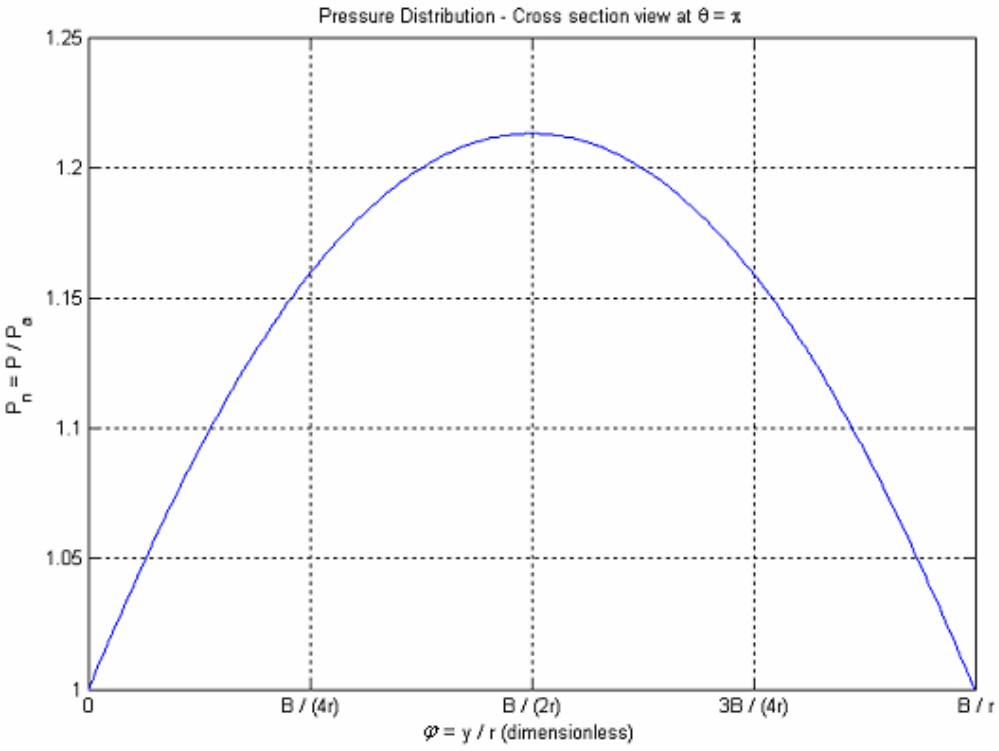

Figure 4.10 Pressure distribution along φ direction; B/D=1/2, ε=0.2, λ=2 - (FD)

4.3 Pressure Distributions Obtained from Finite Element Method

In the previous section, results of finite difference approach were illustrated for some specific bearing designs. In this part, finite element solutions to the governing equation (3.46) obtained from the analysis code COMSOL are illustrated. For comparison purposes, finite element analyses are conducted with the same bearing design parameters.

Figure 4.11 presents the 3D pressure distribution on the journal for which $B/D=1, \varepsilon=0.2$ and $\lambda=2$. Color bar on the right side shows the values of dimensionless pressure, i.e. $P_n = P/P_a$. Using the same design parameters as in the previous section, pressure distributions along θ and φ directions are presented consecutively in the Figures 4.12 and 4.13. The results indicate that the pressure distributions obtained from finite element method are almost the same as the ones obtained from finite difference approach. Relative error in between is around 0.1 %. The same scenario is valid for Figures 4.14, 4.15 and 4.16. These figures present the pressure distributions obtained from finite element method for the bearing design parameters B/D = ½, ε = 0.2 and $\lambda=2$. As in the finite difference case, Figure 4.14 presents the pressure distributions in 3D while the others are 2D representations of pressure distribution in θ and φ directions respectively. Again, the results are in good agreement with the ones obtained from finite difference method.

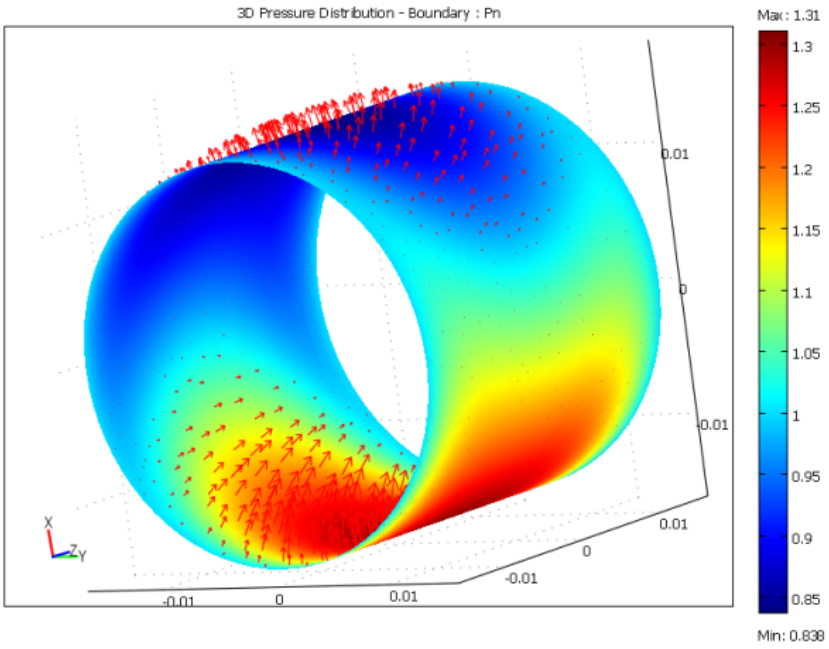

Figure 4.11 3D pressure distribution on bearing surface; B/D=1, ε=0.2, λ=2 - (FEA)

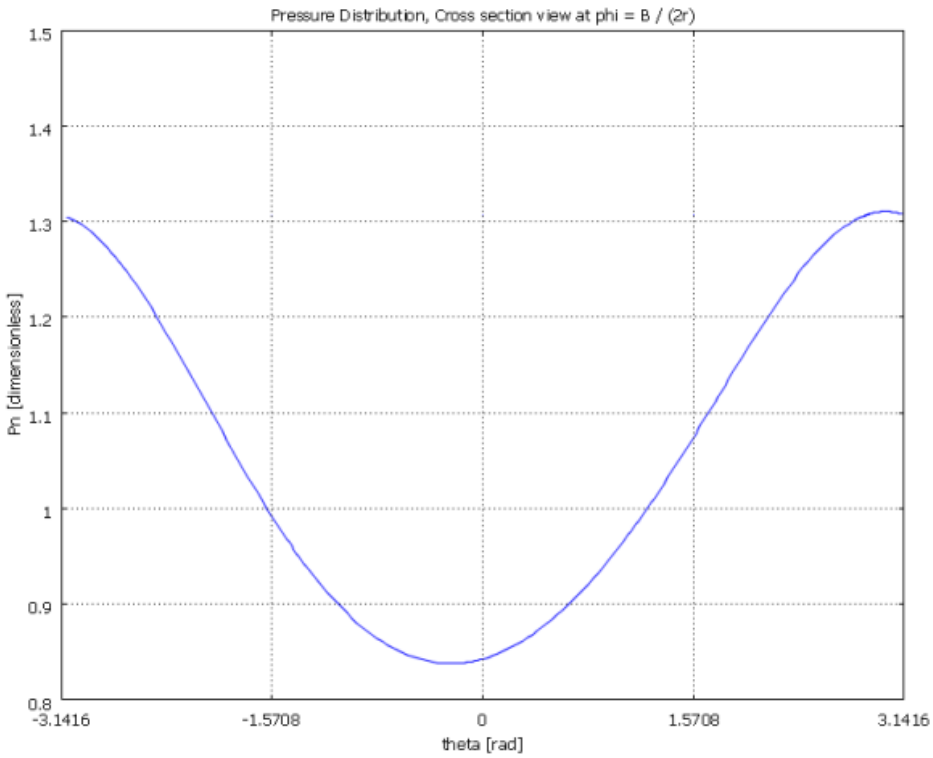

Figure 4.12 Pressure distribution along θ direction; B/D=1, ε=0.2, λ=2 - (FEA)

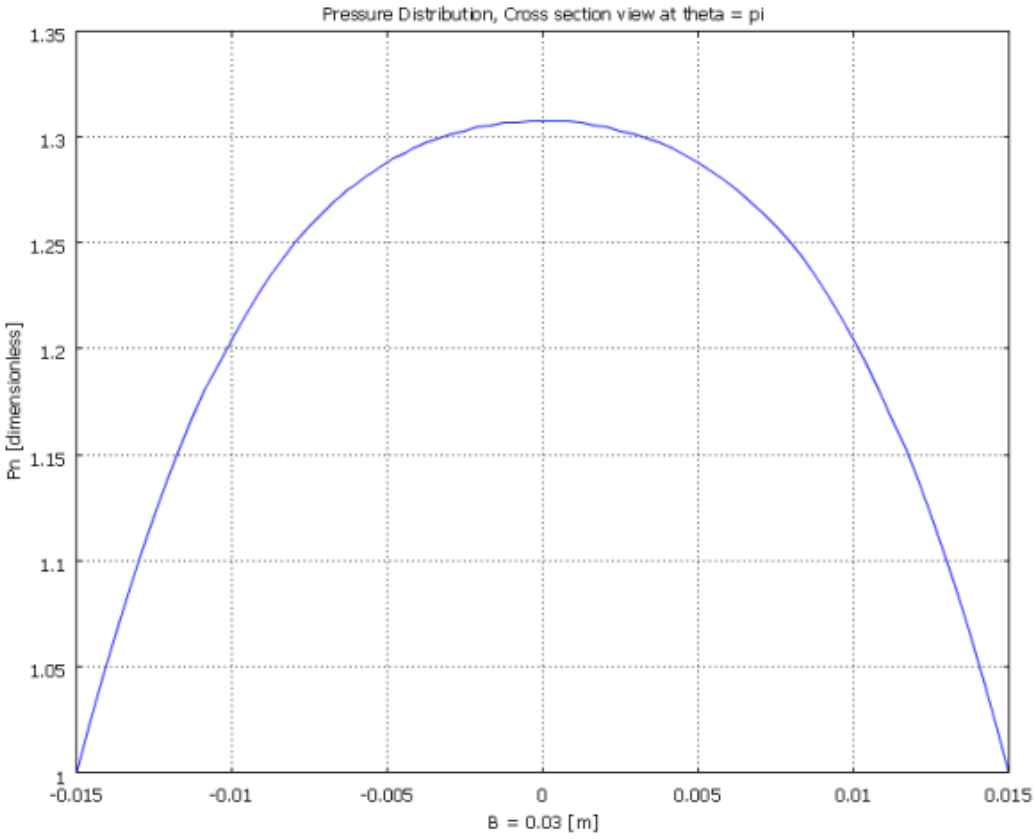

Figure 4.13 Pressure distribution along φ direction; B/D=1, ε=0.2, λ=2 - (FEA)

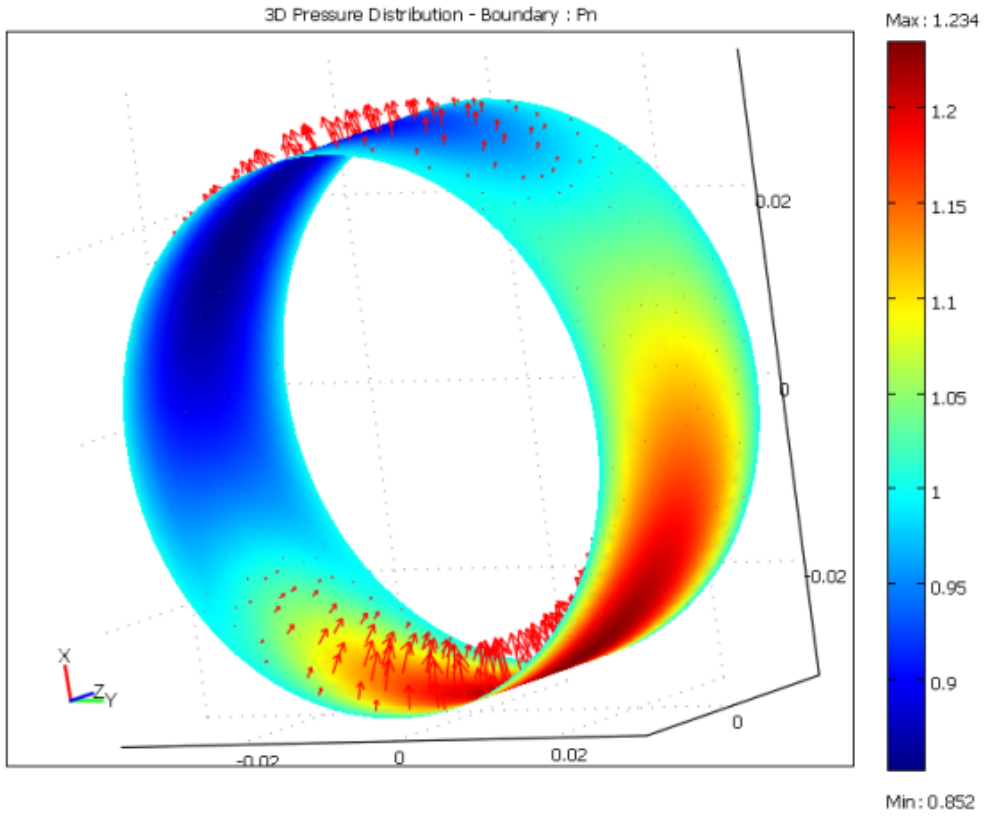

Figure 4.14 3D pressure distribution on bearing surface; B/D=1/2, ε=0.2, λ=2 - (FEA)

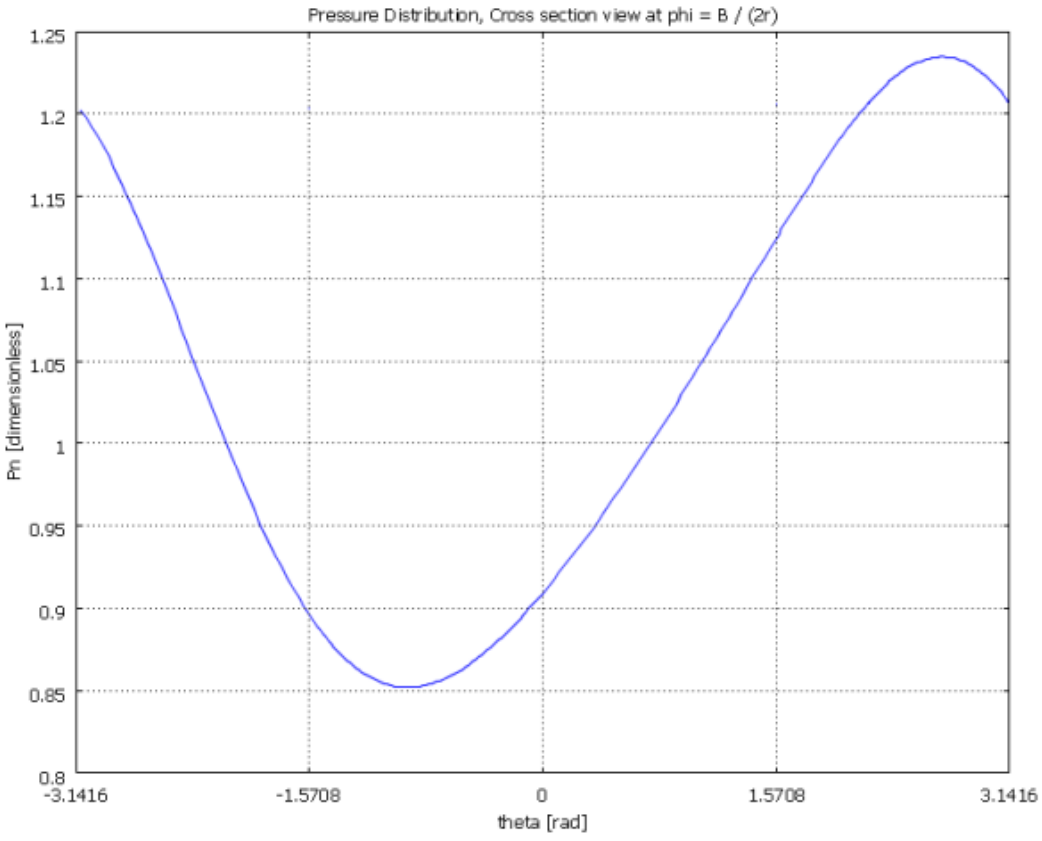

Figure 4.15 Pressure distribution along θ direction; B/D=1/2, ε=0.2, λ=2 - (FEA)

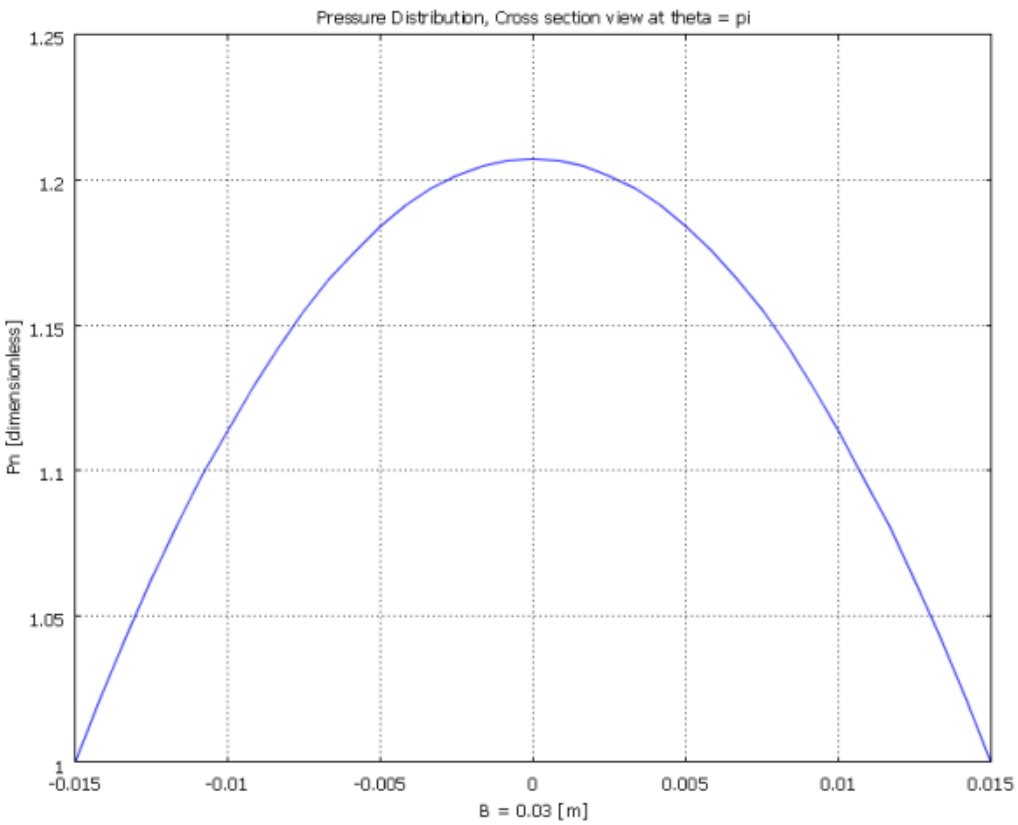

Figure 4.16 Pressure distribution along φ direction; B/D=1/2, ε=0.2, λ=2 - (FEA)

Although the figures show that the results of both methods are in good agreement, in order to make a numerical comparison, results are tabulated in Table 4.1 and Table 4.2 respectively for finite difference and finite element method. The data obtained from finite difference method consists of load ratio P_r / P_a, attitude angle ϕ, Sommerfeld number S, maximum pressure ratio $P_{\max} / P_a$, minimum pressure ratio $P_{\min} / P_a$, relative error for the convergence, # of iterations until convergence and node numbers, m and n, in the mesh grid. On the other hand, for the finite element approach, in addition to $P_r / P_a, \phi$ and S, friction force variable F_t / F_c and time to convergence are also evaluated. These are commonly presented parameters in literature work. In order to make a comprehensive comparison with literature work, all these parameters are tabulated in this study. Theoretical relations for these parameters are as follows:

$$P_r = W/(2rB) \tag{4.2}$$

$$S = \left(\frac{r}{c}\right)^2 \mu \left(\frac{\omega}{2\pi P_r}\right) \tag{4.3}$$

$$F_c = 2\pi\mu UrB/c \rightarrow \text{friction force for concentric } (\varepsilon=0) \text{ case} \tag{4.4}$$

See the list of symbols for the definitions of remaining parameters.

Data in Table 4.1 and Table 4.2 are also used to create design charts for gas lubricated journal bearings (Figure 4.17 through Figure 4.19). In the following section, by using these design charts, solution to the governing equation is validated with Raimondi's results.

4.4 Numerical Validation with Other Published Work

Figure 4.17 through Figure 4.19 are the design charts that illustrate the change of load ratio, attitude angle and friction force variable with respect to compressibility ratio when B/D = ½. Again, all of these design parameters are dimensionless. Load ratio is the ratio of load per unit projected area, $P_r = W/(2rB)$, to the ambient pressure, P_a. Friction force variable is the ratio of the actual friction force F_t to the friction force F_c that is calculated by assuming that the journal is concentric within the bearing. Attitude angle ϕ represents the angle between the minimum film thickness location and the resultant load axis, shown in Figure 1.2. For bearing ratios $B/D =$ ½, and eccentricities ranging from 0.1 to 0.8, these design parameters are plotted with respect to λ in the Figures (4.17 - 4.19). See Appendix B for the same parameters solved and validated with published work for B/D = 1. Appendix B also contains tabulated data of finite difference and finite element solutions to the governing Reynolds equation for comparison purposes in between.

For high compressibility numbers, it is noticed that the load ratio converges to a constant value. This implies that, for the same ambient condition, a substantial increase in the rotor speed would not increase the load capacity after a certain value. Also, design chart for attitude angle (Figure 4.18) demonstrate that the attitude angle starts with 90^o at low compressibility numbers, and reduces gradually to 0 degrees when the speed of the journal increases. It is also realized from Figure 4.19 that the friction force variable is higher for low compressibility numbers. However, this does not mean that the actual friction force is also high. Depending on the friction force at concentric case F_c actual friction force can still be small.

Design charts are also utilized to validate the results with the previous work in literature. Data obtained from finite element and finite difference methods, both of which point to the same values, are compared with the results of Raimondi [36] for the same bearing design parameters. Tabulated data of his finite difference solution is plugged into these design charts. Small circles on the figures represent the data retrieved from Raimondi's work. It is seen that our results are in good agreement with Raimondi's work validating that the presented finite difference and finite element codes are functioning properly. Relative difference in between is on the order of 0.01 demonstrating that results are fitting well to each other. Therefore, developed analyses can be used to solve the gas-lubrication problems for any bearing ratios, eccentricity ratios and compressibility numbers. In other words, these solution procedures will be applied to the proposed seal design to obtain the design parameters such as load ratio, attitude angle and friction force. The next chapter includes the results of these design parameters for the new seal design. Leakage flow analysis and frequency analysis are also carried out in the next chapter.

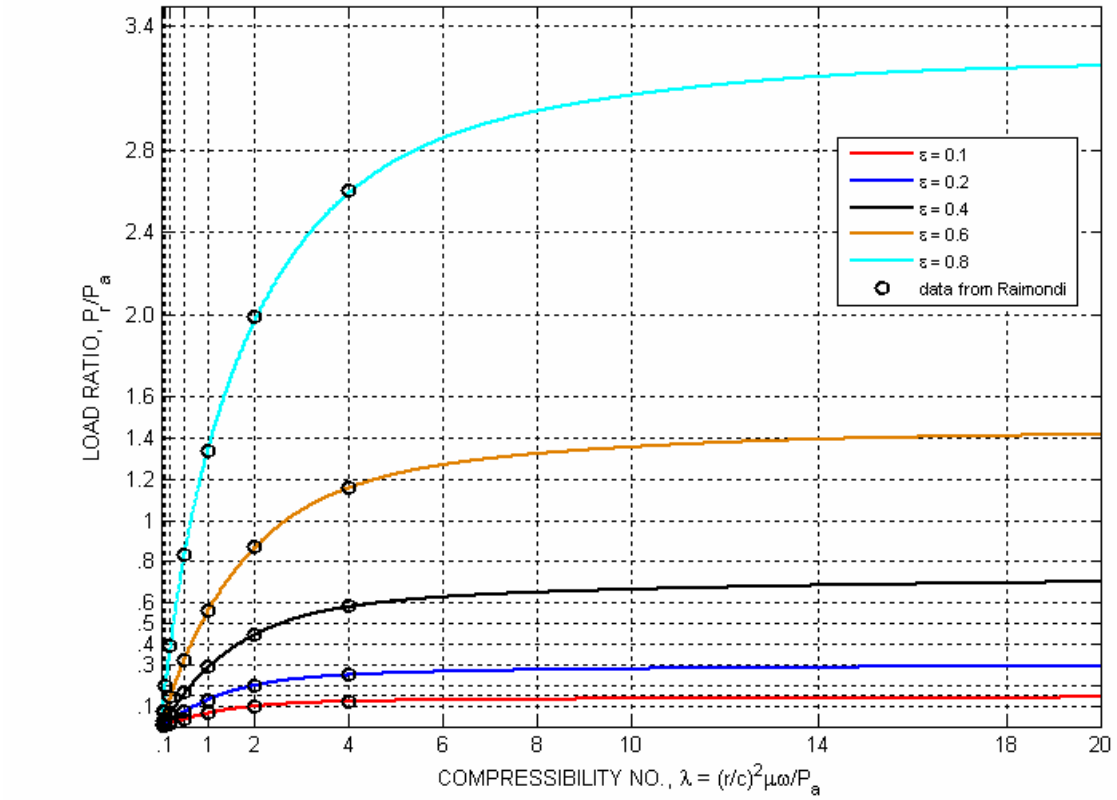

Figure 4.17 Load ratio vs. compressibility no; B/D=1/2

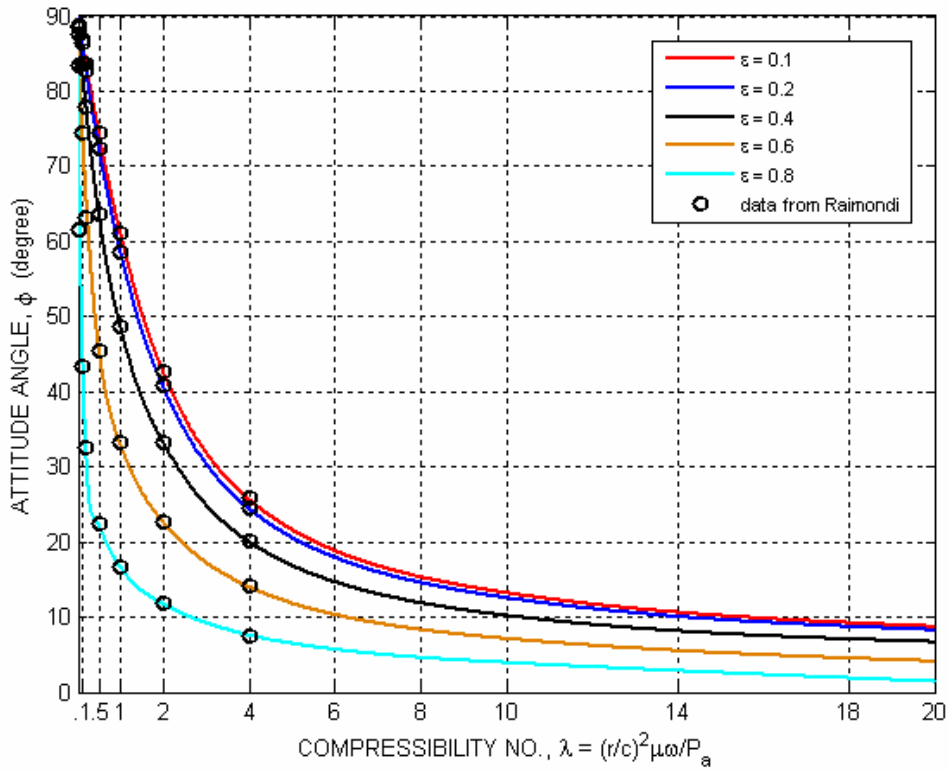

Figure 4.18 Attitude angle vs. compressibility no; B/D=1/2

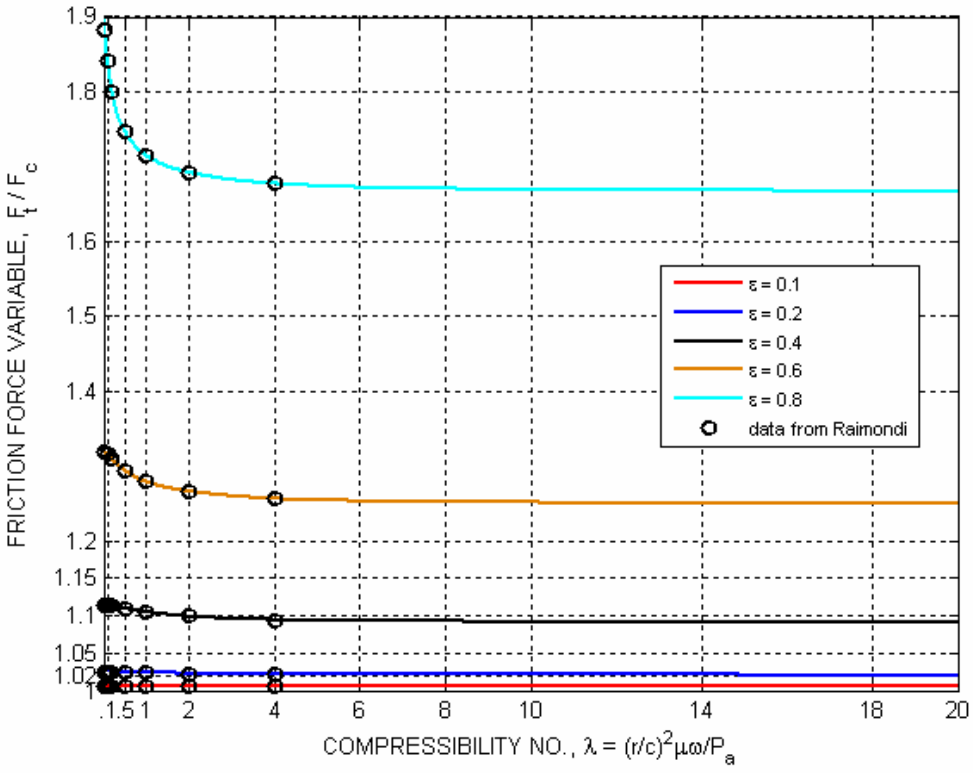

Figure 4.19 Friction force variable vs. compressibility no; B/D=1/2

B/D = 1/2 - ε = 0.1													
	Compressibility Number, λ												
	0.1	0.2	0.4	0.5	0.6	0.8	1.0	2.0	4.0	6.0	8.0	10	20
P_r / P_a	0,007177	0,014292	0,028055	0,034597	0,040858	0,05244	0,062698	0,096501	0,119885	0,127209	0,130858	0,133284	0,140129
Φ	86,76184	83,53218	77,2418	74,22168	71,30452	65,81362	60,81023	42,46542	25,66749	18,82909	15,31778	13,19654	8,705419
S	2,217437	2,227187	2,269155	2,300138	2,337208	2,428002	2,538435	3,298521	5,310248	7,5068	9,729943	11,94103	22,71554
P_{max} / P_a	1,007011	1,014019	1,027843	1,034484	1,040864	1,053122	1,063971	1,101903	1,128071	1,133495	1,133444	1,131919	1,126305
P_{min} / P_a	0,993072	0,986293	0,973463	0,967602	0,962	0,952166	0,943605	0,918685	0,905126	0,903287	0,903793	0,905654	0,910185
relative err	5E-08	4,99E-08	4,99E-08	4,96E-08	4,99E-08	4,97E-08	4,98E-08	5E-08	4,97E-08	4,98E-08	4,99E-08	4,98E-08	4,99E-08
# of iterations	911	1006	1098	1123	1138	1156	1194	1254	1314	1340	1360	1392	3982
m	36	36	36	36	36	36	36	36	36	36	36	36	60
n	40	40	40	40	40	40	40	40	40	40	40	40	40

B/D = 1/2 - ε = 0.2													
	Compressibility Number, λ												
	0.1	0.2	0.4	0.5	0.6	0.8	1.0	2.0	4.0	6.0	8.0	10	20
P_r / P_a	0,014904	0,029629	0,057895	0,071216	0,083908	0,107296	0,128009	0,197667	0,248652	0,265099	0,27321	0,278498	0,293074
Φ	86,26133	82,56981	75,54037	72,25861	69,14787	63,43885	58,37684	40,50611	24,45678	17,91826	14,55562	12,52559	8,245399
S	1,067873	1,074335	1,09961	1,117406	1,138067	1,186663	1,24331	1,610333	2,560288	3,602169	4,660298	5,714758	10,86106
P_{max} / P_a	1,015542	1,031267	1,062259	1,077303	1,09202	1,119325	1,144554	1,234062	1,299662	1,316002	1,316864	1,314745	1,302262
P_{min} / P_a	0,984897	0,970313	0,944046	0,932622	0,922096	0,904455	0,890304	0,852723	0,83543	0,833964	0,835775	0,839168	0,847617
relative err	4,98E-08	5E-08	4,98E-08	4,97E-08	4,98E-08	4,98E-08	4,97E-08	4,97E-08	4,97E-08	4,96E-08	4,96E-08	4,97E-08	4,99E-08
# of iterations	1011	1112	1198	1212	1216	1231	1278	1326	1379	1408	1422	1444	4017
m	36	36	36	36	36	36	36	36	36	36	36	36	60
n	40	40	40	40	40	40	40	40	40	40	40	40	40

B/D = 1/2 - ε = 0.4													
	Compressibility Number, λ												
	0.1	0.2	0.4	0.5	0.6	0.8	1.0	2.0	4.0	6.0	8.0	10	20
P_r / P_a	0,034948	0,068996	0,132463	0,16165	0,189196	0,239704	0,284663	0,444421	0,579424	0,626905	0,649883	0,664155	0,701518
Φ	83,51924	77,46363	67,3268	63,19006	59,55554	53,46396	48,5371	33,10479	20,0443	14,65798	11,86007	10,16741	6,654686
S	0,455401	0,461345	0,480602	0,492281	0,50473	0,531171	0,559099	0,716235	1,098712	1,523246	1,959182	2,396351	4,537443
P_{max} / P_a	1,046151	1,094172	1,185842	1,229662	1,270814	1,345516	1,414035	1,656562	1,860094	1,912654	1,927591	1,926344	1,893283
P_{min} / P_a	0,957383	0,920713	0,865599	0,845466	0,829403	0,805859	0,790539	0,759169	0,752067	0,754386	0,759125	0,763788	0,77826
relative err	4,97E-08	5E-08	4,97E-08	4,97E-08	4,97E-08	5E-08	4,99E-08	4,95E-08	4,99E-08	4,98E-08	4,99E-08	4,96E-08	5E-08
# of iterations	1130	1228	1266	1258	1245	1259	1321	1323	1401	1419	1425	1430	13297
m	36	36	36	36	36	36	36	36	36	36	36	36	120
n	40	40	40	40	40	40	40	40	40	40	40	40	80

B/D = 1/2 - ε = 0.6													
	Compressibility Number, λ												
	0.1	0.2	0.4	0.5	0.6	0.8	1.0	2.0	4.0	6.0	8.0	10	20
P_r / P_a	0,072005	0,141088	0,266832	0,32362	0,376766	0,473414	0,559006	0,868642	1,157407	1,268887	1,323038	1,35548	1,437169
Φ	74,14491	62,78178	49,50968	45,29821	41,95494	36,89557	33,16439	22,62528	13,9975	10,28256	8,299842	7,08604	4,601044
S	0,221035	0,22561	0,238584	0,245898	0,253455	0,268948	0,284711	0,366446	0,55004	0,752573	0,962361	1,174159	2,214839
P_{max} / P_a	1,141786	1,283147	1,526996	1,629784	1,729369	1,905224	2,056182	2,576946	3,036211	3,190905	3,238801	3,246815	3,179181
P_{min} / P_a	0,891053	0,825263	0,764806	0,745914	0,736388	0,723231	0,716265	0,7085	0,717692	0,726306	0,731861	0,737067	0,755168
relative err	4,98E-08	4,98E-08	5E-08	4,96E-08	4,97E-08	4,98E-08	4,97E-08	4,97E-08	4,99E-08	4,98E-08	5E-08	4,98E-08	5E-08
# of iterations	1202	1262	1271	1254	1232	1201	1297	1304	1373	1374	1387	1396	89219
m	36	36	36	36	36	36	36	36	36	36	36	36	350
n	40	40	40	40	40	40	40	40	40	40	40	40	140

B/D = 1/2 - ε = 0.8													
	Compressibility Number, λ												
	0.1	0.2	0.4	0.5	0.6	0.8	1.0	2.0	4.0	6.0	8.0	10	20
P_r / P_a	0,201728	0,391898	0,701659	0,831481	0,94923	1,156675	1,335445	1,968995	2,590147	2,856584	2,98766	3,065202	3,269485
Φ	42,91814	32,26677	24,33491	22,21103	20,5945	18,22505	16,51329	11,70447	7,567085	5,645371	4,565328	3,888201	2,479358
S	0,078896	0,081223	0,090731	0,095706	0,1006	0,110078	0,119178	0,161661	0,245785	0,334291	0,426166	0,519232	0,973578
P_{max} / P_a	1,656169	2,143499	2,837438	3,11807	3,375588	3,819322	4,193978	5,482489	6,681551	7,12587	7,288619	7,339299	7,193438
P_{min} / P_a	0,74954	0,707678	0,687965	0,690672	0,683738	0,684503	0,688923	0,697629	0,715671	0,724873	0,731341	0,7376	0,755788
relative err	4,96E-08	4,97E-08	4,95E-08	4,96E-08	4,99E-08	4,98E-08	4,99E-08	4,96E-08	4,97E-08	4,99E-08	4,99E-08	4,98E-08	5E-08
# of iterations	1192	1245	1257	1242	1218	1171	1200	1212	1269	3331	3459	3460	160023
m	36	36	36	36	36	36	36	36	36	60	60	60	500
n	40	40	40	40	40	40	40	40	40	40	40	40	150

Table 4.1 Analysis results of finite difference method when B/D = ½

B/D = 1/2 - ε = 0.1													
	Compressibility Number, λ												
	0.1	0.2	0.4	0.5	0.6	0.8	1.0	2.0	4.0	6.0	8.0	10	20
P_r / P_a	0,007217	0,014362	0,02818	0,0347	0,041	0,05265	0,062942	0,096779	0,120127	0,127439	0,13109	0,133524	0,140267
Φ	86,73	83,49	77,19	74,16	71,24	65,75	60,74	42,38	25,62	18,8	15,31	13,21	8,7
F_t / F_c	1,005038	1,005038	1,005038	1,005038	1,005038	1,005038	1,005038	1,00538	1,00538	1,00538	1,00538	1,00538	1,00538
S	1,006184	1,006173	1,006131	1,006102	1,006068	1,005993	1,005912	1,005557	1,005244	1,005147	1,005107	1,005086	1,005055
time (sec.)	29	31	140	128	156	144	162	212	211	253	293	315	423

B/D = 1/2 - ε = 0.2													
	Compressibility Number, λ												
	0.1	0.2	0.4	0.5	0.6	0.8	1.0	2.0	4.0	6.0	8.0	10	20
P_r / P_a	0,014976	0,029762	0,058137	0,071505	0,084238	0,1077	0,128475	0,198236	0,249177	0,265602	0,273717	0,279026	0,293383
Φ	86,23	82,53	75,49	72,2	69,09	63,37	58,31	40,44	24,41	17,9	14,55	12,54	8,25
F_t / F_c	1,025377	1,025317	1,025099	1,024955	1,024795	1,024452	1,0241	1,022667	1,02144	1,021054	1,020894	1,020813	1,020688
S	1,062	1,069	1,095	1,112	1,133	1,182	1,238	1,605	2,554	3,595	4,651	5,703	10,84
time (sec.)	158	188	217	186	207	185	212	215	323	417	396	465	527

B/D = 1/2 - ε = 0.4													
	Compressibility Number, λ												
	0.1	0.2	0.4	0.5	0.6	0.8	1.0	2.0	4.0	6.0	8.0	10	20
P_r / P_a	0,035075	0,069228	0,132856	0,162111	0,18972	0,240353	0,285435	0,44563	0,580868	0,628396	0,651428	0,665767	0,70177
Φ	83,48	77,42	67,28	63,15	59,52	53,43	48,51	33,09	20,03	14,66	11,87	10,19	6,64
F_t / F_c	1,113	1,113	1,111	1,11	1,109	1,107	1,105	1,099	1,094	1,092	1,092	1091	1,091
S	1,113275	1,112596	1,110594	1,109505	1,108438	1,106452	1,104703	1,098834	1,094257	1,092777	1,092156	1,091839	1,091348
time (sec.)	61	121	148	156	162	150	145	172	300	348	399	409	540

B/D = 1/2 - ε = 0.6													
	Compressibility Number, λ												
	0.1	0.2	0.4	0.5	0.6	0.8	1.0	2.0	4.0	6.0	8.0	10	20
P_r / P_a	0,07209	0,141191	0,266969	0,323808	0,37703	0,473893	0,55977	0,871039	1,161	1,274041	1,328585	1,36131	1,437115
Φ	74,1	62,76	49,54	45,35	42,01	36,96	33,23	22,685	14,063	10,316	8,333	7,121	4,586
F_t / F_c	1,316	1,31	1,298	1,294	1,29	1,284	1,279	1,266	1,256	1,253	1,252	1,251	1,25
S	0,22	0,225	0,238	0,245	0,253	0,268	0,284	0,365	0,547	0,749	0,958	1,169	2,214
time (sec.)	169	161	75	211	225	244	312	205	280	307	351	386	512

B/D = 1/2 - ε = 0.8													
	Compressibility Number, λ												
	0.1	0.2	0.4	0.5	0.6	0.8	1.0	2.0	4.0	6.0	8.0	10	20
P_r / P_a	0,200467	0,390025	0,700709	0,831459	0,950265	1,159986	1,341089	1,985193	2,619	2,886371	3,019543	3,098145	3,268
Φ	43,09	32,47	24,51	22,37	20,74	18,35	16,63	11,78	7,61	5,67	4,58	3,9	2,471
F_t / F_c	1,841	1,799	1,759	1,747	1,738	1,724	1,715	1,692	1,677	1,672	1,67	1,669	1,667
S	0,079	0,081	0,09	0,095	0,1	0,109	0,118	0,16	0,24	0,33	0,421	0,513	0,973
time (sec.)	208	194	221	230	221	244	222	258	328	312	412	453	530

Table 4.2 Analysis results of finite element method when B/D = ½

5 FORCE FREQUENCY AND LEAKAGE ANALYSIS

In the previous chapters, while introducing the lubrication theory, the term "bearing" was widespread throughout the text. The reason behind is that the lubrication theory is generally used for calculating load carrying capacity of bearings in literature. For gas lubricated journal bearings, it is not viable to carry heavy loads such as the ones in gas turbine applications. This work demonstrates that gas journal bearing structure can also be utilized as a high speed rotary sealing component once provisions for axial load supports and flexible radial attachments are properly developed. Taking into account that the load carrying capacities of gas films are substantially low, the proposed seal should have two important characteristics:

- it should be light and compliant in radial direction to avoid rotor hard-rubs
- it should be stiff in axial direction to bear sealing pressure loads

Geometric details of designed seal are explained in Chapter 2. Lubrication theory and the governing equations for the journal bearing and the designed seal are the same. The differences between the journal bearing and designed seal can be stated as follows,

- Journal bearings are rigid and have fixed supports. On the other hand, our seal have flexible supports and it can move radially around the journal.
- In a shaft-bearing assembly, aerodynamic force created between the journal and bearing surface is utilized for carrying the rotor assembly, whereas the lift force is functional for moving our seal radially around the journal.
- A bearing generally operates in an environment which has the same ambient pressure at both ends. However, seals are buffering components between different pressure levels. So, a seal has upstream and downstream pressures which affect the boundary conditions and solutions for the governing equations of lubrication theory.
- For a shaft-bearing assembly, the main concern is to carry the rotor with the externally exerted forces. On the other hand, for a shaft-seal assembly, the

main concern is to resist to the pressure load acting on the seal as well as to over come the seal ring weight and backing plate friction.

5.1 Application of Governing Reynolds Equation to the Designed Seal

In theory, the only difference between a bearing and a seal is the changing pressure boundary conditions across the seal assembly. Upstream, the seal is governed by high pressure, P_h, while the downstream side is occupied by low pressure, P_l. Note that in (3.47), we normalized the pressure variable with respect to ambient pressure P_a since the same ambient pressure conditions are valid around the journal bearing. For the flexible seal design (Figure 5.5), both sides are occupied by different pressures; therefore ambient pressure P_a is taken equal to downstream pressure (low pressure) P_l. Based on this assumption, equation (3.47) is reformulated for the flexible seal as

$$\frac{\partial}{\partial\theta}\left(P_n H^3 \frac{\partial P}{\partial\theta}\right)+\frac{\partial}{\partial\varphi}\left(P_n H^3 \frac{\partial P_n}{\partial\varphi}\right)=6\lambda\frac{\partial\left(P_n H\right)}{\partial\theta} \tag{5.1}$$

$$\theta=\frac{x}{r},\ \varphi=\frac{y}{r},\ P_n=\frac{P}{P_a},\ H=\frac{h}{c} \text{ and } \lambda=\frac{\mu\omega r^2}{P_a c^2} \tag{5.2}$$

where

$$P_a = P_l \tag{5.3}$$

Also, non-dimensional boundary conditions become,

$$P_{ln}=1 \text{ and } P_{hn}=P_h/P_l \tag{5.4}$$

Solving Equation (5.1) for these boundary conditions, various design parameters such as lifting force acting on the seal, friction force, and attitude angle can be evaluated. In addition, using the lifting force and minimum film thickness, stiffness of the fluid film and natural frequency of the seal assembly can be calculated. Once minimum film thickness is known, leakage flow through seal can be estimated. All of these concepts are important to evaluate the overall performance of the flexible seal. The region in which the seal is most likely to operate was determined and design

parameters were chosen accordingly. Therefore, for the seal analysis results presented in this section following design parameters and boundary conditions are used:

$$B/D = \frac{15}{130}, \frac{20}{130}, \frac{25}{130}, \frac{30}{130}$$

$$\lambda = 0.01 - 0.21$$

$$\varepsilon = 0.7 - 0.95$$

$$P_h / P_l = 10/7$$

5.2 Evaluation of Seal Load Ratio Variation

Figures (5.1-5.4) present the variation of load ratios with respect to these design parameters. Note that all these figures contain dimensionless design parameters as in the figures of previous chapter. There are two limiting conditions to calculate the load capacity. The first one is the ratio of pressures at the boundaries, P_h / P_l. The second limitation is the length to diameter ratio, B/D, of the seal. The design charts below are plotted for the particular, P_h / P_l which is 10/7, and for the certain B/Ds, which are ranging from 15/130 to 30/130. Any seal design which has the stated non-dimensional design properties and pressure boundary conditions would show the load ratio characteristics defined in the following figures corresponding to the selected eccentricity ratio ε and compressibility number λ. Load ratio is the non-dimensional representation of lifting force and evaluated from the results of FEA.

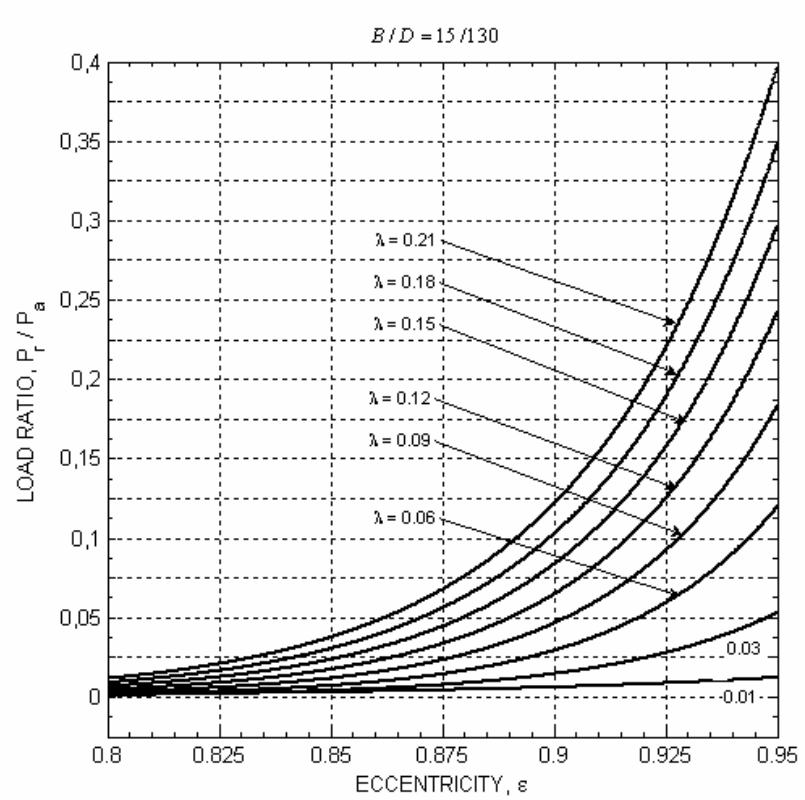

Figure 5.1 Load ratio vs. eccentricity ratio; P_h/P_l = 10/7, B/D = 15/130

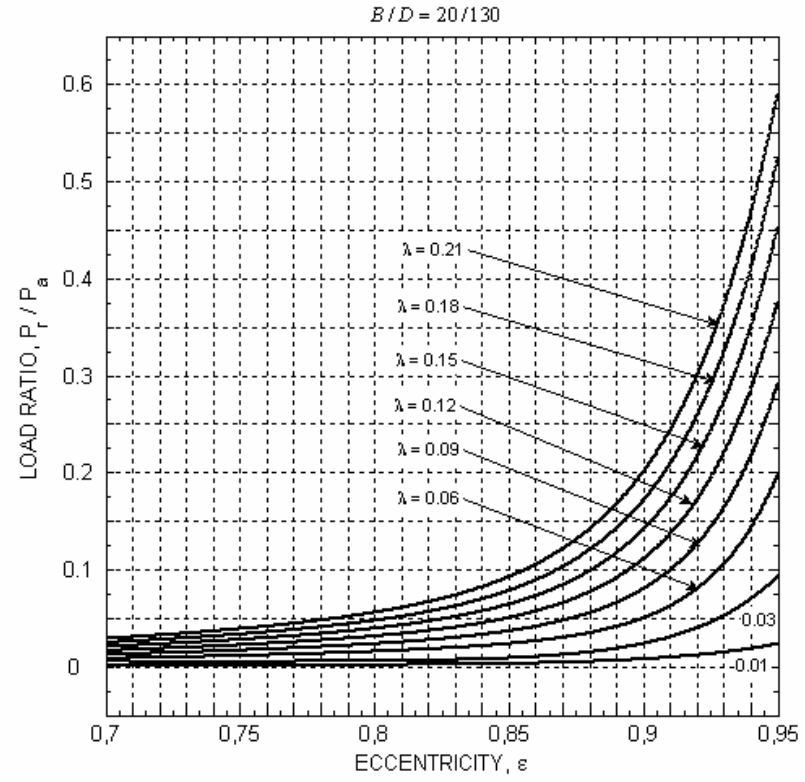

Figure 5.2 Load ratio vs. eccentricity ratio; P_h/P_l = 10/7, B/D = 20/130

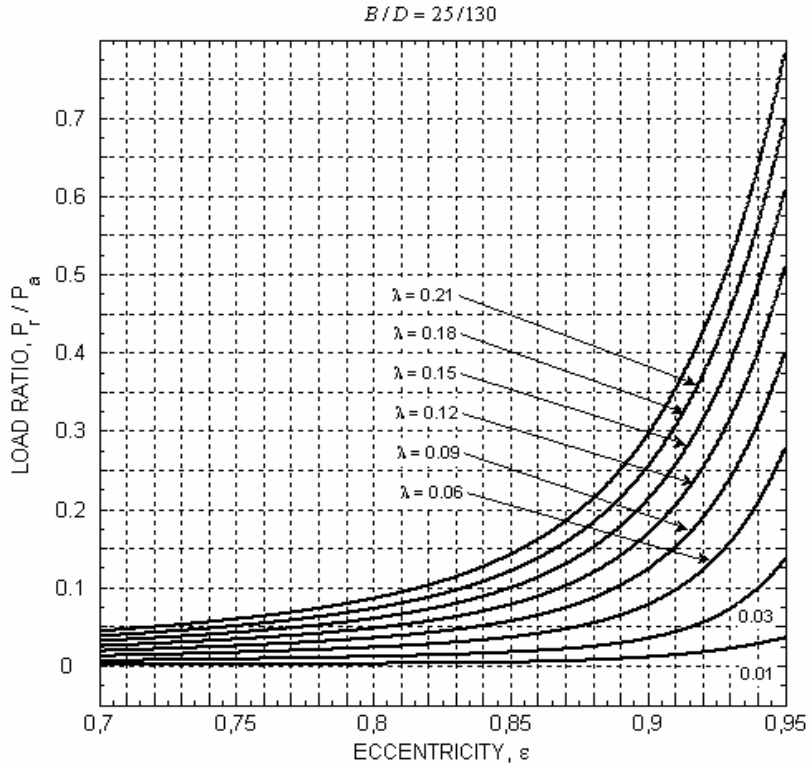

Figure 5.3 Load ratio vs. eccentricity ratio; P_h/P_l = 10/7, B/D = 25/130

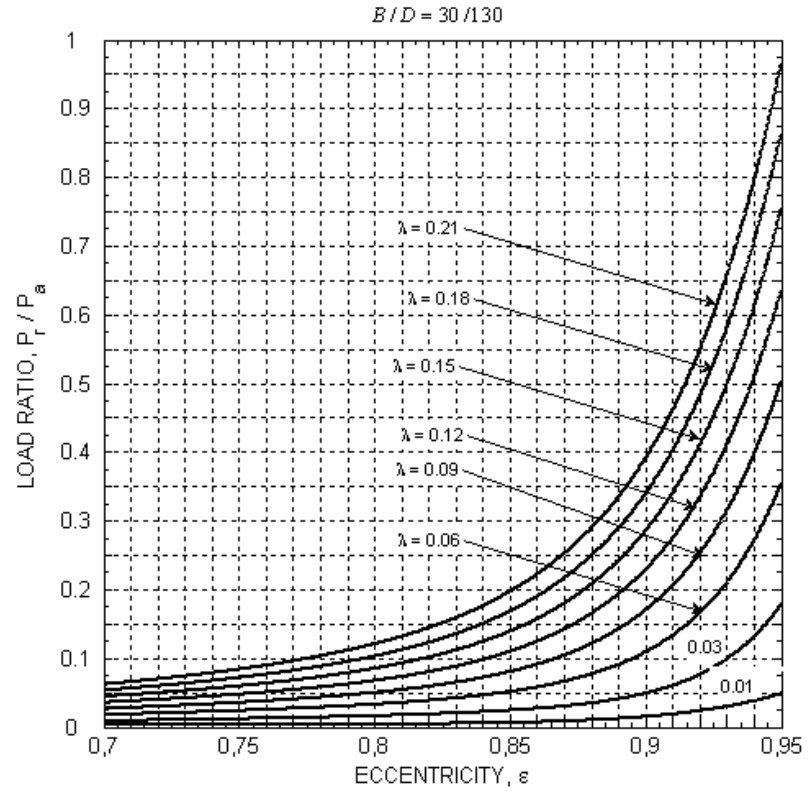

Figure 5.4 Load ratio vs. eccentricity ratio; P_h/P_l = 10/7, B/D = 30/130

These figures represent a general design case which is specialized by the ratio of boundary pressures and length to diameter ratio of the seal. Variation of load ratio on the flexible seal can be obtained for certain compressibility numbers from these figures. When the designed seal has a different compressibility number than the certain values displayed on the figures, one can make an approximation to the load ratio of the nearest compressibility number. Therefore, for various compressibility numbers, the magnitude of lifting force acting on the seal can be evaluated.

Until now, load ratios have been demonstrated as non-dimensional data with respect to eccentricity ratio and compressibility numbers. To investigate the lifting force, natural frequency and leakage rate in dimensional terms, a typical seal (Figure 5.5), which is assumed to be operating at 538^{o}C (1000^{o}F), is analyzed with the following operating parameters and boundary conditions:

$$T = 1000^{\circ}\text{F}$$
$$D = 0.13 \text{ m.} = 5.1 \text{ in.}$$
$$c = 50 \times 10^{-6} \text{ m.} \cong 0.002 \text{ in.}$$
$$\omega = 10000 \text{ rpm} = 1047 \text{ rad/s}$$
$$\mu = 3.751 \times 10^{-5} \text{ N-s/m}^2 \text{ at } 1000^{\circ}\text{F}$$
$$P_a = P_l = 700 \text{ KPa} \cong 100 \text{ psia}$$
$$P_h = 1000 \text{ KPa} \cong 145 \text{ psia}$$

For the design parameters and boundary conditions above, four flexible seals with different lengths are modeled and analyzed with finite elements. Lengths of these seals are:

$$B_1 = 0.03 \text{ m.}$$
$$B_2 = 0.025 \text{ m.}$$
$$B_3 = 0.02 \text{ m.}$$
$$B_4 = 0.015 \text{ m.}$$

Compressibility numbers of these seals are calculated from the following relation,

$$\lambda = \frac{\mu \omega r^2}{P_a c^2} \rightarrow \lambda = \frac{3.751e-5 \cdot 1047 \cdot (0.13/2)^2}{700000 \cdot (50e-6)^2} \tag{5.5}$$

$$\lambda \cong 0.094 \tag{5.6}$$

As it is realized from (5.5), seal length, B, does not affect the compressibility number, λ. Therefore, λ is the same for the designed four seals.

Based on these design parameters and boundary conditions, our aim is to evaluate the lifting force, natural frequency and leakage rates for this seal in variable lengths.

5.3 Lifting Force Analysis

Aerodynamic lift force analysis is based on the eccentricity ratio evaluation of the journal at which the created aerodynamic force is capable of resisting to the sum of bearing weight and frictional resistance at seal backing plate due to the axial pressure force acting on the bearing. As stated earlier, major concern is to obtain the necessary lifting force without violating the required minimum film thickness between the shaft and seal surfaces. The practical limit for this thickness is around 2 μm.

It is also important to note that load ratio and lifting force are not two different concepts but related to each other. Load ratio P_r is the ratio of lifting force F_n to the ambient pressure P_a multiplied by the projected bearing area $2rB$. In other words, load ratio is the dimensionless representation of lifting force. For bearing applications, lifting force should be equal to the total radial loads on rotor to keep it stable. For the flexible seal designs under consideration, lifting force should at least be equal to the sum of bearing weight and friction force F_s produced by the differential pressure acting on the seal. Measurements indicate that metal cloth stiffness is very low and negligible. Therefore, force exerted by the metal cloth is not included in the calculation of total resistive force. Figure (5.5) demonstrates all these forces.

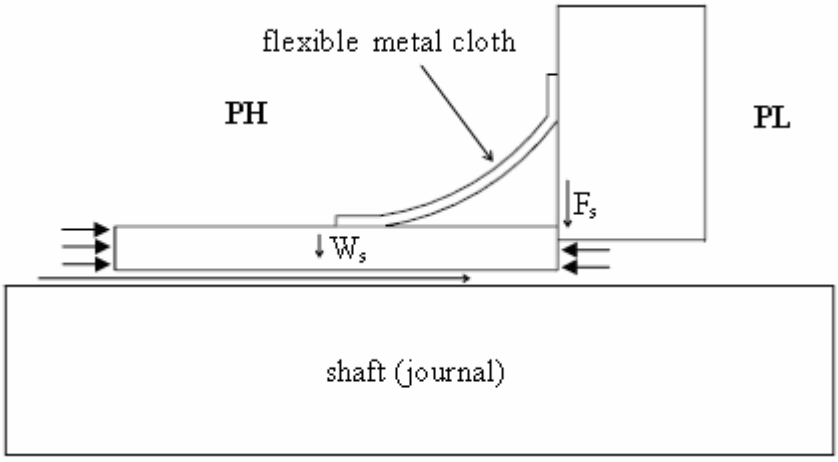

Figure 5.5 Forces acting on the novel seal

We can calculate the necessary lifting force as follows:

$$F_n = W_s + F_s \tag{5.7}$$

Friction force becomes

$$\begin{aligned} F_s &= \Delta P \times A_s \times \mu_f \\ &= (P_h - P_l) \times (\pi Ds) \times \mu_f \end{aligned} \tag{5.8}$$

where

A_s → side area of the seal ring

s → thickness of the seal ring

μ_f → seal ring-to-backing plate coefficient of friction

Technical sketch of the designed seal (Figure 2.11) demonstrates the proposed thickness of the seal ring, which is equal to 0.003 m. A typical steel-to-steel friction coefficient can be taken as 0.5. Values of remaining parameters are defined earlier. So, friction force is calculated to be;

$$\begin{aligned} F_s &= (1000000 - 700000) \times (\pi \times 0.13 \times 0.003) \times 0.5 \\ &= 183.78 \cong 184 \text{ N} \end{aligned} \tag{5.9}$$

For the given typical design values, total mass of the seal with the flexible metal cloth is

$$M_s = 351.03 \text{ g.}$$

making the force exerted by bearing weight as

$$W_s = 3.5 \text{ N}$$

Then the total lifting force, which resists to the weight of the seal and to the friction force between the seal and the backing plate, is calculated as

$$\begin{aligned} F_n &= 184 + 3.5 \\ &= 187.5 \text{ N} \end{aligned}$$

Therefore, once the force equilibrium reached at a certain eccentricity, the aerodynamic lift force equals 187.5 N.

For the seal designs under consideration, FEA gives the following eccentricity values at which the aerodynamic lift force is equal to 187.5 N.

	Load Ratio P_r / P_a	ε	h_{min}	corresponding figure
B = 0.03 m.	0.0686	0,83	8.5 μm	Figure 5.4
B = 0.025 m.	0.0824	0,873	6.35 μm	Figure 5.3
B = 0.02 m.	0.1030	0,909	4.55 μm	Figure 5.2
B = 0.015 m.	0.1373	0,94	3 μm	Figure 5.1

Table 5.1 Eccentricity ratios of designed seals corresponding to 187.5 N lifting force

Note that these values can also be obtained approximately from the corresponding figures without conducting any FEA. Design charts are functional in that sense. For a specific case, if the ratio of downstream pressure to the upstream pressure, and the ratio of seal diameter to the seal length are known, one can determine load ratio from the design charts. Then, using the relation between lifting force and load ratio, exact value of the lifting force can be evaluated.

The results in Table (5.1) show that the design case for which the seal length is 0.015 m. has a minimum film thickness of 3 μm. As stated before, 1 μm is a critical lower limit for the film thickness. For the worst case scenario, this critical limit can extend up to 2 μm. If the bearing length is reduced below 0.015 m., minimum film thickness must also be reduced to create the necessary lifting force. In such a case, asperities of the seal surface and shaft surface can contact and wear debris may occur. As a result, we can state that the necessary lifting force can be created safely if the seal is longer than 0.015 m.

5.4 Natural Frequency Analysis

Natural frequency analysis of the seal is important as it reveals the critical speeds for the overall system. Generally, natural frequency analysis is carried out for the rotating shaft which is coupled with a stiff bearing. The fluid film between the shaft and the bearing behaves as a nonlinear spring. If the shaft is considered to be a rigid mass, then in conjunction with the fluid-film spring there will be a natural frequency of vibration. With the integration of disturbing force coming from a residual unbalance in the system, resonant vibration occurs at shaft rotational speed. This is called “synchronous whirl”. The whirl has been observed as the center of the shaft orbiting the center of the bearing.

When the bearings are held with flexible supports, they can vibrate relative to the spinning shaft. It is called the synchronous whirl of bearings. The same situation is valid for our seal as it is attached with flexible metal cloth supports. So, we can think of our seal as a rigid mass coupled to the backing plate and shaft by springs. These two springs

have nonlinear characteristics. In addition, there is a constant friction force acting on the seal from one side. Figure 5.6 presents the free body diagram of the seal-shaft assembly.

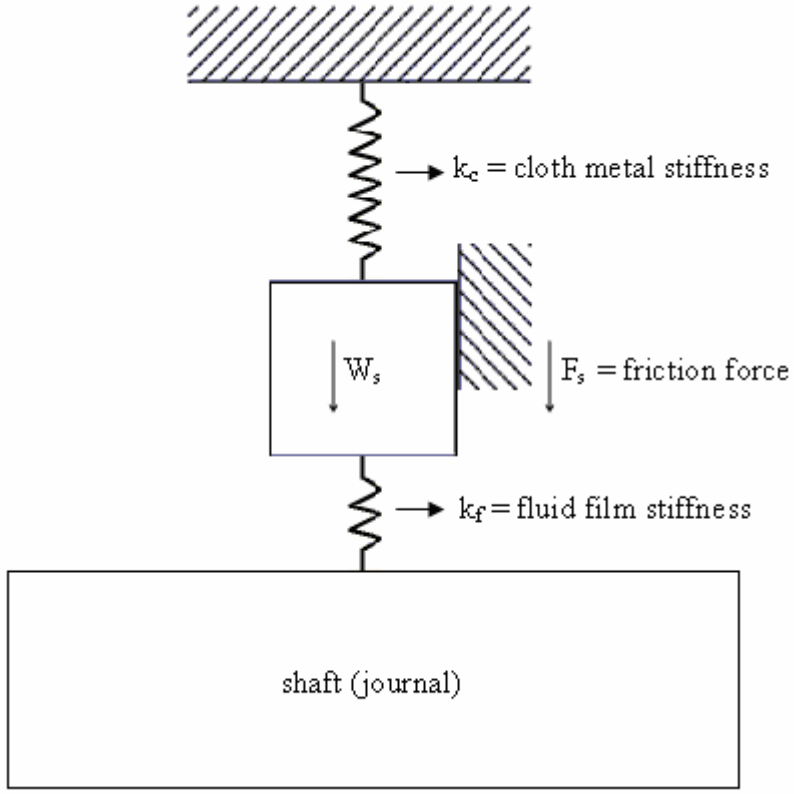

Figure 5.6 Free body diagram of seal-shaft assembly

A simplification of this free body diagram can be made by neglecting the metal cloth stiffness as measurements indicate it to be very low. In fact, neglecting the metal cloth stiffness is a worst case scenario for natural frequency analysis of the seal assembly. It is a common procedure in bearing design to make supports stiffer to keep the overall system in mechanically stable region.

If metal cloth stiffness is neglected, natural frequency of the system can be evaluated by the following relationship [4]:

$$f = \frac{1}{2\pi}\sqrt{\frac{k_f}{M_s}} \tag{5.10}$$

where k_f is the fluid film stiffness and M_s is the mass of the seal.

Since k_f is nonlinear, the value of it is strictly related to the operating conditions of the seal and shaft. For our design, it is important to evaluate the natural frequency of the seal when the lifting force is equal to the total resisting force, which is the sum of

weight and friction force. Therefore, we should calculate the fluid film stiffness of the designed seals around the eccentricities shown in Table 5.1. Note that fluid film stiffness can be calculated by the following relation [4]:

$$k_f = \frac{\Delta F_n}{|\Delta h_{\min}|} \tag{5.11}$$

By making very small perturbations around the operating eccentricities, fluid film coefficient can be evaluated. Values of lifting force around the equilibrium state are illustrated in the following tables. Corresponding stiffness coefficients are calculated below each table.

B = 0.03 m.	h_{min}	F_n
ε = 0.83	8.5 μm	187.5 N
ε = 0.84	8 μm	209.03 N
ε = 0.82	9 μm	170.81 N

Table 5.2 Values of lifting force around the equilibrium when B=0.03 m.

$$k_{f_{0.03}} = \frac{209.03 - 170.81}{(9e-6)-(8e-6)} = 38220000 \text{ N/m} \tag{5.12}$$

B = 0.025 m.	h_{min}	F_n
ε = 0.873	6.35 μm	187.5 N
ε = 0.876	6.2 μm	197.58 N
ε = 0.870	6.5 μm	180.58 N

Table 5.3 Values of lifting force around the equilibrium when B=0.025 m.

$$k_{f_{0.025}} = \frac{197.58 - 180.58}{(6.5e-6)-(6.2e-6)} = 50000000 \text{ N/m} \tag{5.13}$$

B = 0.02 m.	h_{min}	F_n
ε = 0.909	4.55 μm	187.5 N
ε = 0.912	4.4 μm	201.48 N
ε = 0.906	4.7 μm	176.35 N

Table 5.4 Values of lifting force around the equilibrium when B=0.02 m.

$$k_{f_{0.02}} = \frac{201.48 - 176.35}{(4.7e-6)-(4.4e-6)} \cong 83760000 \text{ N/m} \tag{5.14}$$

B = 0.015 m.	h_{min}	F_n
ε = 0.94	3 μm	187.5 N
ε = 0.942	2.9 μm	200.35 N
ε = 0.938	3.1 μm	175.59 N

Table 5.5 Values of lifting force around the equilibrium when B=0.015 m.

$$k_{f_{0.015}} = \frac{200.35 - 175.59}{(3.1e-6) - (2.9e-6)} = 123800000 \text{ N/m} \tag{5.15}$$

It is noted that fluid film stiffness is increasing when the seal length decreases. It is an expected outcome because of the fact that a reduction in seal length also reduces the area of seal surface which is exposed to the aerodynamic pressure. Thus, in order to create the same lifting force, seal must operate at higher eccentricities. For similar reasons lubricated journal bearings are also designed to operate at high eccentricity levels for the sake of stability. As illustrated in Figures (5.1 – 5.4), the load ratio is increasing exponentially with respect to the eccentricity of the seal. Therefore, for the same seal, if the bearing length decreases, fluid film stiffness increases. However, the need for a safe/minimum film thickness should not be overlook to avoid excessive seal wear.

In order to calculate the natural frequency of the seal system, mass of the seal is needed. If we plug calculated fluid film stiffness and the mass of the seal into Equation (5.10), the natural frequencies are obtained as shown below,

$$f_{0.03} = 1663 \text{ hz} \cong 100000 \text{ rpm}$$

$$f_{0.025} = 2025 \text{ hz} \cong 120000 \text{ rpm}$$

$$f_{0.02} = 2462 \text{ hz} \cong 145000 \text{ rpm}$$

$$f_{0.015} = 2993 \text{ hz} \cong 180000 \text{ rpm}$$

Since our seal is designed to run at 10000 rpm, operating range is well below the calculated critical speeds. Essentially, when the seal length is decreased, mass of the seal is also reduced. Reducing mass will also increase the natural frequency of the system. Since the obtained natural frequencies are extremely high, a common value of 0.35 kg is used for the analysis without loss of generality.

The key factor for the very high values of natural frequencies is the excessive friction force acting on the seal. Note that the value of friction force is approximately 50 times larger than the weight of the seal. Therefore, we require a very high lifting force

to move such a small mass. This increases the natural frequency of the system as it is also verified by the relation (5.10).

Analyses indicate that natural frequency is not an active design constraint for the seal operating at these conditions. Note that when the speed of the rotor increases, shaft can operate at lower eccentricities to produce the same lifting force. Therefore, stiffness of the fluid film and natural frequency of the system are expected to decrease. It should be noted that for high speed dynamic systems like gas turbines and aircraft engines, there may be other very high frequency excitations. Care should be taken to avoid such high frequency excitation coupling. Therefore, a detailed natural frequency analysis should be performed for each specific design case and for every operating condition.

5.5 Leakage Flow Analysis

One of the most important performance criteria for the seal is the leakage rate through the gas film or seal-rotor clearance. As stated earlier, brush seals are widely used in turbo machinery. It is reported that leakage rates of brush seals are substantially low with respect to that of labyrinth seals. For a brush seal, in addition to the primary leakage flows through the bristle-rotor clearance, there is also a secondary flow through bristles. Other effects such as hysteresis and blow-down make the calculation of actual leakage through brush seal rather difficult.

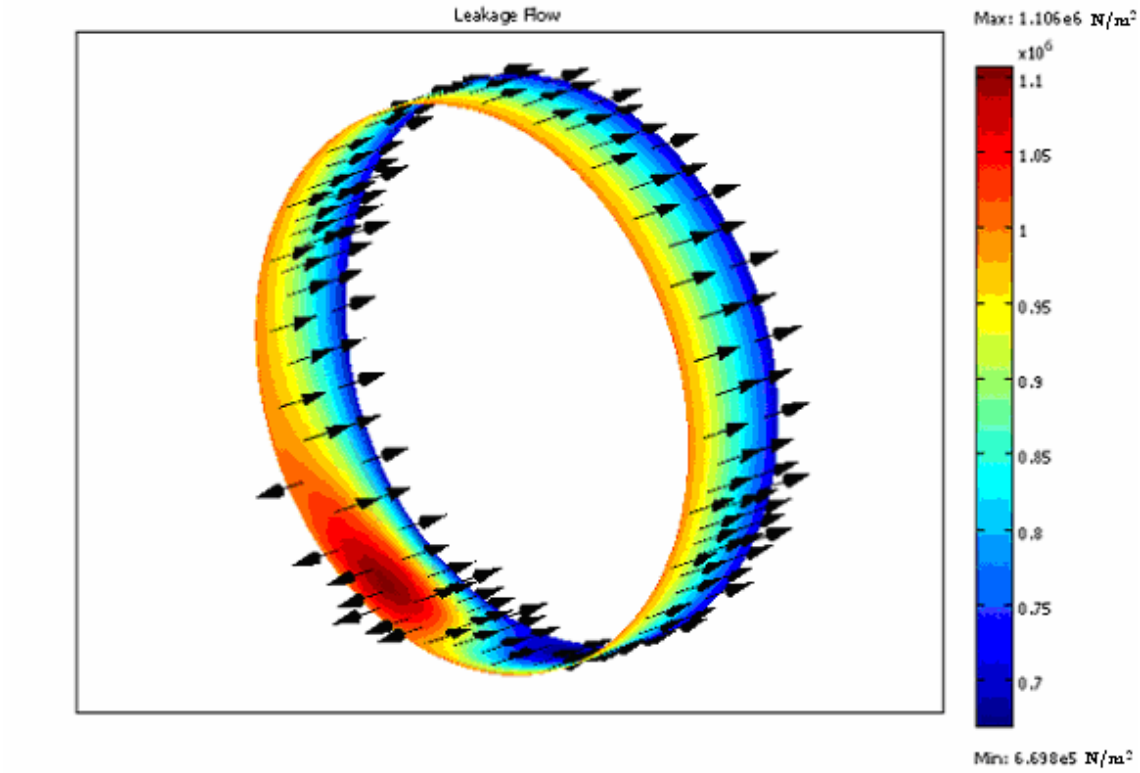

Figure 5.7 Leakage flow across the seal boundary

For the presented seal system, leakage through seal-rotor clearance is nothing but the integration of axial velocity on the cross section of the channel gap. There is no blow-down phenomenon that can affect the amount of leakage through the gap. Figure 5.7 represents the leakage flow through the channel gap of the seal. Color bar on the right hand side shows the pressure scale. It is observed that there is also a leakage flow in the direction to the upstream pressure side. This is somewhat expected due to the fact that there are local boundaries inside the channel gap for which the value of the aerodynamic pressure is higher than the value of upstream pressure.

The axial component of the flow velocity in Equation (3.43) was obtained earlier. As noted from Equation (3.43), leakage flow is pressure driven. It is also important to note that the density of gas film is not constant throughout the channel gap. Therefore, the amount of mass passing through the channel gap must be evaluated instead of the volumetric flow. In other words, conservation of volume assumption is not valid in our case since air in the channel is compressible. Taking into account the compressibility of air, we can obtain the mass flow rate for leaking air as follows,

$$mf = \int_0^{2\pi r} \int_0^{h(\theta)} (\rho v) dz d\theta \tag{5.16}$$

where ρ is the density of the air and dependent on the boundary location, and v is the axial flow velocity of leaking air. Substituting Equation (3.43) in Equation (5.16), the following relation for the mass flow rate is obtained:

$$mf = \int_0^{2\pi r} \int_0^{h(\theta)} \rho \left[\frac{1}{2\mu} \frac{\partial P}{\partial y} \left(z^2 - zh(\theta) \right) \right] dz d\theta \tag{5.17}$$

It has been shown earlier that pressure and density of air do not change along the z direction. Similarly, μ is constant throughout the fluid film and h varies only in the circumferential direction. Thus, we can easily take the integration with respect to z. As a result, Equation (5.17) reduces to

$$mf = \int_0^{2\pi r} \frac{\rho \left(h(\theta) \right)^3}{12\mu} \frac{\partial P}{\partial y} d\theta \tag{5.18}$$

Analytic integration of the above equation is very difficult if at all possible. Integrating it numerically will be easier. COMSOL has a useful tool which can take boundary integration on the defined surface. Taking the integration and then dividing the result to the seal length gives us the mass flow rate of air. We obtain the following mass flow rates for the designed seal:

	ε	mf (lb/s)	mf (kg/s)	effective clr. (in.)	effective clr. (μm)
B = 0.03 m.	0,83	0,0186	0,0084	0,00062	15,748
B = 0.025 m.	0,873	0,0235	0,0107	0,00078	19,812
B = 0.02 m.	0,909	0,0307	0,0139	0,00102	25,908
B = 0.015 m.	0,94	0,0425	0,0193	0,00141	35,814

Table 5.6 Mass flow rate and effective clearances for the novel seal, Fn=187.5 N

Table 5.6 also contains effective clearance data for the seals. Effective clearance is a measure of seal leakage performance that allows comparison of various seals. Note that the mounting clearance of our seal is roughly 2 mils, i.e. 50 μm. Obtained effective clearance values show that the leakage performance of the designed seal is comparable or better than brush seals. Figures (5.8) and (5.9) demonstrate the effect of eccentricity on the leakage rates of new seal.

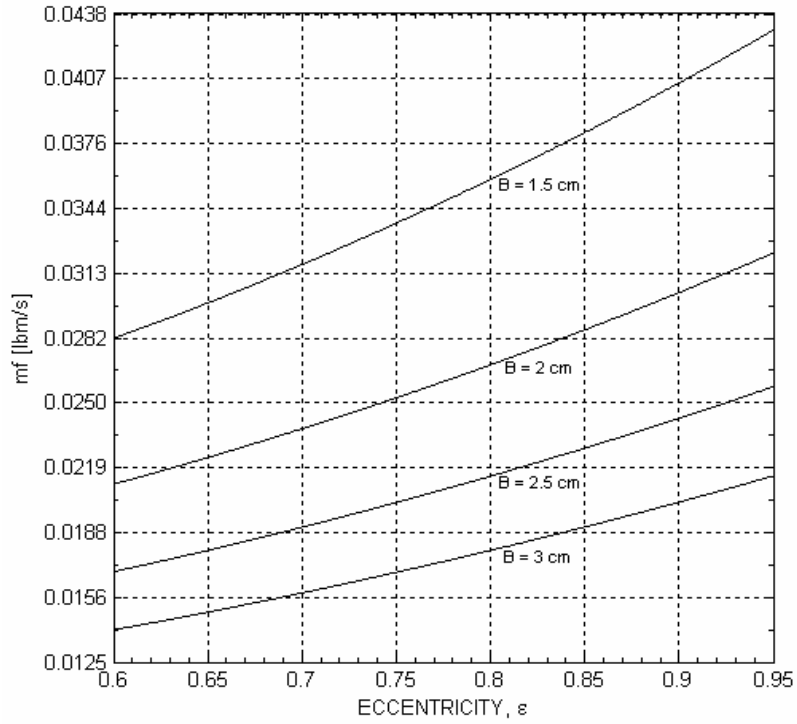

Figure 5.8 Relationship between mass flow rate and eccentricity ratio of the designed seal

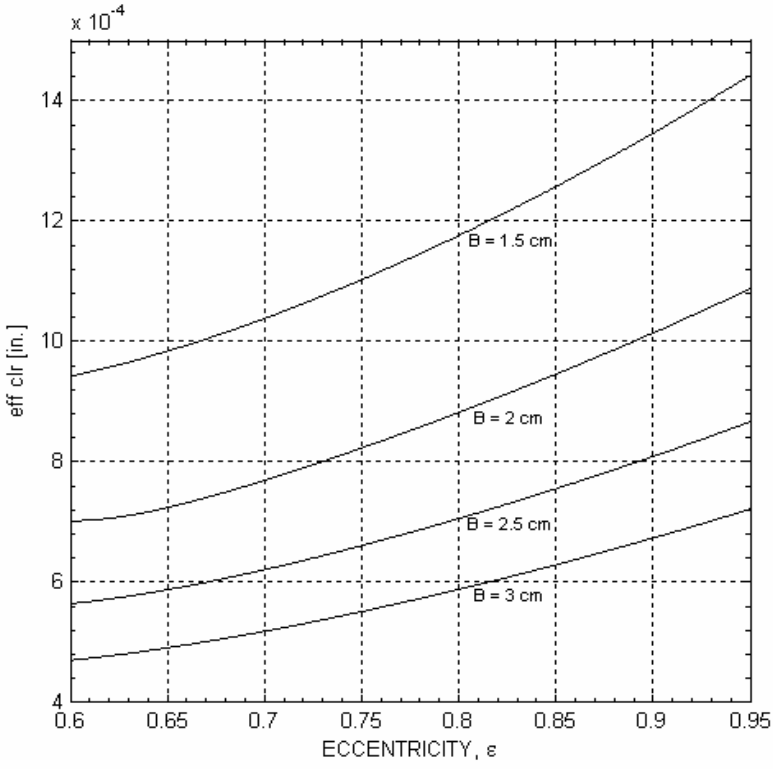

Figure 5.9 Relationship between effective clearance and eccentricity ratio of the designed seal

A comparison between the leakage rates of the new flexible seal and traditional brush seals is demonstrated in Figure 5.10. Effective clearance of the new seal design with varying seal lengths are illustrated with respect to differential pressure. Leakage rates of these seals are compared with two different brush seals which have different clearances. One of the brush seals is interfering with the rotor surface by 0.002 in. while the other one has a 0.008 inch clearance. Notice that the new seal designs show comparable leakage performances with brush seals. At low differential pressures, novel seal designs, which have 0.002 in. mounting clearances, leak even less than the brush seal mounted with 0.002 in. interference.

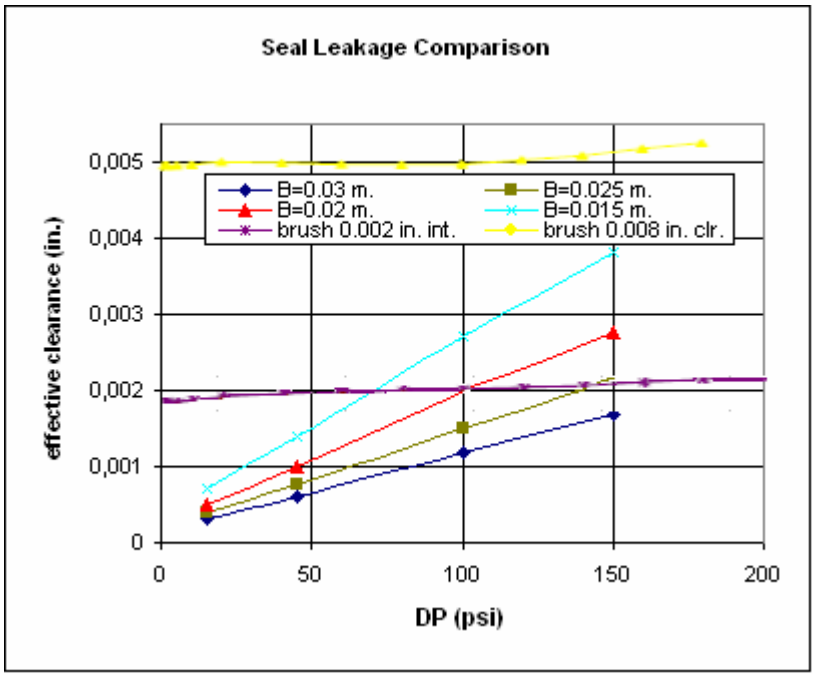

Figure 5.10 Comparison of leakage performance between novel seal and brush seal [48]

One drawback for the new seal design is that leakage rate gradually increases with differential pressure. However, if axial space is available, this problem can be resolved by increasing seal axial length. In brush seals, effective clearance level is stabilized by the effect of blow-down force [48]. Brush seals require higher clearances compared to the proposed seal design because of the fact that rubbing contact may create problems during transient conditions for critical locations like steam turbine applications. However, this is not a limitation for the proposed seal since a possible physical contact is avoided by the flexible seal attachment.

6 CONCLUSION

Turbomachinery designers face real engineering challenges in sealing applications where high speeds and large pressure loads are accentuated by elevated operating temperatures. Traditional labyrinth seals are being replaced by more effective brush seal technology. However, increasing power and efficiency demands pushed brush seals to their limits at high speed and high temperature applications where extended service life is required. Physical contact between the bristle tips and rotor becomes inevitable and wear rub-heat problems come into the picture. This work presents a design and analysis work for a low cost long life alternate seal design to retire some of the contact related problems.

Applying established gas bearing working principles, a novel seal design is proposed. The design involves a simple rigid/semi-flexible seal ring that is attached to a stationary support plate via flexible metal cloth structure. The seal body is capable of moving under the effect of aerodynamic lift force. Therefore, above a certain clearance limit, which ensures that asperity contact is avoided, the seal follows shaft excursions to avoid damaging hard rubs.

In order to guarantee sufficient aerodynamic force at acceptable clearances, a detailed lifting force analysis was carried out based on gas film lubrication theory. For this purpose, governing Reynolds equation for compressible gas flow was solved for pressure distributions using both finite difference and finite element methods. After confirming that results of both methods agree well to each other, analysis results were validated with other published work in literature. Relative difference in between is on the order of 0.01 demonstrating that results are fitting well to each other.

Following analysis validation, the solution procedure has been applied to the novel seal design with proper pressure boundary conditions. Four different seals with varying geometries were designed, and resulting lifting forces were evaluated. It is verified that necessary lifting force for these seals can be obtained without exceeding lower limits of

lift clearance. Furthermore, to ensure dynamic stability of the sealing system, natural frequency analyses were conducted. Results for analysis under typical operating conditions indicated that seal natural frequencies are well above rotor operating speeds. Finally, leakage analysis of new seal system was performed. A comparison with brush seal leakage performance rates has been also provided. .

A comparison between designed seals illustrate that leakage rate increases with decrease in the seal length. Specifically, a seal with 1.5 cm. axial length has a leakage rate twice the leakage rate of the seal with 3 cm. axial length. Note that leakage rate is proportional to the third power of the seal gap theoretically. Therefore, seal performance is sensitive to preset operating clearance. The seal with 1.5 cm length has a minimum film thickness equal to 3 μm. This is above the lower clearance limit of around 2 μm. However, seals designs with larger axial length provide better leakage performance with higher film thickness values.

Overall, it is observed that under typical operating conditions all of the analyzed seal designs show satisfactory leakage performances that are similar to that of brush seals. Proposed seal design is nothing but an assembly of metal cloth and seal ring coupled together. Metal cloth functions as a bridge between seal ring and backing plate. Therefore, it gives flexibility to the whole seal body under the action of applied aerodynamic force. Owing to the simple mechanical structure of the proposed seal design, manufacturing and maintenance costs are expected to be substantially low with respect to brush seals and other mechanical seals in the market. In addition, avoiding seal-rotor contact during operation provides longer seal life and higher operating temperature capabilities. As a result, the analyses indicate that the proposed new sealing system may provide a viable alternative to current engine seals.

REFERENCES

[1] S. Dinc, G. Reluzco, N. A. Turnquist, J. Lawen, O. Kerber, F. Brunner, G. Crum, A. E. Stuck, R. H. Cromer, P. T. Marks, R. P. Chiu, C. E. Wolfe, and P. Crudgington, "Brush Seals in Industrial Gas Turbines - Turbine Section Interstage Sealing," presented at 34th AIAA/ASME/SAE/ASEE Joint Propulsion Conference & Exhibit, Cleveland, OH, 1998.

[2] L. P. Ludwig and R. C. Bill, "Gas Path Sealing in Turbine Engines," presented at ASLE/ASME Lubrication Conference, Minnesota, 1978.

[3] F. M. White, *Viscous Fluid Flow*, Third ed. New York: McGraw - Hill, 2006.

[4] D. D. Fuller, *Theory and Practice of Lubrication for Engineers*. New York: Wiley, 1984.

[5] B. Bhushan, *Introduction to Tribology*. New York: John Wiley & Sons, 2002.

[6] B. J. Hamrock, *Fundamentals of Fluid Film Lubrication*. New York: McGraw - Hill, 1994.

[7] A. Cameron, *Principles of Lubrication*. London: Longman, 1966.

[8] W. A. Gross, *Gas Film Lubrication*. New York: John Wiley & Sons, 1962.

[9] T. A. Stolarski, *Tribology in Machine Design*. Oxford: Butterworth-Heinemann, 1990.

[10] G. B. Karelitz and J. N. Kenyon, "Oil-Film Thickness at Transition from Semifluid to Viscous Lubrication," *Transactions of ASME*, vol. 59, pp. 239-246, 1937.

[11] S. A. McKee, "Effect of Running In on Journal-Bearing Performance," *Mechanical Engineering*, vol. 49, pp. 1335-1340, 1927.

[12] T. E. Stanton, *Friction*: Longmans, Green & Co., 1923.

[13] M. F. Hwang, A. Pope, and B. Shucktis, "Advanced Seals for Engine Secondary FlowPath," presented at 31st AIAA/ASME/SAE/ASEE Joint Propulsion Conference and Exhibit, San Diego, CA, 1995.

[14] G. M. Gorelov, V. E. Reznik, and V. I. Tsibizov, "Experimental Study of Brush Seal Flow Characteristics and Comparison with a Labyrinth Seal," *Izvestiya VUZ. Aviatsionnaya Tekhnika*, vol. 31, pp. 43-46, 1988.

[15] M. F. Aksit, "A Computational Study of Brush Seal Contact Loads with Friction," *PhD Thesis*, 1998.

[16] J. G. Ferguson, "Brushes as High Performance Gas Turbine Seals," *ASME Gas Turbine and Aeroengine Congress Paper ASME 88-GT-182*, 1988.

[17] J. A. Carlile, R. C. Hendricks, and D. A. Yoder, "Brush Seal Leakage Performance with Gaseous Working Fluids at Static and Low Rotor Speed Conditions," *Journal of Engineering for Gas Turbines and Power*, vol. 115, pp. 397-403, 1993.

[18] R. E. Chupp and P. Nelson, "Evaluation of Brush Seals for Limited-Life Engines," presented at AIAA/SAE/ASME/ASEE 26th Joint Propulsion Conference, Orlando, FL, 1990.

[19] G. F. Holle and M. R. Khrishnan, "Gas Turbine Engine Brush Seal Applications," presented at AIAA/SAE/ASME/ASEE 26th Joint Propulsion Conference, Orlando, FL, 1990.

[20] E. T. Duran, "Analysis of Shear Heating and Effect of Temperature Dependant Viscosity on Hydrodynamic Lift of Oil Brush Seals," *MSc Thesis*, 2006.

[21] P. Basu, A. Datta, R. Johnson, R. Loewenthal, and J. Short, "Hysteresis and Bristle Stiffening Effects of Conventional Brush Seals," presented at AIAA/SAE/ASME/ASEE 29th Joint Propulsion Conference, AIAA 93-1996, 1993.

[22] R. C. Hendricks, J. Wilson, T. Wu, and R. Flower, "Bidirectional Brush Seals," *ASME Gas Turbine and Aeroengine Congress Paper ASME 97-GT-256*, 1997.

[23] J. F. Short, P. Basu, A. Datta, R. G. Loewenthal, and R. J. Prior, "Advanced Brush Seal Development," presented at AIAA/SAE/ASME/ASEE 32nd Joint Propulsion Conference, AIAA 96-2907, 1996.

[24] G. K. Arora and M. P. Proctor, "JTAGG II Brush Seal Test Results," presented at AIAA/SAE/ASME/ASEE 33rd Joint Propulsion Conference, AIAA 97-2632, 1997.

[25] G. L. Agrawal, "Foil Air/Gas Bearing Technology ~ An Overview," presented at International Gas Turbine & Aeroengine Congress & Exhibition, ASME, Orlando, Florida, 1997.

[26] K. Radil, S. Howard, and B. Dykas, "The Role of Radial Clearance on the Performance of Foil Air Bearings," *Tribology Transactions*, vol. 45, pp. 485-490, 2002.

[27] C. Dellacorte and M. J. Valco, "Load Capacity Estimation of Foil Air Journal Bearings for Oil-Free Turbomachinery Applications," *Tribology Transactions*, vol. 43, pp. 795-801, 2000.

[28] C. Dellacorte, V. Lukaszewicz, M. J. Valco, K. C. Radil, and H. Heshmat, "Performance and Durability of High Temperature Foil Air Bearings for Oil-Free Turbomachinery," *Tribology Transactions*, vol. 43, pp. 774-780, 2000.

[29] R. Ongun, M. F. Aksit, and G. Goktug, "A simple Model for Wear of Metal Cloth Seals," presented at 40th AIAA/SAE/ASME/ASEE Joint Propulsion Conference & Exhibit, AIAA-2004-3892, Fort Lauderdale, Florida, 2004.

[30] Y. Dogu, M. F. Aksit, B. Bagepalli, J. Burns, B. Sexton, and I. Kellock, "Thermal and Flow Analysis of Cloth-Seal in Slot for Gas Turbine Shroud Applications," presented at AIAA/SAE/ASME/ASEE 34th Joint Propulsion Conference, AIAA 98-3174, 1998.

[31] M. F. Aksit, B. Bagepalli, M. Demiroglu, M. Dinc, I. Kellock, and T. Farrell, "Advanced Flexible Seals for Gas Turbine Shroud Applications," presented at AIAA/SAE/ASME/ASEE 35th Joint Propulsion Conference, AIAA 99-2827, 1999.

[32] J. S. Ausman, "Theory and Design of Self-Acting, Gas-Lubricated Journal Bearings Including Misalignment Effects," presented at International Symposium on Gas-Lubricated Bearings, Office of Naval Research, Dept. of the Navy, Washington, 1959.

[33] J. S. Ausman, "An Improved Analytical Solution for Self-Acting, Gas-Lubricated Journal Bearings of Finite Length," *Journal of Basic Engineering*, vol. 83, pp. 188-194, 1961.

[34] B. Sternlicht and R. C. Elwell, "Theoretical and Experimental Analysis of Hydrodynamic Gas-Lubricated Journal Bearings," *Transactions of ASME*, vol. 80, pp. 865-878, 1958.

[35] H. G. Elrod, Jr., and S. B. Malanoski, "Theory and Design Data for Continuous-Film, Self-Acting Journal Bearings of Finite Length," Report I-A 2049-13, The Franklin Institute Laboratories for Research and Development 1960.

[36] A. A. Raimondi, "A numerical Solution for the Gas Lubricated Full Journal Bearing of Finite Length," *Tribology Transactions*, vol. 4, pp. 131-155, 1961.

[37] N. Arakere and H. D. Nelson, "An Interior Collocation Method for Static and Dynamic Analysis of Finite Length Gas Journal Bearings," *Transactions of the ASME*, vol. 110, pp. 456-461, 1988.

[38] G. Belforte, T. Raparelli, and V. Vikforov, "Theoretical Investigation of Fluid Inertia Effects and Stability of Self-Acting Gas Journal Bearings," *Transactions of the ASME*, vol. 121, pp. 836-843, 1999.

[39] G. Belforte, T. Raparelli, and V. Vikforov, "Modeling and Identification of Gas Journal Bearings: Self-Acting Gas Bearing Results," *Transactions of the ASME*, vol. 124, pp. 716-724, 2002.

[40] E. Cetinsoy, "Analysis of Hydrodynamic Lift for Gas Turbine Oil Seals," *MSc Thesis*, 2006.

[41] A. A. Raimondi and J. Boyd, "A Solution for the Finite Journal Bearing and its Application to Analysis and Design: I, II, III," *Tribology Transactions*, vol. 1, pp. 159-209, 1958.

[42] B. Bhushan, *Tribology and Mechanics of Magnetic Storage Devices*, 2nd ed. New York: Springer-Verlag, 1996.

[43] W. A. Gross, L. A. Matsch, V. Castelli, A. Eshel, J. H. Vohr, and M. Wildmann, *Fluid Film Lubrication*. New York: Wiley, 1980.

[44] A. Burgdorfer, "The Influence of the Molecular Mean Free Path on the Performance of Hydrodynamic Gas Lubricated Bearings," *Journal of Basic Engineering*, vol. 81, pp. 94-100, 1959.

[45] S. G. Kandlikar, S. Garimella, D. Li, S. Colin, and M. R. King, *Heat Transfer and Fluid Flow in Minichannels and Microchannels*. Oxford: Elsevier, 2006.

[46] M. H. Holmes, *Introduction to Numerical Methods in Differential Equations*. New York: Springer, 2007.

[47] G. W. K. Ford, D. M. Harris, and D. Pantall, "Principles and Applications of Hydrodynamic-Type Gas Bearings," *Proc. Inst. Mech. Engrs.*, vol. 171, pp. 93-113, 1957.

[48] P. F. Crudgington and A. Bowsher, "Brush Seal Blow Down," *AIAA Paper No 2003-4697*.

Appendix A

Complete Finite Difference Code to Solve Governing Compressible Reynolds Equation

```
close all
clear all
clc
format long


% Bearing Parameters

r = 0.065;          % m    - radius of bearing/seal/shaft
B = 0.03;           % m     - axail length (width) of bearing/seal
c = 5e-5;           % dimensionless - clearance
eps = 0.8           % dimensionless - eccentricity ratio
nu = 3.751e-5;      % N-s/m^2 - dynamic viscosity
Pl = 1;             % dimensionless downstream pressure
Ph = 10/7;          % dimensionless upstream pressure
w = 10000*2*pi/60;  % rad/s - linear velocity
Pa = 700000;        % N/m^2 - ambient pressure

comp_rat = (r/c)^2*nu*w/Pa; % - compressibility ratio

% Discretization Parameters
M = 450; % z,j
N = 500; % theta,i

% Discretized Lengths
dz = B/r/(M+1);
dt = 2*pi/N;

cons = 6*comp_rat;


% %%%%%%%%%%%%%%% Boundary Conditions %%%%%%%%%%%%%

% bottom boundary
gb = zeros (1,N+1);
for i=1:N+1
    gb(i)= Pl;
end

% top boundary
gt = zeros (1,N+1);
for i=1:N+1
    gt(i)= Ph;
end

%%%%%%%%%%%%% ================== %%%%%%%%%%%%%%

P = (Ph+Pl)/2.*ones(M*N,1);   % pressure vector
Pi = P-2;   % initial pressure
```

```
ups = 0;    % error condition 1
bups = 0;   % error condition 2

iter = 0;
rt = zeros (2,1);
while max(abs((P-Pi)./P))>0.000005  % convergence criteria
Pi = P;

for j=1:M
    for i=1:N
        l = (j-1)*N+i;
        him = 1+eps*cos(dt*(i-2)); % h(i-1) film thickness at node i-1
        hi  = 1+eps*cos(dt*(i-1)); % hi film thickness at node i
        hip = 1+eps*cos(dt*i); % h(i+1) film thickness at node i+1


        % coefficients in the FD formulation

        c1 = hi^3/2/dz^2;
        c2 = (3/8*hi^2/dt^2*(hip-him)+1/2*hi^3/dt^2);
        c3 = (-3/8*hi^2/dt^2*(hip-him)+1/2*hi^3/dt^2);
        c4 = cons*hi/2/dt;
        c5 = cons*(hip-him)/2/dt;
        c6 = (hi^3/dt^2)+(hi^3/dz^2);


        % description of pressure on the left boundary nodes
        if i~=1
            Pleft = P(l-1);
        else
            k=j*N;
            Pleft = P(k);
        end

        % description of pressure on the right boundary nodes
        if i~=N
            Pright = P(l+1);
        else
            k=(j-2)*N+i+1;
            Pright = P(k);
        end

        % description of pressure on the bottom boundary nodes
        if l-N>=1
            Pdown = P(l-N);
        else
            Pdown = Pl;
        end

        % description of pressure on the top boundary nodes
        if l+N<=M*N
            Pup = P(l+N);
        else
            Pup = Ph;
        end

        % Gause - Seidel iterative solution – root finding
        rt(1) = -(c5 + sqrt((c5^2)-(4*(-c6)*((c2*Pright-c4)*Pright +
(c3*Pleft+c4)*Pleft + c1*(Pup^2+Pdown^2)))))/2/c6;
```

```
        rt(2) = -(c5 - sqrt((c5^2)-(4*(-c6)*((c2*Pright-c4)*Pright +
(c3*Pleft+c4)*Pleft + c1*(Pup^2+Pdown^2)))))/2/c6;
        % ================================

        % error condition1 - two roots can not be above zero!
        if (rt(1)>=0)&&(rt(2)>=0)
            ups = ups+1
        % refine mesh!
        end

        % error condition2 - two roots can not be below zero!
        if (rt(1)<=0)&&(rt(2)<=0)
            bups = bups+1
        % refine mesh!
        end

        % appropriate solution
        if rt(1)>0
            P(l) = rt(1);
        else
            P(l) = rt(2);
        end
        % you can move with the next iteration
    end
end

% display iteration
if mod(iter,10)==0
        iter;
end

iter=iter+1;
end

% relative error
max(abs((P-Pi)./P))

% pressure matrix on the seal/shaft/bearing boundary
P_mat = zeros (M,N);

% put the obtained pressure values in the matrix (dimesionless)
for ro = 1:M
    for co = 1:N
        P_mat (ro,co) = P((ro-1)*N+co);
    end
end

% periodicity boundary condition
P_mat = [P_mat P_mat(:,1)];

% insert the bottom and top boundary pressure values (dimensionless)
P_mat = [gb; P_mat; gt];

% pressure ratio
p_rat = P_mat./Pl;

% calculation of P*r components - dimension (m)
for ro = 1:M
    for co = 1:N
        P_mat_x (ro,co) = P((ro-1)*N+co)*r*sin(dt*(co-1));
        P_mat_y (ro,co) = P((ro-1)*N+co)*r*cos(dt*(co-1));
```

```
    end
end

% apply periodicity condition
P_mat_x = [P_mat_x P_mat_x(:,1)];
P_mat_y = [P_mat_y P_mat_y(:,1)];

% calculation of P*r components on the top and bottom boundaries (m)
for co = 1:(N+1)
        gb_x (1,co) = Pl*r*sin(dt*(co-1));
        gb_y (1,co) = Pl*r*cos(dt*(co-1));
        gt_x (1,co) = Ph*r*sin(dt*(co-1));
        gt_y (1,co) = Ph*r*cos(dt*(co-1));
end
% Complete P*r matrix - dimension of each component (m)
P_mat_x = [gb_x; P_mat_x; gt_x];
P_mat_y = [gb_y; P_mat_y; gt_y];

% Numerical integraton
% components of total force acting on the boundary, dimension = N
F_x =  dz*r*dt*Pa*trapz(trapz (P_mat_x,2),1);
F_y = -dz*r*dt*Pa*trapz(trapz (P_mat_y,2),1);

% B/D ratio (dimensionless)
B_D = B/2/r;

% Net force acting on the seal/shaft/bearing (N)
F = sqrt(F_x^2+F_y^2);

% Load ratio (dimensionless)
P_rati = F/2/r/B/Pa

% Pressure variation on boundary in dimensional form (N/m^2)
P_mat = P_mat*Pa-Pa;
maximum = max (max(P_mat))
minimum = min (min(P_mat))

% results

figure (1)
surf (0:dt*r:2*pi*r, -B/2:dz*r:B/2, P_mat)
title ('Pf - Absolute Pressure Variation')
xlabel ('Arc Length (2*pi*r) [m]')
ylabel ('Width (B) [m]')

figure (2)
plot (0:dt*r:2*pi*r, P_mat(ceil((size(P_mat,1)/2)),:))
grid on
title ('Pf - Absolute Pressure Variation, x-z cross section view @
y=0')
xlabel ('Arc Length (2*pi*r) [m]')
ylabel ('Pf')

figure (3)
plot (-B/2:dz*r:B/2, P_mat(:,ceil((size(P_mat,2)/2))))
grid on
title ('Pf - Absolute Pressure Variation, y-z cross section view @
x=pi*r')
xlabel ('Width (B) [m]')
ylabel ('Pf')
%%%%%%%%%%%%%%%%%%%%%%%%%%%%      end      %%%%%%%%%%%%%%%%%%%%%%%%%%%%%
```

Appendix B

Numerical Validation with Other Published Work

Figures Validating the Results for B/D=1

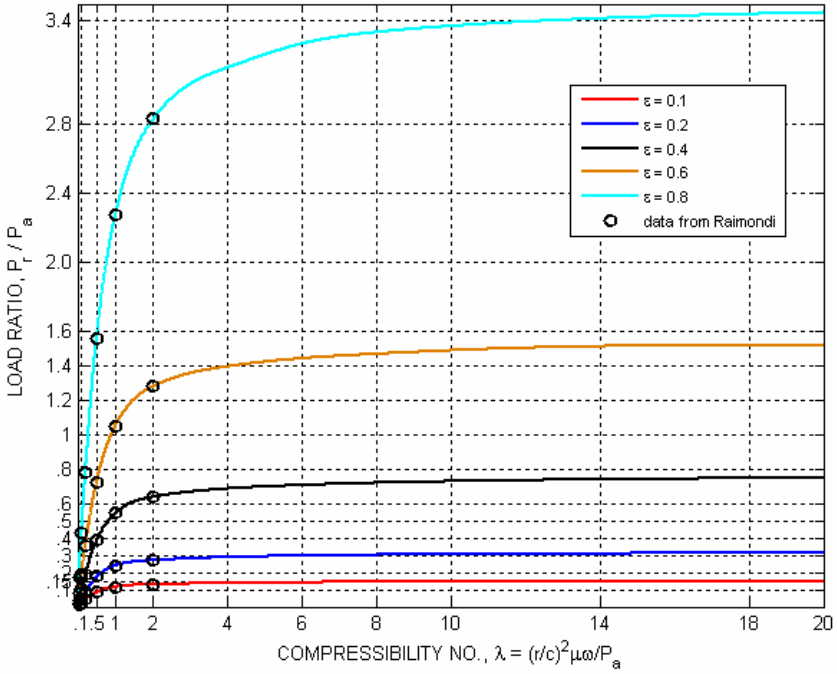

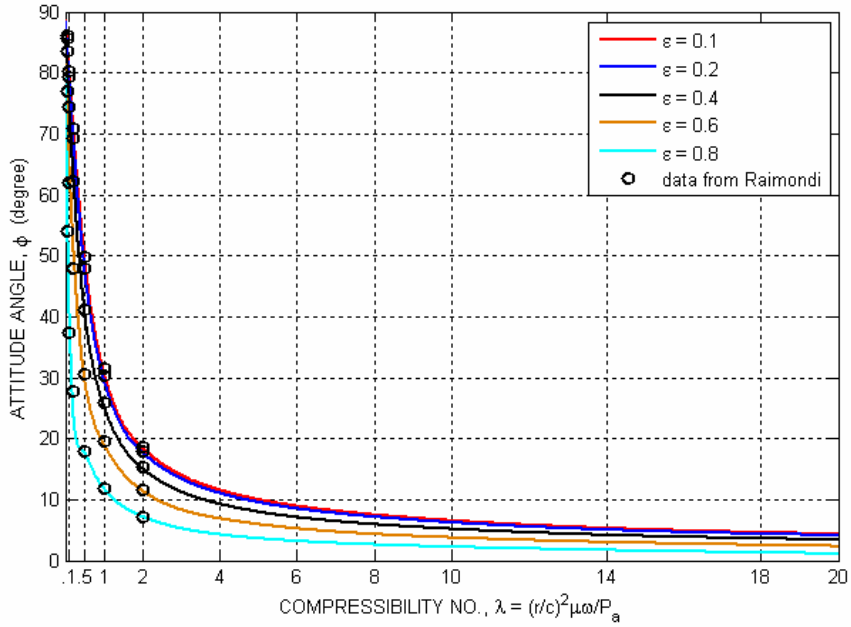

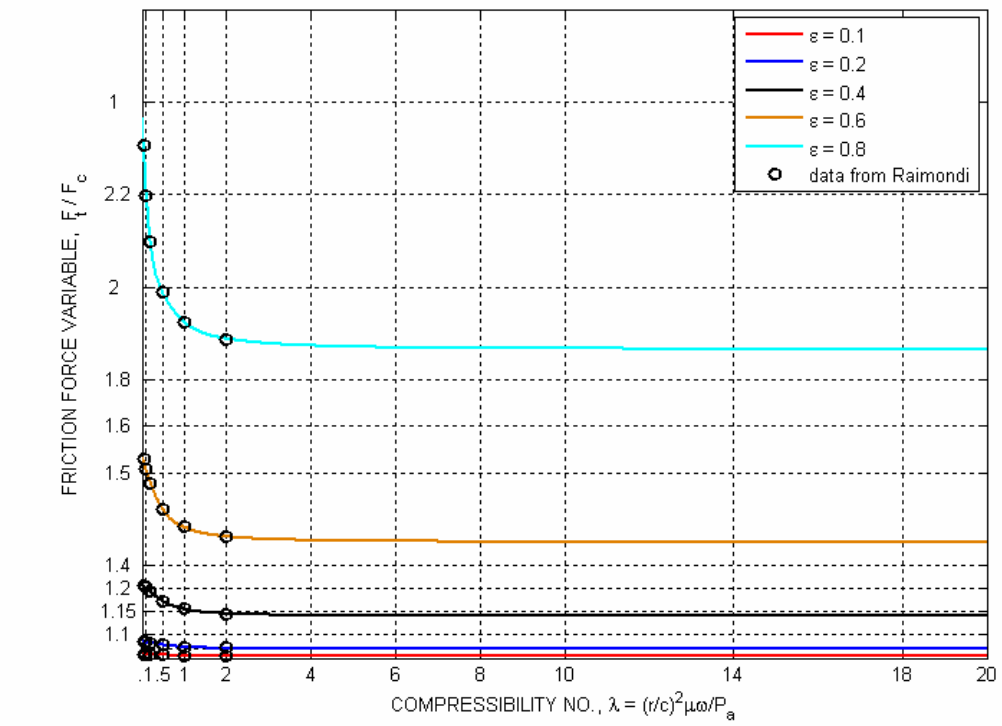
ε = 0.1
ε = 0.2
ε = 0.4
ε = 0.6
ε = 0.8
data from Raimondi
FRICTION FORCE VARIABLE, F_f / F_c
1
2.2
2
1.8
1.6
1.5
1.4
1.2
1.15
1.1
.1.5 1 2 4 6 8 10 14 18 20
COMPRESSIBILITY NO., $\lambda = (r/c)^2 \mu\omega/P_a$

Tables Validating the Results for B/D=1

B/D = 1 - ε = 0.1													
	Compressibility Number, λ												
	0.1	0.2	0.4	0.5	0.6	0.8	1.0	2.0	4.0	6.0	8.0	10	20
P_r / P_a	0,022217	0,042585	0,074122	0,085341	0,09412	0,106368	0,114083	0,12904	0,1374	0,141229	0,143735	0,145322585	0,149414
Φ	80,06697	70,7551	55,41039	49,43543	44,4293	36,73812	31,25906	18,5643	11,55314	8,902787	7,478235	6,515588699	4,320448
S	0,716359	0,747463	0,858884	0,932467	1,01459	1,19701	1,395082	2,46676	4,633335	6,761566	8,858247	10,95183813	21,30389
P_{max} / P_a	1,021612	1,042282	1,075986	1,088172	1,098136	1,111751	1,119653	1,130971	1,126124	1,125718	1,126195	1,126315428	1,126711
P_{min} / P_a	0,97939	0,961528	0,936182	0,927956	0,922011	0,914131	0,909952	0,905605	0,910286	0,910377	0,91006	0,910043672	0,909717
relative err	4,98E-08	4,96E-08	4,99E-08	4,99E-08	4,98E-08	4,99E-08	4,98E-08	4,96E-08	4,95E-08	4,94E-08	4,99E-08	4,99076E-08	5E-08
# of iterations	926	985	1043	1049	1059	1082	1091	1106	1102	1214	3144	3542	42820
m	36	36	36	36	36	36	36	36	36	36	60	60	108
n	40	40	40	40	40	40	40	40	40	40	40	40	72

B/D = 1 - ε = 0.2													
	Compressibility Number, λ												
	0.1	0.2	0.4	0.5	0.6	0.8	1.0	2.0	4.0	6.0	8.0	10	20
P_r / P_a	0,045514	0,086906	0,150861	0,173952	0,192314	0,218522	0,235436	0,2689	0,287158	0,295322	0,300636	0,303989205	0,312588
Φ	79,04003	69,08188	53,50141	47,64565	42,79316	35,37661	30,10097	17,83115	11,04627	8,496646	7,130481	6,206944633	4,108198
S	0,349684	0,36627	0,421991	0,457467	0,496548	0,582658	0,676002	1,18375	2,216971	3,233515	4,235156	5,235545879	10,18305
P_{max} / P_a	1,047157	1,093469	1,17093	1,199692	1,223814	1,257078	1,279266	1,310595	1,301967	1,300798	1,301931	1,302194105	1,302607
P_{min} / P_a	0,957511	0,923561	0,880839	0,868136	0,859117	0,84836	0,842651	0,838987	0,847698	0,847971	0,847398	0,847382069	0,846835
relative err	4,96E-08	4,99E-08	4,98E-08	4,98E-08	4,97E-08	4,98E-08	4,99E-08	4,98E-08	4,94E-08	4,98E-08	4,98E-08	4,97449E-08	5E-08
# of iterations	1013	1044	1090	1096	1092	1123	1140	1159	1141	1200	3152	3422	12766
m	36	36	36	36	36	36	36	36	36	36	60	60	108
n	40	40	40	40	40	40	40	40	40	40	40	40	72

B/D = 1 - ε = 0.4													
	Compressibility Number, λ												
	0.1	0.2	0.4	0.5	0.6	0.8	1.0	2.0	4.0	6.0	8.0	10	20
P_r / P_a	0,100966	0,190565	0,32976	0,382459	0,426158	0,492318	0,537994	0,634679	0,684715	0,705378	0,718626	0,727424142	0,748048
Φ	74,01418	61,67168	45,97027	40,73179	36,53067	30,22501	25,75517	15,18325	9,256676	7,068111	5,908385	5,143979781	3,378734
S	0,157632	0,167035	0,193056	0,208068	0,224079	0,258622	0,295831	0,501529	0,929758	1,353784	1,771768	2,187924953	4,255208
P_{max} / P_a	1,12929	1,25742	1,465666	1,547377	1,614107	1,712037	1,781883	1,898636	1,895581	1,890023	1,892691	1,892804423	1,893904
P_{min} / P_a	0,901626	0,842737	0,789859	0,777683	0,769798	0,762822	0,759834	0,762364	0,778554	0,77988	0,779012	0,778200634	0,777214
relative err	4,96E-08	4,97E-08	4,96E-08	4,99E-08	5E-08	5E-08	4,99E-08	4,97E-08	4,99E-08	4,98E-08	4,99E-08	4,99661E-08	5E-08
# of iterations	1070	1041	1076	1050	1049	1123	1108	1164	1159	1131	2991	6148	36353
m	36	36	36	36	36	36	36	36	36	36	60	90	240
n	40	40	40	40	40	40	40	40	40	40	40	60	140

B/D = 1 - ε = 0.6													
	Compressibility Number, λ												
	0.1	0.2	0.4	0.5	0.6	0.8	1.0	2.0	4.0	6.0	8.0	10	20
P_r / P_a	0,188632	0,35467	0,615567	0,717556	0,804529	0,942206	1,042976	1,275113	1,393783	1,440929	1,4666	1,487158782	1,52983
Φ	61,57443	47,53516	34,19247	30,25081	27,17823	22,63185	19,40173	11,49423	6,867114	5,214997	4,298676	3,732551501	
S	0,084373	0,089748	0,10342	0,110901	0,118694	0,135134	0,152597	0,249633	0,456757	0,662718	0,868157	1,070194689	
P_{max} / P_a	1,333963	1,637945	2,094285	2,269972	2,417293	2,645371	2,806664	3,138599	3,18836	3,170516	3,175102	3,173404421	
P_{min} / P_a	0,820102	0,760912	0,726315	0,721588	0,720473	0,719186	0,721193	0,73478	0,754509	0,758385	0,757592	0,755387303	
relative err	4,97E-08	4,97E-08	5E-08	4,97E-08	5E-08	5E-08	4,96E-08	4,97E-08	4,98E-08	5E-08	4,86E-08	4,99424E-08	
# of iterations	1043	999	1021	1020	1017	1080	1108	1186	1193	2835	3068	8112	35780
m	36	36	36	36	36	36	36	36	36	60	60	108	362
n	40	40	40	40	40	40	40	40	40	40	40	72	400

B/D = 1 - ε = 0.8													
	Compressibility Number, λ												
	0.1	0.2	0.4	0.5	0.6	0.8	1.0	2.0	4.0	6.0	8.0	10	20
P_r / P_a	0,430193	0,790948	1,333132	1,5446	1,727071	2,023519	2,249782	2,822909	3,127282	3,267104	3,33461	3,373541501	
Φ	36,80605	27,4392	19,94883	17,81315	16,14857	13,66268	11,85971	7,192428	4,228056	3,157501	2,578289	2,207232969	
S	0,036996	0,040244	0,047754	0,05152	0,055292	0,062922	0,070742	0,11276	0,20357	0,292286	0,381826	0,471774078	
P_{max} / P_a	2,119045	2,8956	3,990249	4,42445	4,796251	5,39474	5,845202	6,896328	7,183802	7,128744	7,135072	7,148276266	
P_{min} / P_a	0,723368	0,697302	0,692881	0,696046	0,696503	0,704036	0,709433	0,728904	0,750892	0,757887	0,757248	0,756798919	
relative err	5E-08	4,99E-08	4,99E-08	4,99E-08	4,99E-08	4,97E-08	4,97E-08	5E-08	4,99E-08	5E-08	5E-08	0,00000005	
# of iterations	983	958	958	1019	1051	1110	1151	2589	2750	9177	33964	61968	
m	36	36	36	36	36	36	36	60	60	120	250	350	
n	40	40	40	40	40	40	40	40	40	80	140	140	

Analysis results of finite difference approach when B/D=1

B/D = 1 - ε = 0.1													
	Compressibility Number, λ												
	0.1	0.2	0.4	0.5	0.6	0.8	1.0	2.0	4.0	6.0	8.0	10	20
P_r / P_a	0,0223	0,0427	0,0743	0,0856	0,0943	0,1066	0,1143	0,1292	0,1376	0,141	0,143	0,145	0,149
Φ	80,02	70,7	55,34	49,36	44,36	36,67	31,2	18,5	11,57	8,93	7,44	6,47	4,166
F_t / F_c	1,008	1,008	1,007	1,007	1,006	1,006	1,005	1,005	1,005	1,005	1,005	1,005	1,005
S	0,713	0,744	0,855	0,929	1,011	1,194	1,391	2,462	4,623	6,745	8,847	10,937	21,296
time (sec.)	39	29	24	114	29	33	38	18	30	38	85	126	164

B/D = 1 - ε = 0.2													
	Compressibility Number, λ												
	0.1	0.2	0.4	0.5	0.6	0.8	1.0	2.0	4.0	6.0	8.0	10	20
P_r / P_a	0,04569	0,0872	0,151	0,174	0,192	0,219	0,235	0,269	0,287	0,296	0,3	0,304	0,312
Φ	79,01	69,04	53,44	47,59	42,74	35,33	30,06	17,832	11,086	8,556	7,143	6,222	4,09
F_t / F_c	1,035	1,033	1,03	1,028	1,027	1,025	1,024	1,021	1,021	1,02	1,02	1,02	1,02
S	0,348	0,364	0,42	0,456	0,495	0,581	0,674	1,181	2,212	3,226	4,23	5,229	10,178
time (sec.)	48	93	124	118	125	138	125	254	442	534	559	663	803

B/D = 1 - ε = 0.4													
	Compressibility Number, λ												
	0.1	0.2	0.4	0.5	0.6	0.8	1.0	2.0	4.0	6.0	8.0	10	20
P_r / P_a	0,1011	0,1909	0,33	0,383	0,42	0,493	0,539	0,635	0,686	0,707	0,719	0,727	0,748
Φ	74	61,671	45,981	40,744	36,544	30,23	25,77	15,21	9,305	7,128	5,924	5,143	3,345
F_t / F_c	1,153	1,144	1,128	1,122	1,118	1,11	1,106	1,096	1,092	1,092	1,091	1,091	1,091
S	0,157	0,1667	0,192	0,207	0,223	0,258	0,295	0,5005	0,9275	1,35	1,769	2,186	4,255
time (sec.)	54	100	103	123	124	121	125	176	350	395	520	552	711

B/D = 1 - ε = 0.6													
	Compressibility Number, λ												
	0.1	0.2	0.4	0.5	0.6	0.8	1.0	2.0	4.0	6.0	8.0	10	20
P_r / P_a	0,1884	0,3543	0,6157	0,718	0,805	0,944	1,045	1,279	1,399	1,445	1,471	1,488	1,528
Φ	61,64	47,64	34,4	30,36	27,28	22,72	19,48	11,53	6,92	5,237	4,319	3,726	2,382
F_t / F_c	1,408	1,375	1,332	1,319	1,308	1,293	1,283	1,262	1,254	1,252	1,251	1,25	1,25
S	0,0844	0,0898	0,103	0,11	0,118	0,134	0,152	0,248	0,454	0,66	0,865	1,069	2,081
time (sec.)	42	112	113	135	138	124	127	248	329	478	552	607	772

B/D = 1 - ε = 0.8													
	Compressibility Number, λ												
	0.1	0.2	0.4	0.5	0.6	0.8	1.0	2.0	4.0	6.0	8.0	10	20
P_r / P_a	0,4278	0,789	1,338	1,553	1,739	2,042	2,274	2,857	3,168	3,275	3,335	3,373	3,461
Φ	37,044	27,64	20,1	17,95	16,275	13,766	11,94	7,229	4,248	3,156	2,57	2,196	1,365
F_t / F_c	1,994	1,899	1,813	1,788	1,77	1,744	1,726	1,689	1,674	1,67	1,669	1,668	1,667
S	0,0372	0,04	0,0475	0,05122	0,0548	0,0623	0,0699	0,111	0,2	0,291	0,381	0,471	0,919
time (sec.)	65	139	137	131	149	142	140	209	345	462	516	574	726

Analysis results of finite element method when B/D = 1